Global Modeling and Assimilation Office
Annual Report & Research Highlights
2011-2012

NASA Goddard Space Flight Center ★ August 1, 2012

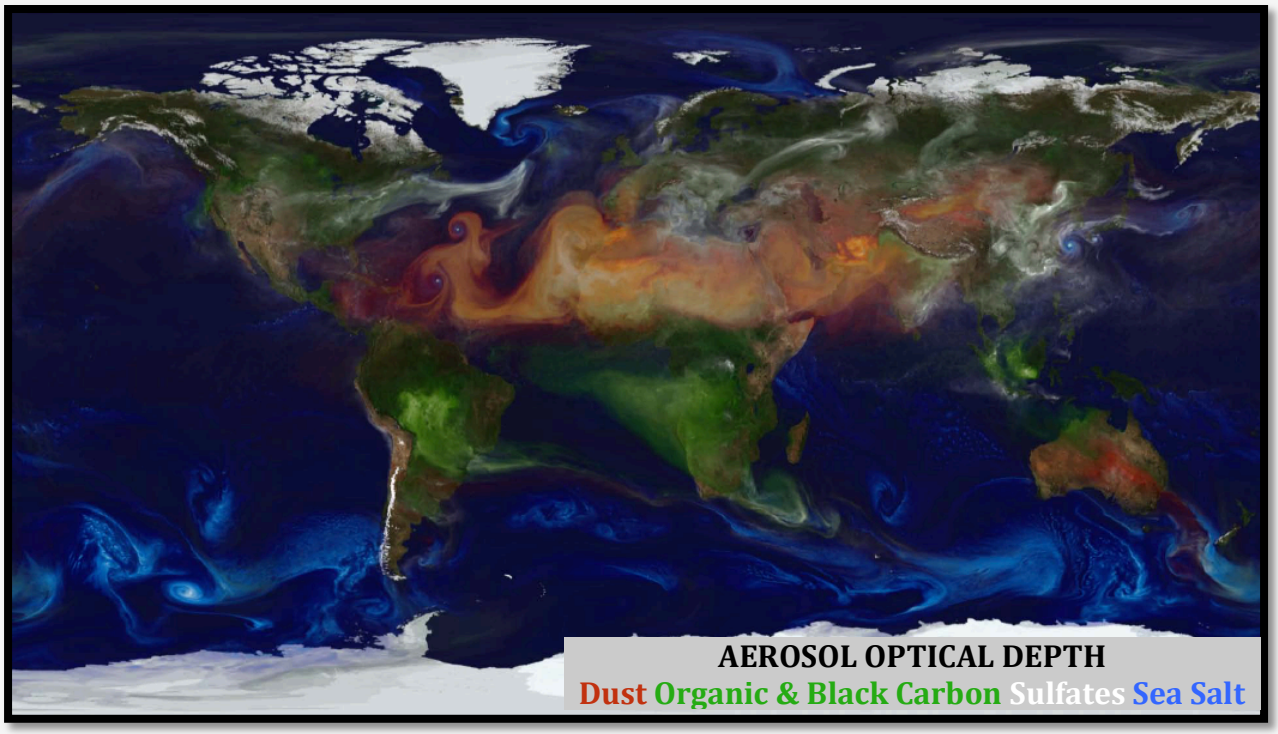

The image on the front cover is a single snapshot from a 2-year simulation conducted by Bill Putman with the GEOS-5 AGCM on the cubed sphere grid at 10-km resolution. The simulation used the Goddard Chemistry Aerosol Radiation and Transport (GOCART) integrated with GEOS-5 and ran on 3750 processors of the Discover supercomputer at the NASA Center for Climate Simulation.

Table of Contents

July 2011 – June 2012 in review

Over the last year, the Global Modeling and Assimilation Office (GMAO) has continued to advance our GEOS-5-based systems, updating products for both weather and climate applications. We contributed hindcasts and forecasts to the National Multi-Model Ensemble (NMME) of seasonal forecasts and the suite of decadal predictions to the Coupled Model Intercomparison Project (CMIP5).

The collaboration with NOAA/NCEP in the development of the Gridpoint Statistical Interpolation (GSI) analysis has continued and helped us to provide high quality products from GEOS-5 for NASA instrument teams and other science groups who use GEOS-5 products. This year, we have made progress on our 4DVar and, through collaboration with both NCEP and NOAA/ESRL, a hybrid ensemble-variational assimilation.

While we have continued to use version 5.2.0 of the GEOS-5 atmospheric data assimilation system (ADAS), at 1/2° × 2/3°× 72L, for MERRA and products for NASA instrument teams, the 1/4° system, with GEOS-5.7.3, became operational in August 2011. With this system, assimilated and forecast aerosol distributions have been provided in near real time alongside our regular meteorological products. We continue to improve the near real-time information from these systems online at http://gmao.gsfc.nasa.gov/forecasts. Observation impacts based on the GEOS-5 atmospheric data assimilation adjoint system are now produced routinely and posted on the GMAO's external web page, allowing near real-time monitoring of short-range forecast impacts of all assimilated observations simultaneously. A recently developed Structured Query Language (SQL) database and accompanying python-based utilities allow fast retrieval and display of GEOS-5 operational impact statistics back to August 2010. This capability has facilitated GMAO's participation in several national and international observing system research projects and assessment activities (THORPEX Intercomparison Project, ConcordIASI, Fifth WMO Observation Impact Workshop, NWS observing system planning exercise).

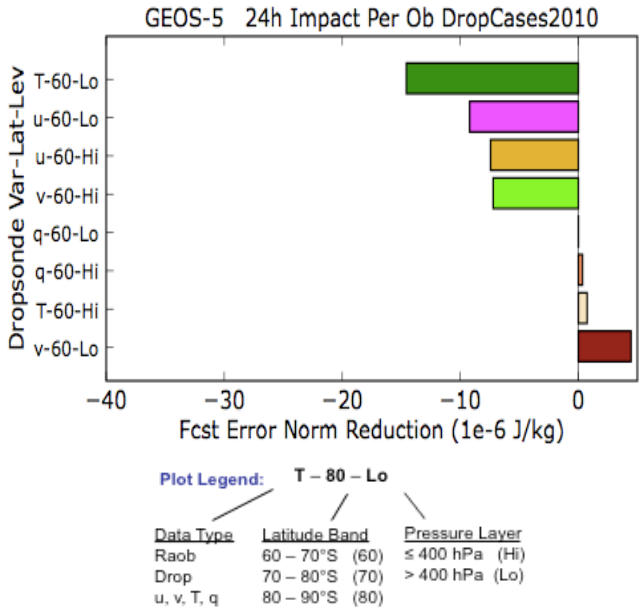

The adjoint of a data assimilation system provides a means of measuring the impact of observations on numerical weather forecasts. During this period, we used the GEOS-5 observation impact tool to examine the impact of dropsondes during the ConcordIASI campaign. The figure here shows the overall impacts of dropsonde observations in terms of their fractional contributions to the reduction of a measure of 24-h forecast error over the region 60-90°S, surface to 50 hPa for the period 20 Sep 2010 – 20 Dec 2010. The measure combines errors in wind, temperature and surface pressure with respect to the verifying analysis, in terms of energy per unit mass (J/kg). The largest impacts are achieved with lower tropospheric temperature observations in the 60-70°S band. Interestingly, in GEOS-5, the meridional wind observations in this region had a detrimental impact on 24-hour forecasts.

In addition to the extensive analysis of the observing system through the GEOS-5 adjoint tools, the web site now includes our radiance monitoring and statistics for assimilated observations. In collaboration with the NASA Center for Climate Simulation (NCCS), GEOS-5 products remain openly available on the NCCS data portal in addition to the regular access for NASA instrument teams through the Goddard Earth Sciences Data and Information Services Center (GES DISC).

The GEOS-5 analyses and forecasts, with aerosols and tagged tracers from regions of biomass burning, supported the DISCOVER-AQ (Deriving Information on Surface Conditions from Column and Vertically Resolved Observations Relevant to Air Quality) field campaign in July 2011. The field campaigns in this four-year project are designed to provide systematic and concurrent observations of column-integrated, surface, and vertically-resolved distributions of aerosols and trace gases relevant to air quality as they evolve throughout the day. Support was also provided to BORTAS (BOReal forest fires on Tropospheric oxidants over the Atlantic using Aircraft and Satellite) in July 2011, HIPPO (HIAPER Pole-to-Pole Observations of Carbon Cycle and Greenhouse Gases Study) from June–August 2011, and HS3 (Hurricane and Severe Storm Sentinel) in August 2011. As a result of our international collaborations on aerosol modeling and assimilation, GEOS-5 dust forecasts are now included in the WMO Dust and Sand Storm Warning Advisory and Assessment System (WMO SDS-WAS), see http://sds-was.aemet.es/forecast-products/dust-forecasts/compared-dust-forecasts.

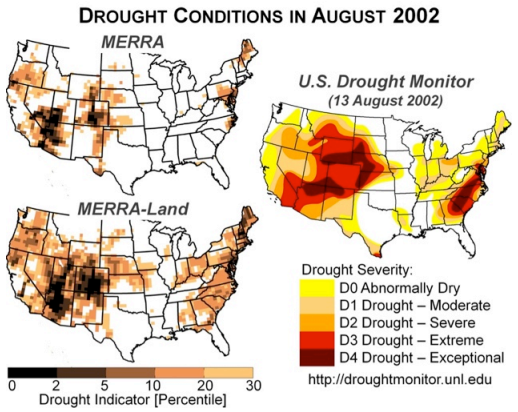

The MERRA-Land collection is a supplement to MERRA, with an improved set of land surface hydrological fields, generated by re-running a revised version of the Catchment land model used the MERRA system but with corrections to the precipitation forcing from the global gauge-based NOAA Climate Prediction Center "Unified" (CPCU) precipitation product.

With few exceptions, the MERRA-Land data appear more accurate than the original MERRA estimates. For example, MERRA-Land data are more consistent than MERRA with the Drought Monitor's estimates of the drought conditions experienced across the western United States and along the East Coast during August 2002. The MERRA and MERRA-Land drought indicators shown in the figure are derived by ranking the normalized, monthly mean root zone soil moisture anomalies for June, July, and August of 1980 through 2011 and converting the rank for August 2002 into percentile units.

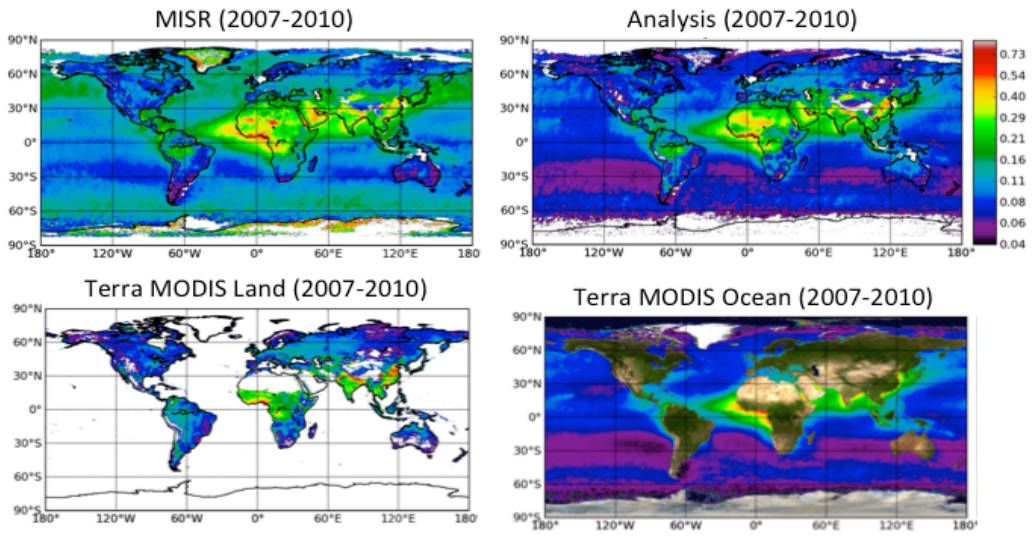

MERR*Aero* provides time series of gridded aerosol products that are consistent with MODIS and in-situ AOD measurements. Like MERRA-Land, observed precipitation is used during replay. In addition to assimilation of MISR and MODIS observations, the analysis is driven by QFED daily biomass burning estimates derived from MODIS fire radiative power. Stringent cloud screening during assimilation explains some of the differences between the analysis and the MODIS observations over the ocean.

Production of the GMAO's Modern-Era Retrospective Analysis for Research and Applications (MERRA) has continued, with products released only a few weeks behind real time. As of the end of June 2012, users had downloaded almost 1.2 PB of data from the GES DISC. The special collection of MERRA papers in the Journal of Climate (http://journals.ametsoc.org/page/MERRA) has continued to grow. We have examined regional climate information from MERRA as a contribution to the most recent National Climate Assessment. Monthly mean data have also been published through the Earth System Grid node in the NCCS to facilitate the availability of MERRA data for model evaluations anticipated for the Fifth Assessment Report (AR5) of the IPCC. The MERRA-Land reanalysis has corrected some of the deficiencies in the land surface products from MERRA itself and is now available from the GES DISC as one of the MERRA collections. Other MERRA-forced component reanalyses have been conducted or are underway. One example is the MERR*Aero* product currently in progress, based on the GEOS-5 model coupled to GOCART and forced by MERRA fields in the GEOS-5 replay configuration.

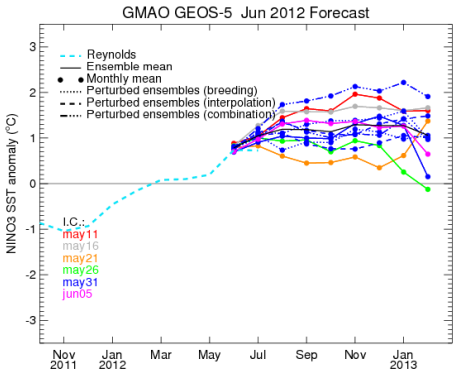

GMAO's seasonal forecasts are now conducted with GEOS-5, initialized from the GEOS-5 AOGCM constrained by MERRA and by the GEOS ocean and sea-ice assimilation system. Each month the 30-year hindcast suite as well as the ensemble of forecasts initialized every 5 days, with a 7-member ensemble near the beginning to the month, are contributed to the U.S. National Multi-Model Ensemble. Here we show the Niño-3 forecasts initialized for the June 2012 forecasts and the historical anomaly correlation skill for the first two seasons of the forecasts.

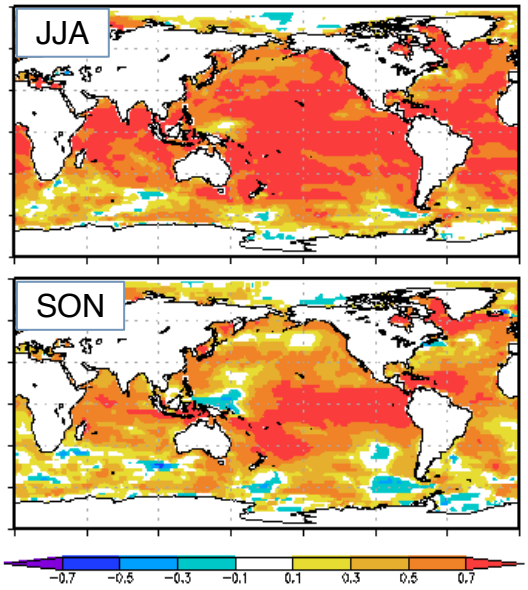

Another is the ocean reanalysis conducted using MERRA (and a coarser resolution scout version of MERRA) to force the GEOS ocean and sea-ice data assimilation system from 1960 to 2011. These states were used to initialize seasonal predictions with a 30-year suite of hindcasts to calibrate the forecasts. These are now being contributed each month to the National Multi-Model Ensemble (NMME). Three-member ensemble decadal predictions have also been conducted, initialized in December of each year from 1960 to 2005. These have been published through the Earth System Grid node in the NCCS as a contribution to the Coupled Model Intercomparison Project Phase 5 (CMIP5). A revised tuning of the system with improved error covariances is now underway and is being contributed to the international intercomparison being conducted under the auspices of CLIVAR and GODAE OceanView.

Since January, the new GMAO seasonal forecast system, using GEOS-5, has been predicting a transition from cold to warm conditions in the eastern Pacific in about June 2012. Observed SST in the Niño-3 region (150°–90°W, 5°S–5°N) was close to zero from March to May and increased to about 0.5°C in June. The GEOS-5 forecast system improves upon the

SST forecasts from the previous system, CGCMv1, especially in the equatorial Atlantic.

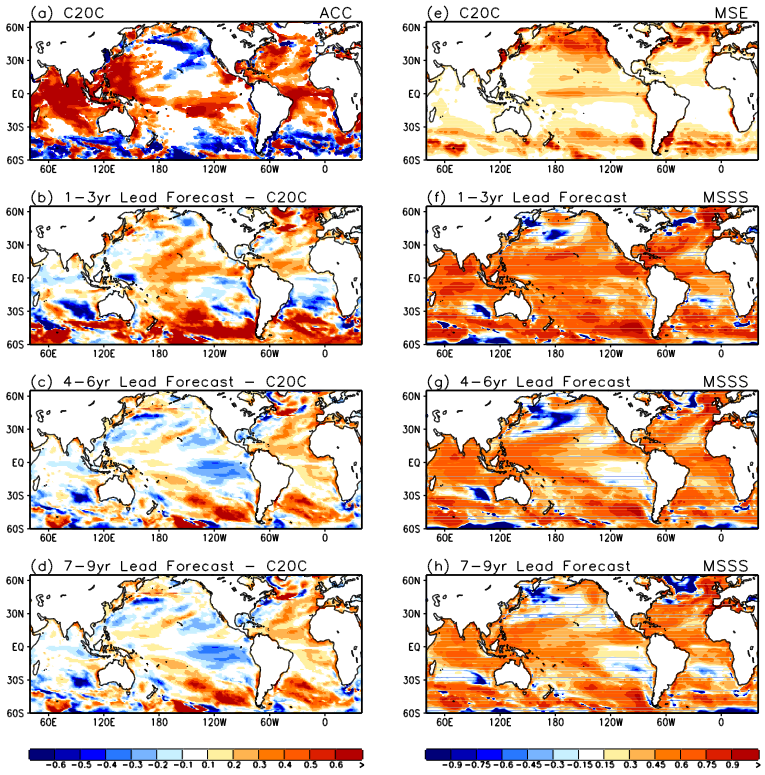

Decadal predictions for CMIP5 have been conducted with the GEOS-5 AOGCM, initialized every December from 1960 to 2010 from the ocean and sea-ice reanalysis and MERRA (or the MERRA scout prior to 1979). Three ensemble members were generated using a two-sided breeding centered on the reanalyses. The prediction skill of these initialized ensembles improves upon that from uninitialized ensembles (3 ensemble members of a free-running coupled integration, C20C) in many parts of the globe, as seen in the figure to the left. The top left panel shows the anomaly correlation of the 3-year moving averaged SST from the C20C simulation with the GMAO ocean reanalysis. The panels below show the difference of the C20C correlation from that of the initialized predictions at increasing lead times. The upper right hand panel shows the Mean Square Error (MSE) of the C20C simulation. The panels below show the Mean Squared Skill Score (MSSS) at increasing lead times.

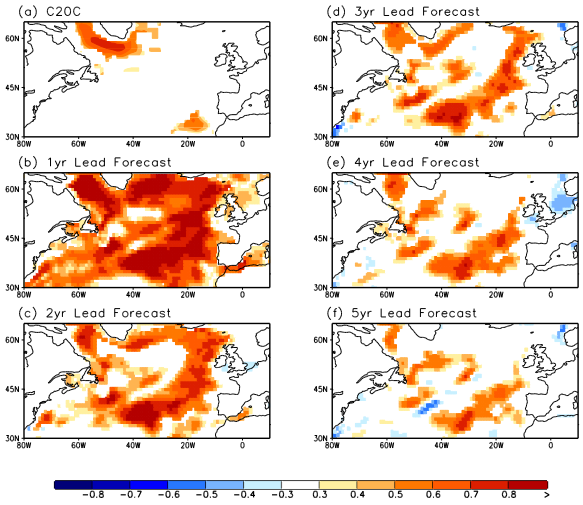

The correlation skill of the de-trended annual mean HC500 anomaly in the C20C simulation, and increasing leads up to a 5-year lead forecast.

It is apparent in the correlation, and even more so in the MSSS, that there is some degradation of skill in the initialized forecasts in the subpolar North Atlantic. This is clearer in the in the anomaly correlation of the heat content in the upper 500 m of the ocean when the trend related to global warming is removed. The degradation with forecast lead can be related to biases in the transports in the subpolar region. Thus, model biases need to be reduced to improve the predictability of climate variations in this region.

Substantial progress has also been made in the GEOS land data assimilation system, with the assimilation of passive microwave, AMSR-E, and active microwave, ASCAT, soil moisture, as well as snow. GMAO continues to lead the development and implementation of the Level 4 Surface and Root Zone Soil Moisture product for the NASA Soil Moisture Active Passive (SMAP) Mission.

Significant modeling developments have been in very high-resolution (cloud-permitting) global simulation capability, the update of the cloud microphysics in GEOS-5 to a two-moment scheme, which explicitly calculates the mass and number of cloud ice and liquid, rain and snow, and in an aerosol-cloud microphysics component that facilitates computation of aerosol indirect effects. The new cloud microphysics implementation has significantly improved the prediction of microphysical variables like ice and liquid water content and cloud particle size, and of large scale variables like cloud fraction and cloud radiative forcing. We have also completed the integration of a vegetation module adapted from the NCAR Community Land Model (CLM4). The photosynthesis, conductance, and carbon treatments from CLM4 have been integrated the GMAO's Catchment land surface model (LSM) to produce a merged LSM that simulates the fluxes and states of water, energy, and carbon together while maintaining the the unique water and energy balance framework of the Catchment LSM. One unique feature of our merged model, for example, is the ability to simulate different degrees of phenological development in different sub-regions of a given land element, capturing, for example, the greater lushness of vegetation in riparian zones. Relative to the original Catchment LSM, and aside from the addition of the carbon and phenology treatments, the new system features separate prognostic variables in the canopy and ground surface and a broader catalogue of vegetation types for a more accurate characterization of the land boundary.

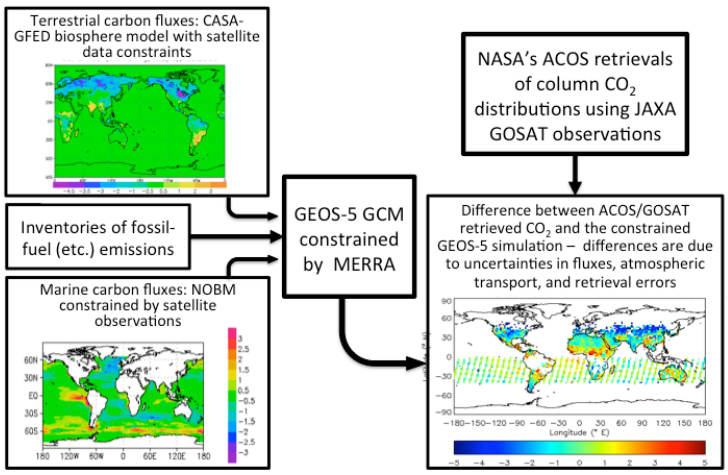

GMAO is contributing to NASA's Carbon Monitoring System (CMS) by using GEOS-5 analyses in the "Flux Pilot Project." Atmospheric constraints from GEOS-5 are used alongside satellite observations to compute CO_2 fluxes from the land and the ocean. CO_2 fluxes from the ocean to the atmosphere are computed using the NASA Ocean Biogeochemistry Model (NOBM), forced by wind speeds from MERRA and constrained by ocean color observations. Similarly, MERRA meteorology is used to constrain surface processes in a terrestrial biosphere model (CASA-GFED) that computes CO_2 fluxes using additional constraints from satellite data (the Normalized Difference Vegetation Index, NDVI, from MODIS) and from space-based estimates of biomass burning. These fluxes are combined with inventory information about fossil-fuel CO_2 emissions in computations of atmospheric transport with MERRA. The atmospheric CO_2 concentrations can then be evaluated against in-situ (surface-, tower-, or aircraft-based) measurements and against satellite retrievals, such as the partial column information from GOSAT/ACOS. The framework also allows for other surface flux estimates to be used in GEOS-5, enabling it to be used as an evaluation tool for CMS. This capability allows NASA to play a unique role in carbon monitoring, using GEOS-5 as the central tool in a model constrained analysis, providing a focal point for the broad scientific expertise needed to address this issue. The CMS project also helps GMAO contribute to preparations for NASA's future carbon missions, such as the Orbiting Carbon Observatory Version 2 (OCO-2) and the Active Sensing of CO_2 over Nights, Days and Seasons (ASCENDS).

Following are more detailed presentations of some of the research highlights from this period.

Preliminary Studies with a 3DVAR-Hybrid Ensemble for GEOS Atmospheric Data Assimilation

Amal El Akkraoui and Ricardo Todling (GMAO)
Jeffrey Whitaker (ESRL), David Parrish (NCEP), and Daryl Kliest (NCEP)

The reliance of many data assimilation procedures on a static, time-independent, error covariance that is supposed to represent background (short-range forecast) errors has long been recognized to be a weakness in practical (operational) global numerical weather prediction (NWP) systems. Many approaches have been proposed to allow some flow-dependent representation of background errors. Most are unfeasible for practical use and a few only allow for partial flow-dependence, such as for the error variances, leaving the error correlations still unchanged. From the mid-to-late 1990s, ensemble-based data assimilation procedures were introduced as possible candidates to replace variational data assimilation for NWP purposes (Houtemaker and Mitchell, 1998). However, pure-ensemble data assimilation is a considerable departure from the more familiar variational approach most operational NWP centers employ. A more conservative approach has been proposed (Hamill and Snyder, 2000; Lorenc, 2003) allowing ensemble data assimilation to be combined with the variational approach, bringing flow-dependence to operational procedures without need for a complete revamp of existing code. These so-called hybrid systems can be built as extensions to either three-dimensional (3D) or four-dimensional (4D) variational systems.

GMAO has collaborated with NCEP in the development of the Grid-point Statistical Interpolation (GSI) system. Originally 3DVAR-capable only, this collaboration has enabled GSI with a 4D-capability. Concurrently, the collaboration between ESRL and NCEP has introduced an ensemble-hybrid capability to GSI. GMAO is currently investigating a traditional 4DVAR and the 3DVAR-hybrid as possible intermediate steps toward fully 4D-hybrid data assimilation for GEOS. Here we summarize results from the implementation of a hybrid-3DVAR component for the GEOS atmospheric data assimilation system (ADAS). Together with the GEOS atmospheric general circulation model (AGCM) and GSI, the ensemble Kalman filter of Whitaker et al. (2008) is used to provide analysis updates for GEOS AGCM ensemble forecasts that serve as background to the 3D-hybrid strategy.

In this preliminary study, results from a 10-member ensemble hybrid system are compared with a control experiment running traditional 3DVAR. The resolution of the central ADAS for both the control and the hybrid experiments is 0.5°. When the hybrid option is exercised, the ensemble of short-range forecasts runs at 1° resolution.

Figure 1 shows observation-minus-background residuals for radiosondes over the month of December 2011 for both the control (red) and hybrid (blue) experiments. Observation fits to temperature (top row) and zonal wind (bottom row) are shown for the globe (left column) and for the tropics (right column). Globally, both biases (dash curves) and standard deviations (solid curves) show the hybrid to bring neutral impact to the results. Over the tropics, however, the hybrid shows reduced biases for the zonal wind. A comparison of the zonally-averaged, monthly-mean zonal wind with the corresponding ECMWF wind appears in Fig. 2 and suggests that, indeed the wind biases with respect to ECMWF are slightly reduced in the hybrid system (right) from what is seen for the control experiment with traditional 3DVAR (left). The benefit of using a hybrid-3DVAR strategy for the GEOS ADAS is still only marginal (forecast skills are neutral for all variables and slightly improved for the winds; not shown). This preliminary study is only a proof of concept for GEOS and the machinery involved in the ensemble implementation. Experimentation with an increased number of ensemble members and some adjusted parameters pertinent to the ensemble filter is presently being conducted.

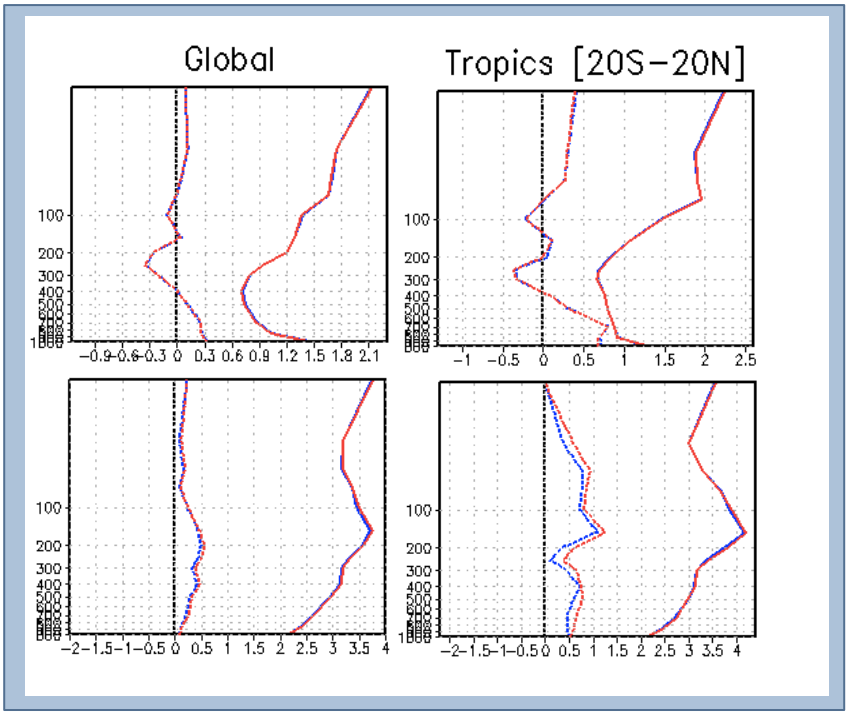

Figure 1: December 2011 observation-minus-background radiosonde residual biases (dashed) and standard deviations (solid) for two GEOS ADAS configurations: the usual 3DVAR (red); and a 3DVAR-hybrid (blue). Top panels show fits to temperature; bottom panels show fits to the zonal component of wind.

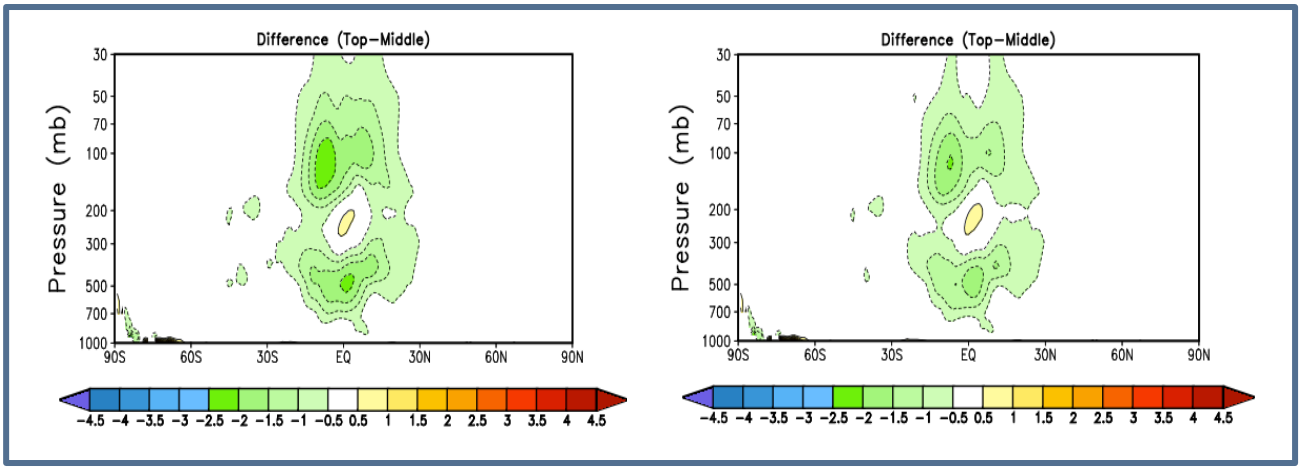

Figure 2: Difference of the zonally-averaged monthly mean zonal wind component of the GEOS ADAS from that of ECMWF for December 2011; left panel is for the control 3DVAR; the right panel is for the Hybrid-3DVAR.

References:

Hamill, T.M., and C. Snyder, 2001:A hybrid ensemble Kalman filter-3D variational analysis system. *Mon. Wea. Rev.*, **128**, 2905-2919.

Houtekamer, P.L., and H.L. Mitchell, 1998: Data assimilation using an ensemble Kalman filter technique. *Mon. Wea. Rev.*, **126**, 796-811.

Lorenc, A.C., 2003: The potential of the ensemble Kalman filter for NWP - A comparison with 4DVAR. *Quart. J. Roy. Meteorol. Soc.*, **129**, 3183-3203.

Whitaker, J.S., T.M. Hamill, X. Wei, Y. Song, and Z. Toth, 2008: Ensemble data assimilation with the NCEP Global Forecast System. *Mon. Wea. Rev.,* **136**, 463-482.

The GEOS 4DVAR: Preliminary Tests with the Cubed-Sphere Tangent Linear and Adjoint Models

Jing Guo, Jong G. Kim, Max Suarez, Atanas Trayanov, Ron M. Errico, and Ricardo Todling

The GMAO has updating its prototype four-dimensional variational (4DVAR) system to a version that can be exercised at operational resolutions. Besides a general circulation model (GCM) and an analysis system, traditional 4DVAR requires availability of tangent linear (TL) and adjoint (AD) models of the corresponding GCM. The GMAO prototype 4DVAR uses the finite-volume-based GEOS Atmospheric GCM (AGCM) and the Grid-point Statistical Interpolation (GSI) system, and TL and AD models derived from an early version of the finite-volume numerics that is computationally outdated. Specifically, the existing TL and AD models use a simple (1-dimensional) latitudinal MPI domain decomposition, which has consequent low scalability and prevents the prototype 4DVAR from being used in realistic applications.

Since GMAO is upgrading its operational GEOS AGCM to use a cubed-sphere grid, we have re-derived the TL and AD models for this grid and taken advantage of its two-dimensional MPI decomposition and scalability properties. With the aid of the *Transformation of Algorithms in FORTRAN (TAF)* automatic adjoint generation tool and some hand-coding, a version of the cubed-sphere-based TL and AD models, with a simplified vertical diffusion scheme, is now available and is thus under intense testing in the 4DVAR framework. Here we present preliminary results of performance testing and static analysis, comparing 3DVAR and 4DVAR. What follows refers to a simple 1° configuration of the data assimilation system.

Experiments to assess computational performance were conducted with various configurations of the TL and AD models, the GSI minimization, and computing resources. The objective of these experiments is to get a basic sense of scalability of the 4DVAR minimization component and quality of the analyses. Initial results appear in Figure 1 in terms of *wall-clock-time*. Panel *(a)* gives the profiling of the GSI-4DVAR components with respect to different numbers of MPI processes. The individual bars show the time spent in the three main components of the minimization: the TL model (blue), the AD model (green), and the remainder of the minimization (yellow). This last part is representative of what typically happens in 3DVAR, where the costs for the TL and AD models are not involved. Within the uncertainty of *wall-clock-time*, it is clear that the TL and AD models dominate the timing for 4DVAR, which is considerably higher than for 3DVAR. However, the scalability of the TL and AD models appears to be much better than that of the rest of the minimization. In particular, scalability of the AD model appears to be even better than that of the TL model. Panel *(b)* of Figure 1 is a scalability chart for the GSI-4DVAR minimization shown as $\log_{10}$(*wall-clock-time*) vs. $\log_{10}$(*NCPUS*). This basically confirms that at this resolution GSI-4DVAR scales relatively well with 216 processes. Furthermore, this evaluation suggests that code scalability can benefit from a hybrid MPI-OpenMP strategy (see the figure caption).

A summary of the quality of the 4DVAR analysis as compared to 3DVAR appears in Figure 2. Results are for a single 6-hour analysis segment and display the normalized fit of the observations to the initial background (blue), to the 4DVAR analysis (solution), and to a 3DVAR analysis calculated from the same background as 4DVAR. Both 3D and 4DVAR use the same conjugate minimization procedure with an orthogonalization of the residuals applied for improved convergence (e.g., El Akkraoui et al., 2012), and 200 iterations; only a single inner loop minimization is evaluated for consistency. Results suggest the 4DVAR fits to be rather comparable to those of 3DVAR. This comparison holds when evaluation is done over 30 days of cycling.

Continuation of the work includes performance tests for other GEOS DAS resolutions of interest, closer examination of the simplified physical parameterizations in the TL and AD models, and investigation of configurations connecting 4DVAR with the ensemble hybrid development.

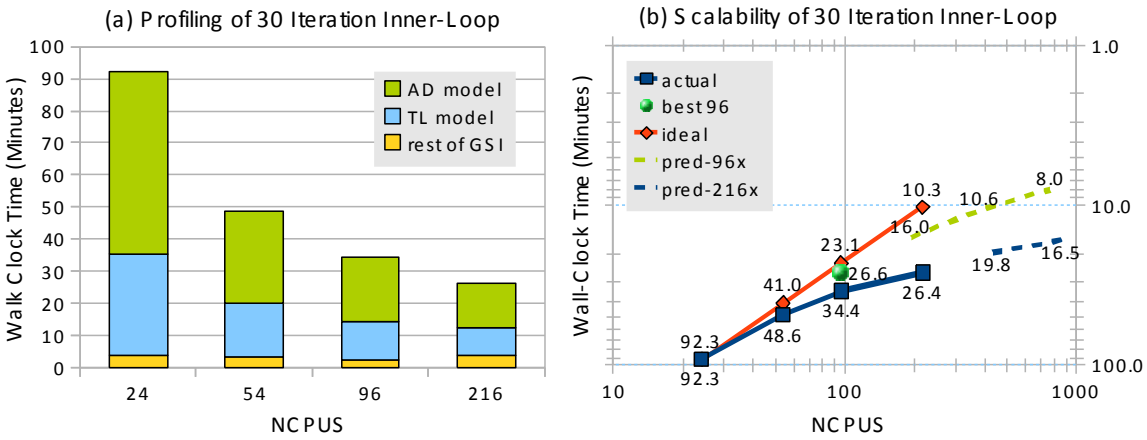

Figure 1: Computational performance of a set of 30-iteration-inner-loop runs with 4DVAR: (a) profiling in wall-clock time (minutes), and (b) scalability in -log$_{10}$(wall-clock time). In (a), TL-model is the time spent on the tangent linear model, and AD-model is the time spent on the adjoint model of the cubed-sphere GEOS AGCM; the remaining is time spent in the GSI initialization and minimization. In (b), actual refers to actual timing; best-96 is a run with 96 MPI processes with simplified computations; ideal is an idealized prediction assuming 100% parallelizable beyond 24 MPI processes; pred-96x is an optimistic extrapolation assuming 80% shared-memory parallelization beyond 96 MPI processes; pred-216x is a less optimistic extrapolation assuming 50% shared-memory parallelization beyond 216 MPI processes. NCPUS=6mn^2, where n is MPI process count, and m is shared memory process count per MPI node. In both (a) and (b), m=1 and n=2, 3, 4, 6 for most cases, except m=2, 4, 8 and n=96 for pred-96x, m=2, 4 and n=216 for pred-216x.

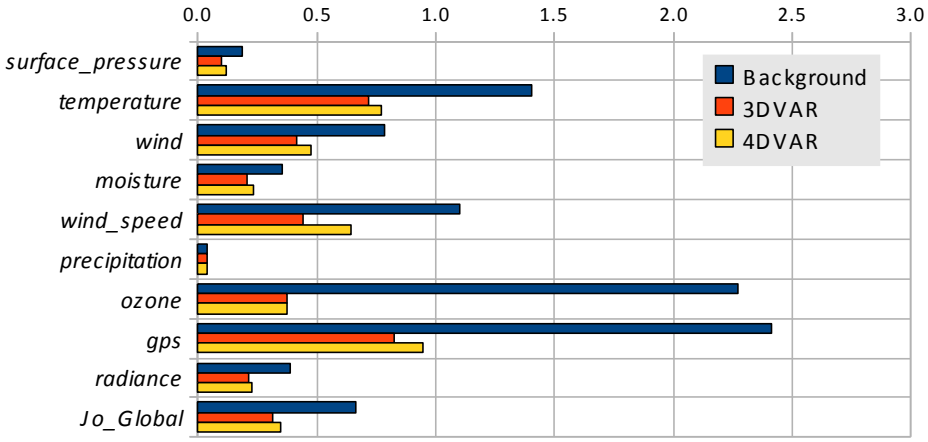

Figure 2: A sample set of normalized observation fits broken down into separate observation types and totals (global). The blue bars are for the observation fits to the background, which for this test is the same in both 3D and 4DVAR. The red bars refer to the observation fits to the 3DVAR analysis (solution), and the yellow bars refer to the observations fits to the 4DVAR analysis.

References:

El Akkraoui, A., Y. Trémolet, and R. Todling, 2012: Preconditioning of variational data assimilation and the use of a Bi-Conjugate Gradient method. *Quart. J. Roy. Meteorol. Soc*. (in press).

Tangent Linear and Adjoint Models of the Cubed-Sphere GEOS GCM

Jong Kim, Max Suarez, Atanas Trayanov, Ron Errico, Jing Guo, and Ricardo Todling

As discussed in the previous report, the planned upgrade of the GEOS AGCM hydrodynamics core has led us to re-derive the TL and AD models for this two-dimensional MPI domain-decomposed cubed-sphere dynamical core. The initial derivation employs the *Transformation of Algorithms in FORTRAN (TAF)* automatic adjoint generation tool. The connections to the Earth System Modeling Framework and to GFDL's Flexible Modeling System have been hand-treated to maintain parallel scalability and MPI communications consistent with the GCM's hydrodynamics code. The interplay between re-computation and check-pointing, largely affecting memory usage, is being addressed in different ways by, for example, investigating various options for the piece-wise parabolic method used for the dynamics and implementing simplifications to the internal time-split option. To render perturbations physically realistic, the TL and AD models also include a simplified vertical diffusion scheme. Initial tests with a 1° configuration suggest that about 70-80% parallel scalability is achieved when using 216 processors.

We have started testing the new AD model as a replacement for the observation impact calculations. An illustration of observation impacts on the 24-hour 00-UTC forecasts for 11 days in November 2011 is shown in Figure 1. Impacts for various components of the observing system are displayed for both the Northern (left panel) and Southern (right panel) Hemispheres. Observation impacts obtained with the new cubed-sphere model and its adjoint (yellow bars) are compared with those obtained with the finite-volume (lat-lon) models used in the current operational GEOS DAS (cyan bars). The forecasts from GMAO operations are conducted at 1/4° whereas those for the cubed-sphere experiment here are at 1°. This is reflected in the former forecasts being more accurate than the latter, which then show larger overall observation impacts. With this in mind, the relative impacts among different observing systems are rather similar between the two experiments: radiosondes, AMSU-A and aircraft observations are the dominant observing systems in the Northern Hemisphere in both cases; and AMSU-A is by far the dominant observing system in the Southern Hemisphere in both experiments. Close examination shows the impact of wind observations to be more significantly distinct in the two systems. Nonetheless, results are very encouraging. Future work includes scalability studies at various resolutions and implementation of a cube-to-cube transformation procedure to allow running forecasts at a resolution higher.

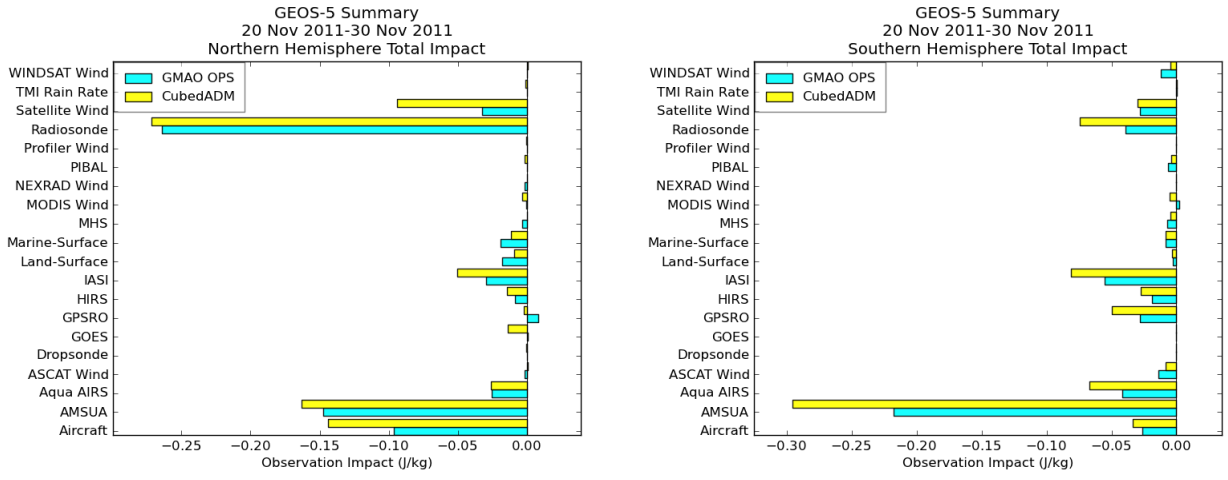

Figure 1: Observation impacts on the 24-hour 00-UTC forecasts for 11 days in November 2011. Results from GMAO operational forecasts (cyan bars) are compared with those obtained with a cubed-sphere version of the DAS running at a resolution of 1°. Observation impacts are separated into Northern (left) and Southern (right) Hemispheres.

The Assimilation of Cloud-affected Infrared Radiances in the GSI

Will McCarty

With the advent of modern hyperspectral sounders like the Atmospheric Infrared Sounder (AIRS), the Infrared Atmospheric Sounding Interferometer (IASI), and the Cross-track Infrared Sounder (CrIS), more than half of the of the global observing system is made of satellite radiances in the thermal infrared. While these observations are large in quantity, infrared measurements that are sensitive to clouds are screened out via quality control. These methods discard ~85% of infrared channels within the window region. It is desirable to incorporate these observations into the assimilation system, but there are difficulties including: the nonlinear nature of clouds on the observations, the difficulty of detecting multilayer clouds within a single field-of-view, spectral variations in cloud emissivity, and the separation of atmospheric and cloud signatures. This ongoing effort is currently focused on the incorporation of a graybody assumption into the observation operator and allowing the cloud top pressure (CTP) to vary in the minimization as part of the control vector.

Current infrared radiances are assimilated by assuming that the atmosphere is clear when comparing the actual observation and its corresponding calculated "guess" observation, derived from the background state. In this study, the guess observation is expanded to allow for a simplified cloud characterization by including a graybody assumption. This defines the cloud by its height (in this case CTP) and cloud fraction. By this expansion, and the corresponding modification of the observation Jacobians from clear-sky to all-sky, it is possible to include infrared observations that are affected by clouds rather than discarding them. As this work is still under development, the initial focus has been on very cloudy observations, determined as those having a retrieved cloud fraction of 0.90 or greater.

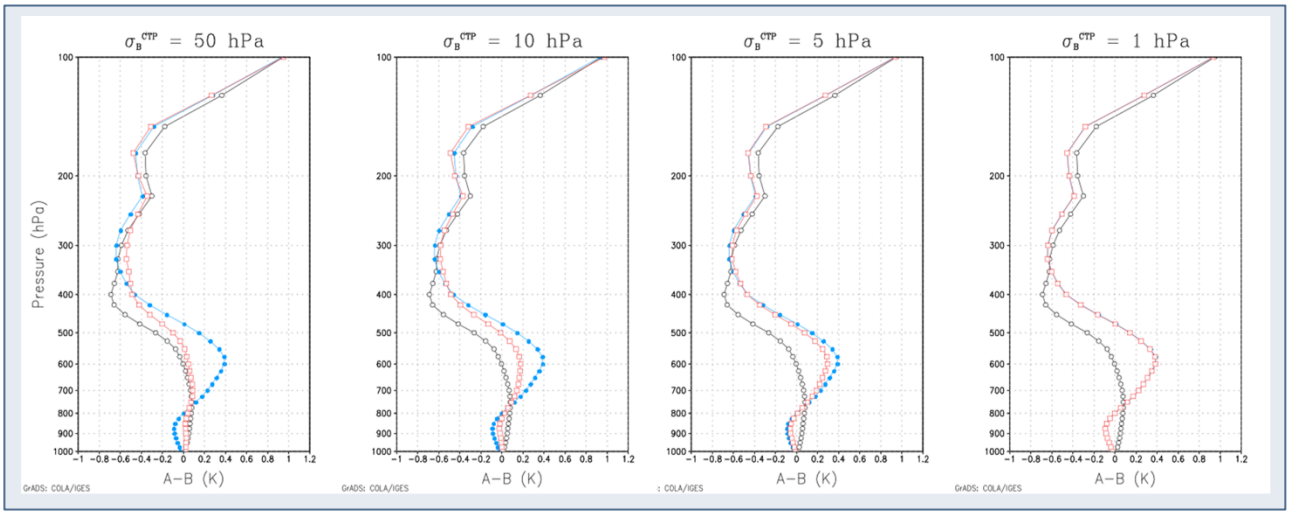

Figure 1: Analysis increments for a single footprint test, assimilating only clear-sky measurements (after QC, black), cloudy measurements with a fixed cloud height (blue), and cloudy measurements with variational cloud height (red), with values of σ_B^{CTP} of 50 hPa, 10 hPa, 5 hPa, and 1 hPa (left to right). The initial CTP for this example was 624 hPa. The estimated cloud fraction was 0.968 and was held constant.

To compensate for a potentially erroneous CTP retrieval, the value is appended to the control vector and allowed to vary in the minimization. Cloud fraction is currently considered as a constant. An example of the analysis increments of temperature for this methodology for a single cloudy footprint is shown in Figure 1 for four different CTP background error variances. In this example, the initial CTP was 624 hPa and the cloud fraction was held constant at 0.968. The example shows a clear-sky only methodology in black. Since channels sensitive to the clouds are discarded, only channels that are considered "clear", in that they are only sensitive to the atmosphere above the clouds, are assimilated. The analysis is therefore

only changed well above the clouds. An example of the analysis increments for a static CTP is included in blue. This includes the graybody characterization of the clouds, but the cloud height is held constant through the minimization. It can be seen that the analysis is changed at the cloud level (624 hPa) and that the background covariances spread the information vertically below the cloud. Once well above the cloud, the analysis increments are similar in both the clear-only and static cloud examples. When allowing the CTP to vary in the minimization, the result varies between the static CTP and clear-only example as a function of background error variance as shown in each panel in red. When CTP is allowed to vary largely with a background error of 50 hPa, the result approaches the clear-only case. The analysis increments are closer to the static CTP case as the CTP background error variance is decreased.

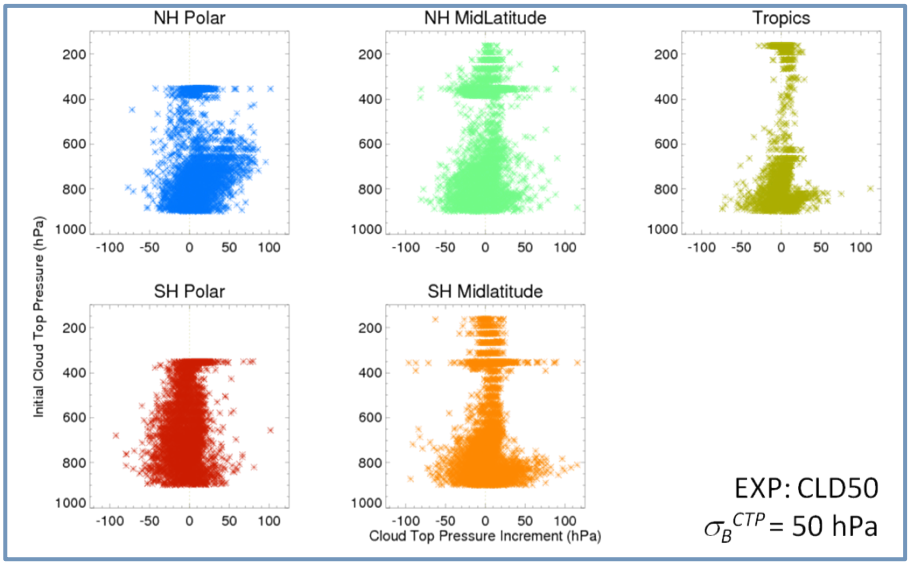

Figure 2: Cloud top pressure vs CTP increment for latitudinal bands for σ_B^{CTP} = 50 hPa for one month of analyses (3 April – 3 May 2011) at 0000 UTC and 0600 UTC. Only measurements with a minimum retrieved cloud fraction of 0.90 are used.

When considering the increments of CTP versus height and location shown in Figure 2, it can be seen that, when left unconstrained, cloud height will change in the minimization differently as a function of both height and location. This illustrates that a simple, constant background error is insufficient. Furthermore, there is evidence that large error variance values have negative effects on the convergence of the minimization. Work is underway to circumvent this issue. One option under consideration is to include a more advanced error model related to the distributions shown in Figure 2. Another is to consider projecting the cloud height into a different vertical coordinate (i.e. log-p or geopotential height).

Though not shown, the initial analysis results show that there is additional information in regions where changes are expected (i.e. regions of persistent, opaque cloudiness). Ongoing work is expanding this development to IASI and CrIS will be trivial and to ascertain its applicability to HIRS. For HIRS though, there is concern that, with the fewer channels, the retrieval of CTP may be less accurate. Expanding to footprints of cloud fraction less than 0.9 will also be a significant way to increase the data count, as the 0.9 threshold is still conservative. The expansion of the control vector to include an observation-centered parameter, in this case CTP, was developed in a flexible manner that will allow for further parameters to be included in the minimization, including skin temperature, simplified surface emissivity, etc. These are being considered for future efforts.

The Impact of Satellite Atmospheric Motion Vectors in the GEOS-5 Global Atmospheric Data Assimilation System

Ronald Gelaro, Dagmar Merkova, and Will McCarty (GMAO)
Patricia Pauley (NRL) and Nancy Baker (NRL)

Atmospheric motion vectors (AMVs), commonly referred to as "satellite winds", are derived by tracing the movement of individual cloud or water vapor patterns in successive images from geostationary and polar-orbiting satellites. Because of their broad spatial coverage and near-continuous availability, AMVs have become an important source of three-dimensional wind information for assimilation into weather prediction models and climate analyses, especially over oceanic regions where *in-situ* wind observations (e.g. from balloons or commercial aircraft) may be sparse. While assimilation of these data improves the accuracy of numerical weather forecasts in general, the degree of improvement can vary significantly depending on the number and treatment of the AMVs selected for assimilation, and the mix of other observation types present in the assimilation system.

This study investigates the impact of AMVs on short-range weather forecasts produced by the GEOS-5 atmospheric data assimilation system. A cycling data assimilation experiment, including forecasts and adjoint-based observation impact calculations, was conducted for a two-month period during the 2010-2011 Northern Hemisphere winter season. Results from a control experiment that included all AMVs and other data types assimilated operationally in GEOS-5 were compared with those from an experiment in which the GEOS-5 AMVs (only) were replaced by ones produced by the Naval Research Laboratory (NRL) for the Navy's operational forecast system. The primary objective of these experiments is to determine whether aspects of the NRL data selection and quality control procedure, especially the use of carefully averaged "super-ob" wind vectors and large volume of AMVs, explain the typically larger beneficial impact of these data in the Navy system as compared with most other forecast systems. Also of interest is whether the impact of the AMVs is modulated by other data types assimilated in GEOS-5, especially the much larger number of satellite radiances.

Figure 1 compares the relative impacts of selected observing systems assimilated in GEOS-5 for the control experiment and the experiment using the NRL AMVs (NRLAMV) in terms of their fractional contributions to the reduction of a global measure of 24-h forecast error. The measure combines errors in wind, temperature and surface pressure with respect to the verifying GEOS-5 analysis. In both experiments, radiosondes (balloon observations) and AMSU-A satellite radiances have the largest beneficial impact, with each providing 20-25% of the total error reduction due to the assimilation of all observations. Satellite winds rank fifth and provide roughly 8% of the total error reduction in the control experiment, but rank third with nearly double the fractional contribution to the total error reduction in the NRLAMV experiment.

Also of interest are the compensating responses of other data types in GEOS-5 to the assimilation of the NRL satellite winds. It can be seen in Figure 1 that while the fractional contribution from satellite winds is nearly doubled in the NRLAMV experiment, the contributions from other leading observing systems such as aircraft, radiosondes, AMSU-A and IASI satellite radiances are reduced by 10-15%.

There are roughly twice as many satellite winds in the NRL observation set as in the control set. Other diagnostics not shown here indicate that that the greater volume (versus super-obing) of the NRL AMVs is primarily responsible for their larger impact, although there is evidence that superobing is also beneficial. For example, map views of the results show that the impact obtained from assimilation of the NRL AMVs is more uniformly beneficial, perhaps due to the averaging of individual observations in creating the super-obs.

The mix of observations plays an important role in modulating the impact of any one data type. For example, while the NRL AMVs have a much larger impact in GEOS-5 than do the control AMVs, their impact is still smaller than in the Navy forecast system (not shown). This is likely due to the larger

number of satellite radiances assimilated in GEOS-5. Identifying and understanding these dependencies and redundancies is not only important for assessing the benefit of existing observing systems, but also for identifying needs for future observations. Additional experiments might therefore include assimilating the NRL AMVs in GEOS-5 while reducing the number of satellite radiance observations.

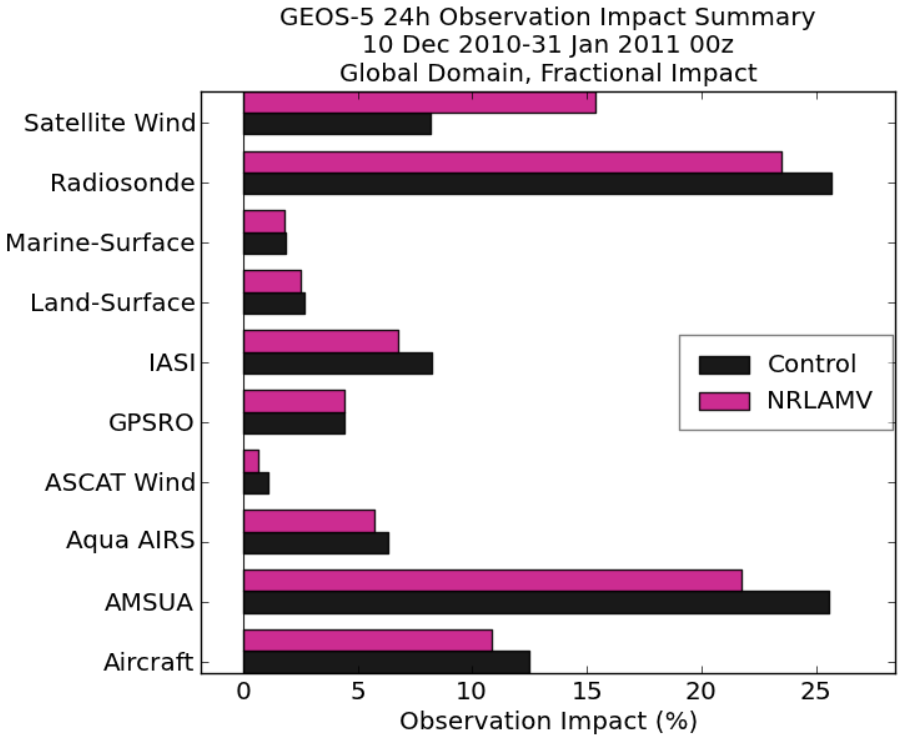

Figure 1: Average impacts of various observing systems on the GEOS-5 24-h forecasts from 00Z during the period 10 December 2010 – 31 January 2011 for the control and NRLAMV experiments. Results are expressed in terms of the fraction of the total error reduction due to assimilation of all observations based on a global error measure. The observation impacts are computed using the adjoint of the GEOS-5 atmospheric data assimilation system.

Complementary Measures of Observation Impact

Ricardo Todling

For over a year now one of the byproducts of GMAO's operational data assimilation system has been a diagnostic of the impact of the observations on the 24-hour forecasts. Similar diagnostics have been produced by a few other operational data assimilation centers (see Gelaro et al. (2010) for specifics). In principle, a nice feature of this diagnostic is that it provides an evaluation of the entire observing system under an equal measure. So far, the common measure has been based on total energy. More recently, Todling (2012) has highlighted some of the subjectivity related to such measures. This work compares various choices of measures (norms) and, in particular, suggests that assessment of the actual performance of the observing system is more directly linked to observation-minus-background and observation-minus-analysis residuals. These residuals are a direct byproduct of any data assimilation system and can be used as a complement to measures based on the 24-hour forecasts.

The left panel of Figure 1 displays a typical summary of the fractional observation impact on the 24-hour forecasts from the GEOS data assimilation system (DAS) obtained with the traditional adjoint-based procedure using a total energy measure. The panel is for the 00 UTC forecasts of December 2011 and shows, for example, that AMSU-A, radiosondes and aircraft observations are the most influential in reducing errors in the 24-hour forecasts when error is measured in units of total energy. The panel on the right shows the fractional impact of the observations on the 00 UTC analyses measured directly in observation space and weighted according to how the analysis system in GEOS DAS normally weighs the observations. In this case, the ranking of the observing system changes and the three dominant observing systems become aircraft, radiosondes and GPS Radio Occultation. This measure is more directly related to how the various observing systems participate in the actual data assimilation cycle. Whereas both assessments of observation impact are useful, the comparison highlights some of the uncertainty associated with various measures.

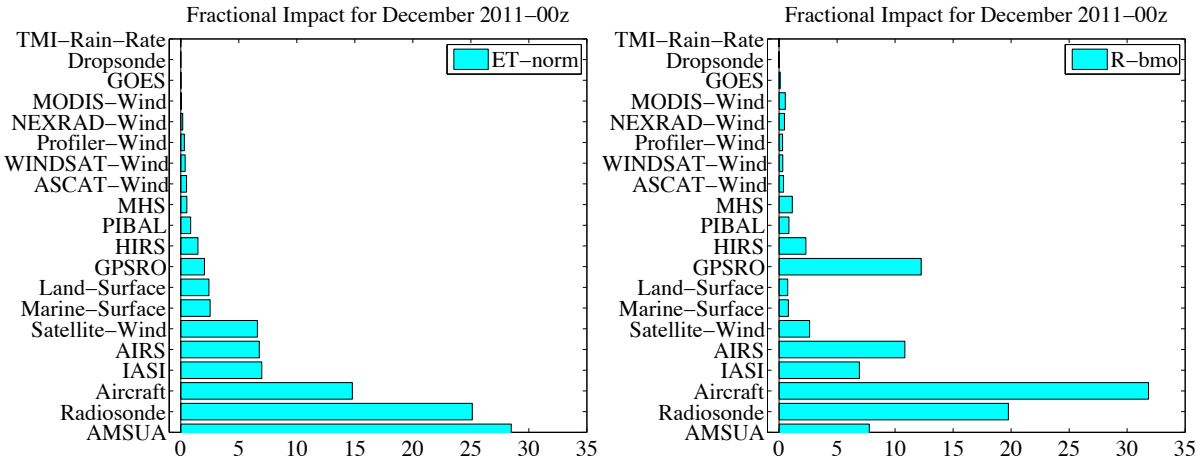

Figure 1: State-space, total energy-norm, observation impact on the 24-hour forecast (left panel), and observation-space, observation error variance-norm, observation impact on the 0-hour forecast (i.e., analysis, right panel); impacts are for all 00 UTC forecasts (analyses) of December 2011.

Further illustration is given in Figure 2, which shows the percentage of observations contributing positively to the 24-hour forecasts (left) and to the analyses (right). These are calculated by simply counting the number of observation whose impacts are negative (these being beneficial) for each instrument of interest, then dividing each result by the corresponding total number of observations for that

instrument type, and multiplying the result by 100. The panel on the right is analogous to the result shown in Gelaro et al. (2010; Figure 5 there), though for a different time period and observing system selection here. Gelaro et al. (2010) remind us that scalar theoretical analysis in idealized settings (Ehrendorfer, 2007; M. Fisher, 2006, personal communication) indicate that roughly 60%-65% of the observations should contribute positively to the assimilation when the accuracy of both backgrounds and observations are comparable. Results such as the one in the left panel of Figure 2, suggesting that only 50% of the observations lead to positive impact on the 24-hour forecast has led Gelaro et al. (2010) to the conclusion that operational systems cannot be expected to perform at theoretical levels. Results displayed in panel (b), when the impact on the analyses is evaluated, indicate otherwise: operational systems do corroborate the scalar theoretical analysis. The bulk of the observing system contributes at exactly the expected theoretical range, that is, 60%-65% of the assimilated observations contribute positively to the background. Todling (2012) provides further corroboration that, from a global measure perspective, current operational data assimilation systems run near optimality. This is not to say that further improvements are not needed, nor possible. Results obtained using alternative verifications indicate there is still plenty of room for improvement.

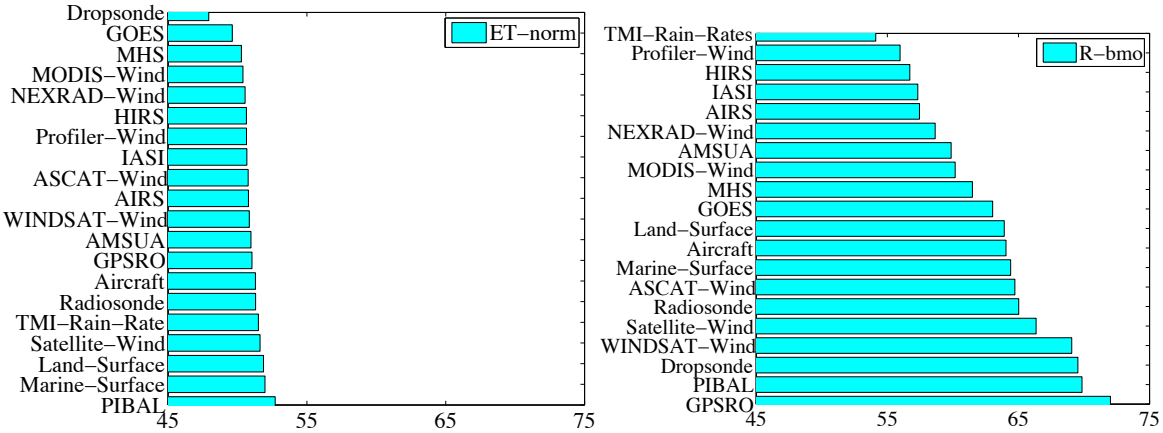

Figure 2: As in Figure 1, but showing percentage of observations contributing positively to the 24- and 0-hour forecasts (analyses), left and right panels, respectively.

In general, an assessment of the performance of the observing system involves a variety of diagnostics. This work highlights that a variety should be applied in practice.

References:

Ehrendorfer, M., 2007: A review of issues in ensemble-based Kalman filtering. *Meteorologische Zeitschrift*, **16**, 795–818.

Gelaro, R., R.H. Langland, S. Pellerin, and R. Todling, 2010: The THORPEX observation impact inter-comparison experiment. *Mon. Wea. Rev.*, **138**, 4009-4025.

Todling, R., 2012: Insights on observation impact measures. *Mon. Wea. Rev.* (submitted).

Sea Surface Temperature Analysis in the GSI

Santha Akella and Ricardo Todling

The main goal of this project is to produce an analysis for the sea surface temperature (SST) in the GEOS coupled atmosphere-ocean system. Such a product will provide improved estimates of surface fluxes in order to better predict short timescale weather features such as tropical cyclones and also yield balanced-initial conditions for climate predictions.

We improved skin SST modeling in the surface modules of the GEOS AGCM, focusing on the interface of atmosphere and ocean. Very close to the interface, a very thin cool skin layer, typically a few microns to millimeters in thickness, almost always exists. This cool skin is about 0.1-0.5 K cooler than the underlying water, and is mostly due to molecular diffusion, net longwave, latent and sensible heat fluxes. During daytime or light wind conditions, the cool skin layer is dominated by diurnal warming (~2-4 K). We included both cool skin effects (based on Fairall et al., 1996) and diurnal warming, following Zeng and Beljaars (2005). In Figure1 we plot the mean diurnal warming (at 12Z) for a period from August 2-10, 2011. Top-left and right panels show a comparison of the free running AGCM without and with the diurnal model, respectively. In the bottom panel we compare the water temperature at 1 m depth from our model runs with hourly TAO buoy data for the same period. For the first two days the model captures diurnal variability reasonably well, but because the model was run freely, the forecast diverged from observed data later in the simulation.

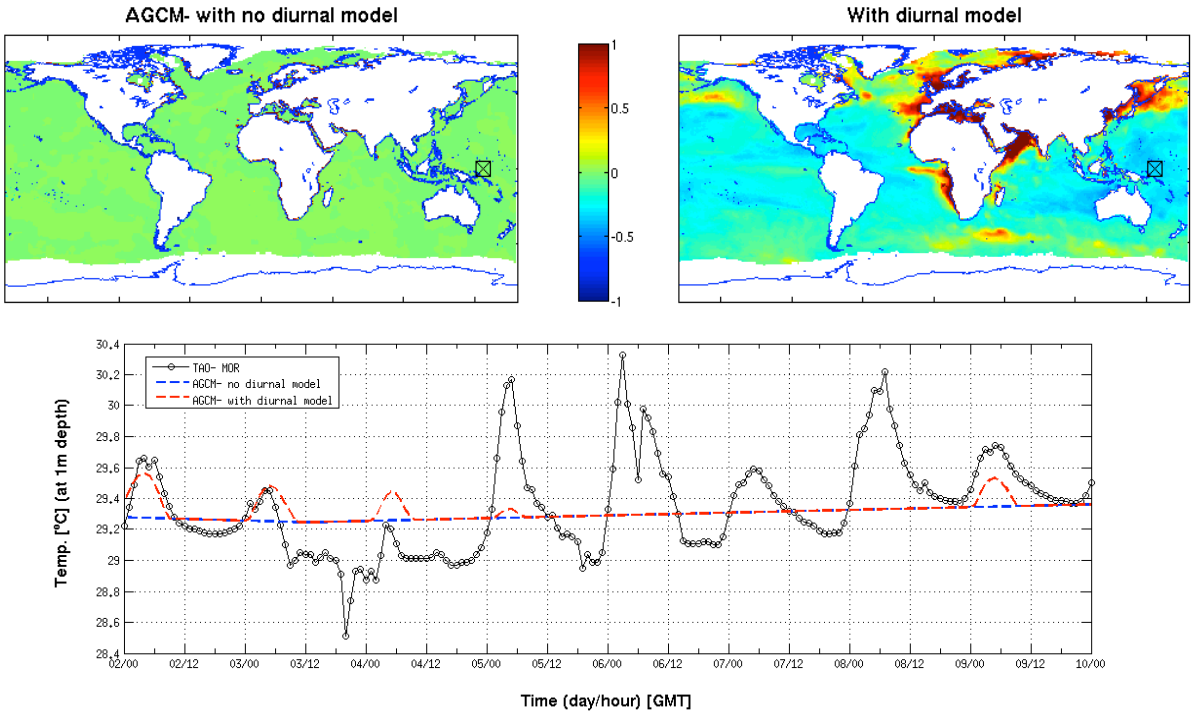

Figure 1: Top Panel: Mean difference between skin temperature and Reynolds SST for 2-10 August 2011 at 12Z. The left (right) panel shows the result without (with) a diurnal warm layer model. The TAO buoy location at 0N, 156E, used for the time series in the bottom panel, is marked by ⊠. Bottom Panel: Comparison of model predicted temperature at 1m depth with hourly TAO data. The blue (red) dashed curve is for the model without (with) the diurnal warm layer model.

We are also working on including the diurnal variability of SST in the GEOS atmospheric analysis system in collaboration with NCEP. Infrared sensors, such as AIRS, AVHRR, HIRS-3/4 are capable of measuring temperature within the cool skin layer. In addition, surface floating buoys and microwave sensors, for e.g., AMSR-E, AMSU-A, AMSU-B, can measure diurnal warming within the top two meters of the ocean. Within the analysis, the interface to the CRTM has been modified so that an analysis can be generated for brightness and in situ surface temperature measured by different observing systems. In Figure 2 we plot the analysis increment for skin temperature over the open ocean.

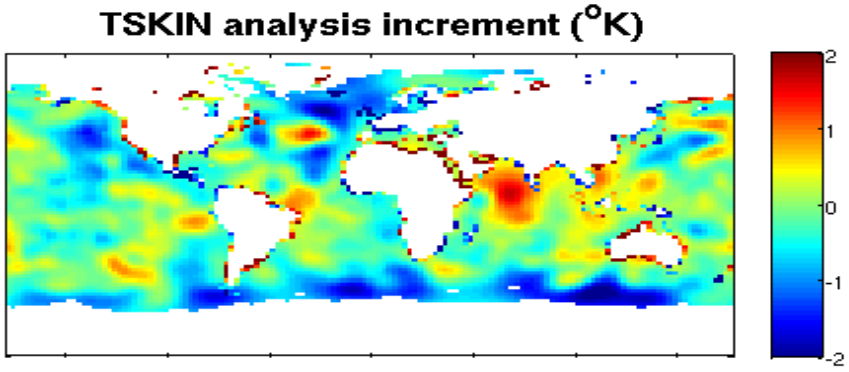

Figure 2: Difference between analysis (ANA) and background (BKG) skin temperature from a single GSI analysis for August 2, 2011 at 0Z.

We are now integrating the analysis output with the model. Following this step, we will tune and refine the analysis quality control, improve diurnal warming effects in the model and set up test cases.

Reference:

Fairall, C.W., E.F. Bradley, J.S. Godfrey, G.A. Wick, J.B. Edson, and G.S. Young, 1996: Cool-skin and warm-layer effects on sea surface temperature. *J. Geophys. Res*., **101**, 1295- 1308.

Zeng, X., and A. Beljaars, 2005: A prognostic scheme of sea surface skin temperature for modeling and data assimilation. *Geophys. Res. Lett*., **32**, L14605, doi:10.1029/2005GL023030.

Assimilation of MODIS Cloud Data into GEOS-5 by Monte Carlo Bayesian Inference

Peter Norris and Arlindo da Silva

The current horizontal resolution of global NWP simulations is still not sufficient to resolve individual clouds, which typically have scales of 1 km or less. This is the basis for our development of an advanced statistical cloud parameterization for GEOS-5. The parameterization characterizes the statistical properties of cloud within a model grid-column using distributions of sub-gridscale total moisture in each model layer and a copula function to correlate these distributions in the vertical (Norris et al., 2008). As in Norris and da Silva (2007), we are developing methods to extract statistical information from high-resolution satellite data to constrain the layer moisture distributions and the copula cloud overlap model. The MODIS instruments on Terra and Aqua provide a wealth of high-resolution cloud retrievals (cloud optical thickness in 1 km pixels and cloud top pressure in 5 km pixels) that suit this purpose very well. This parameter constraint or estimation is a form of cloud data assimilation, having the ability to correct biases both in the moisture state variables and in the empirical constants of the cloud parameterization.

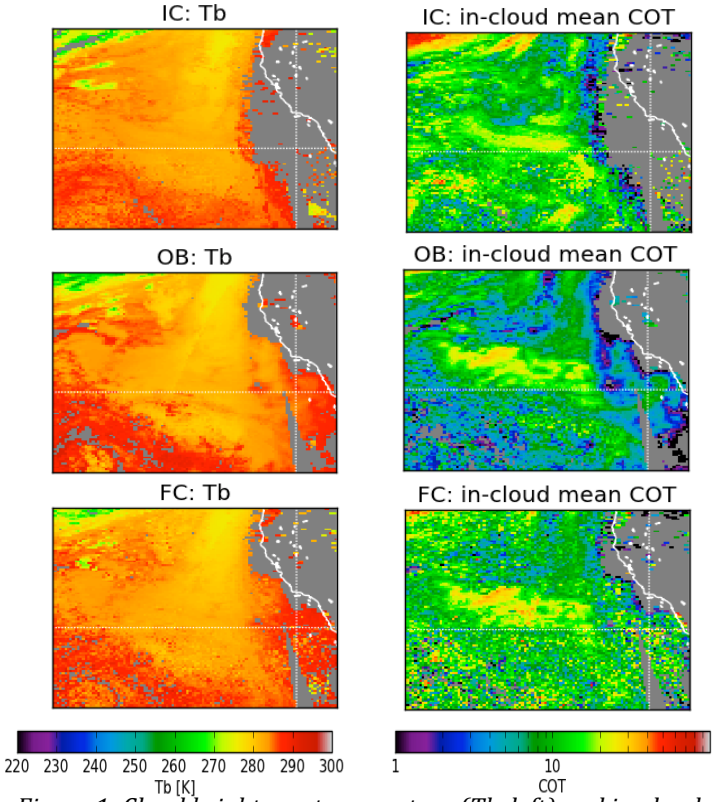

Figure 1: Cloud brightness temperature (Tb, left) and in-cloud cloud optical thickness (COT, right) for a marine stratocumulus field off Southern California. The background (top panels) show no stratocumulus near the coast, as compared to the MODIS observations (mid panels). This is rectified by the MODIS cloud assimilation (bottom panels), although the COT is too high.

Existing cloud assimilation schemes are typically based on tangent linear models, which is problematic for clear grid-column backgrounds because no infinitesimal temperature or moisture perturbations can produce cloud observations. To address these sorts of issues we use Markov Chain Monte Carlo methods to allow finite (but reasonable) departures from the background state into regions of control parameter space with higher posteriori probability, such as into regions that simulate cloud in the presence of cloudy observations. Figure 1 shows an example where the scheme is able to restore marine stratocumulus to the Californian coastline when it is absent in the background. We have also been able to show very significant reductions in global and regional bias and RMS error of cloud optical thickness, cloud brightness temperature and cloud top pressure using the new Monte Carlo cloud assimilation method.

References:

Norris, P.M., L. Oreopoulos, A.Y. Hou, W.-K. Tao, X. Zeng, 2008: *Q. J. Roy. Meteorol. Soc*., **134**, 1843-1864.

Norris, P.M. and A.M. da Silva, 2007: *J. Atmos. Sci*., **64**, 3880-3895.

Norris, P. M. and A. M. da Silva, 2012: Monte Carlo Bayesian inference on a statistical model of sub-grid column moisture variability using high-resolution cloud observations. Part I: Method. *Q. J. Roy. Meteorol. Soc*. (submitted).

Assimilation of Radiance Data from the Microwave Limb Sounder in GEOS-5

Kris Wargan and Steven Pawson (GMAO)
Nathaniel Livesey, William Read, Paul Wagner and Haley Nguyen (JPL)

While the satellite data assimilation community has moved toward direct assimilation of radiances, retrieved data still tends to be used in trace gas assimilation. The motivation behind assimilating radiances is twofold. First, retrieved data are affected by *a priori* information (e.g., climatological or earlier analyses) which then 'contaminates' the assimilation analyses. Second, retrieval algorithms introduce additional errors which can be highly correlated in the vertical. Such correlations are difficult to represent in assimilation systems and are often ignored for simplicity. Another incentive for the use of radiances is their availability in near real time.

We have added a capability to assimilate radiances from the Microwave Limb Sounder (MLS) onboard EOS Aura into the GEOS-5 Atmospheric Data Assimilation System (GEOS-ADAS). Here, we present the current status and early results. At present our system assimilates MLS band 7 (near 240 GHz) which consists of 25 channels sensitive to ozone at 125 tangent altitudes. The observation operator employs the MLS Callable Forward Model (CFM) developed at JPL and integrated within the GEOS-ADAS. A full implementation will require simultaneous fitting of ozone mixing ratio, tangent pressure grid, and an extinction field which will account for effects of absorption not explicitly represented in the CFM. As a first step we use prescribed tangent pressure obtained from prior retrievals and we set the extinction field to zero. We plan to include an online retrieval of extinction in the next version of the algorithm. This implementation can be extended to include other bands for assimilation of temperature and water vapor.

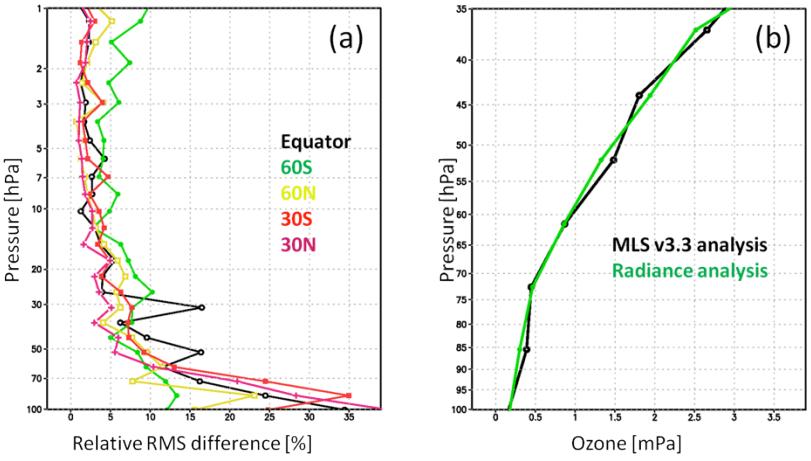

Figure 1: (a) The RMS relative difference between ozone from radiance assimilation and MLS version 3.3 assimilated ozone at selected latitude bands on August 8th 2009. (b) The lower stratospheric zonal mean equatorial ozone from radiance (green) and MLS version 3.3 (black) assimilation experiments calculated for the same analysis time. Note the different pressure range on the vertical axes in (a) and (b).

Figure 1(a) shows the zonal RMS difference between ozone from the radiance assimilation and an assimilation of MLS version 3.3 retrievals (control). The RMS difference is calculated along 5 latitude circles at a single synoptic time one week into the analysis and is divided by the averaged ozone from the control. The agreement is within 5% between 20 and 1 hPa except in the southern mid-latitudes where the differences reach 10%. In the lower stratosphere, the differences are reach 35%. While some of these differences can be attributed to the absence of an extinction retrieval in the current version of the algorithm, the large excursions seen in the tropical profile (black) at 30, 50, and 100 hPa may, in fact, indicate superior performance of the radiance assimilation.

The zonal mean ozone at the equator from the two experiments is shown for the lower stratosphere in Figure 1(b). Note a pattern of vertical oscillation in the control assimilation that is absent in the radiance assimilation. Such oscillations are artifacts in the version 3.3 of MLS retrievals that adversely affect the assimilated product. This is one example of an improvement from direct assimilation of radiances.

Development and Validation of Observing System Simulation Experiments at the GMAO

Ronald Errico, Nikki Privé, and King-Sheng Tai

Observing System Simulation Experiments (OSSEs) are designed to mimic the process of data assimilation. In applications of atmospheric data assimilation systems with regard to real observations, imperfect real observations are drawn from the real atmosphere to produce estimates of global atmospheric states at sequences of time. In an atmospheric OSSE, simulated observations with simulated errors are drawn from a simulated atmosphere (termed a "nature run" or "NR") and provided to a data assimilation system to produce estimates of those NR states. Since the OSSE deals entirely with simulations, it is not restricted to using only observations that actually exist. Also, the underlying "true" atmospheric state is known precisely. These two properties of the OSSE facilitate many types of informative experiments relevant to data assimilation and NASA's missions.

OSSEs may be used to help guide development of new instruments, as they may be performed during the planning stages. By estimating impacts of envisioned observations on data assimilation and forecast system performance, project requirements and design implications can be better determined. The OSSE setup may also be used to investigate more theoretical questions, as even impractical observations can be generated with relative ease; e.g., because the quality of the observations can be strictly controlled in the OSSE context, how the accuracy of data assimilation products depend on instrument error or deployment characteristics can be easily examined. Unlike when assimilating real observations, the NR states from which the OSSE observations are drawn are known perfectly and analysis errors can be explicitly and precisely determined. This OSSE property can therefore be used to greatly expedite development and testing of new data assimilation algorithms.

An OSSE has recently been developed at the GMAO. This OSSE uses a Nature Run generated by ECMWF as part of a multi-agency Joint OSSE project using a 2005 version of the ECMWF operational numerical weather prediction model. This 13-month Nature Run has been evaluated and found to be satisfactory for use in OSSEs. A full suite of synthetic observations with calibrated observational error has been created from the Nature Run to replicate the current atmospheric observational network. The Gridpoint Statistical Interpolation (GSI) data assimilation and GEOS-5 forecast model are used to ingest the synthetic observations and generate experimental forecasts.

It is imperative that a baseline OSSE be well validated. The OSSE should faithfully reproduce many metrics used to assess observations and data assimilation systems when similar existing observation types are considered. For past OSSEs, when validations have been performed, usually the best included a few data denial comparisons (i.e., corresponding observing system experiments) performed in OSSE and real contexts. In contrast, the GMAO OSSE has been extensively calibrated using a suite of different metrics and an iterative process in which the synthetic observations and their errors were tuned to behave realistically.

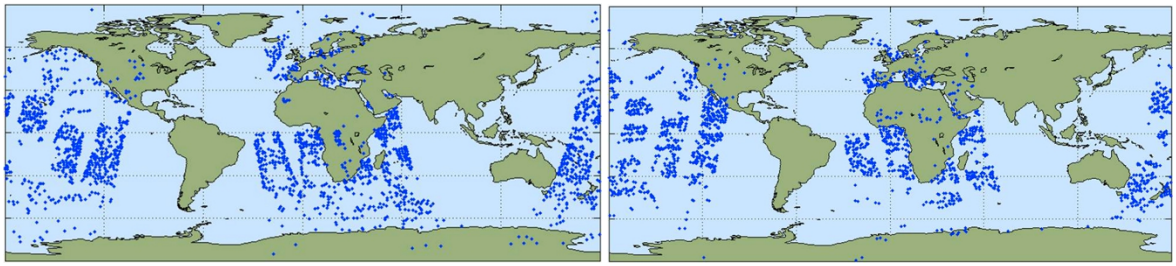

Figure 1: Locations of thinned and quality-controlled AIRS data for channel 295 for the 6-hour period centered on 18 UTC 12 July 2005 for real observations (left) and OSSE simulated observations (right).

Figure 1 shows a comparison of locations of real and simulated observations for a particular AIRS channel used by the GSI. Blank patches in the observing swaths indicate where data have been rejected by the quality-control algorithm that detects cloud-contaminated signals. These patches are not expected to correspond in the two data sets because where clouds are on a particular day in reality need not be where they are in the Nature Run simulation, since the only real aspects about the data known by the NR are the sun's position and sea-surface temperature. What is expected, however, is that the typical observation counts and qualitative nature of the location distributions are similar. That appears true in Figure 1.

The analysis increment, or analysis minus background, is a measure of how much work the observations do in changing the analysis state. Square roots of the zonal means of temporal variances of analysis increments for both zonal wind and temperature determined for July 2005 are presented in Figure 2. From left to right, results are presented for tropospheric values of real and OSSE temperatures and real and OSSE zonal winds. Although the OSSE results appear weakly deficient in most locations, the agreement is otherwise remarkably good. In order to obtain this level of agreement, for some observation types, it was critical to simulate their errors with spatial or channel correlations.

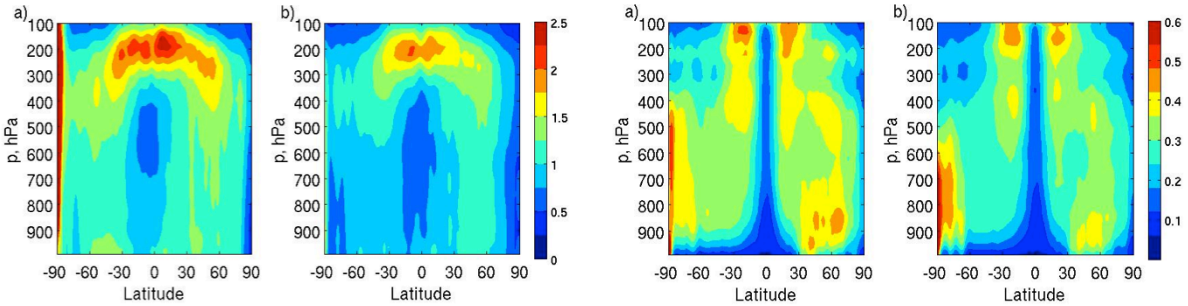

Figure 2: Square roots of the zonal means of temporal variances of analysis increments determined for July 2005 for (left to right) real and OSSE temperatures and real and OSSE zonal winds.

These and many other metrics validate the GMAO OSSE as a valuable tool for investigating present and planned observing and assimilation systems. Work is proceeding on several fronts, including extending the observational data set to include all 2012 operational data types, evaluating model error within the OSSE context, and improving the error simulation model and its parameters. Validations using other metrics are also being performed. The first OSSE application will be an estimation of the broad character of real analysis error in the GMAO data assimilation system.

Publications:

Errico, R.M., R. Yang, N. C. Privé, K.-S. Tai, R. Todling, M. E. Sienkiewicz, J. Guo, 2012: Development and validation of observing system simulation experiments at NASA's Global Modeling and Assimilation Office. *Q. J. Roy. Meteorol. Soc.,* (submitted).

Privé, N.C., R.M. Errico, K.-S. Tai, 2012: Validation of forecast skill of the Global Modeling and Assimilation Office observing system simulation experiment. *Q. J. Roy. Meteorol. Soc.,* (submitted).

Carbon Data Assimilation in the GSI Analysis System

Andrew Tangborn, Steven Pawson, and Ricardo Todling

The Gridpoint Statistical Interpolation (GSI) analysis system within GEOS-5 has not had the capability to assimilate trace gases other than ozone and water vapor. This project involves the initial steps towards extending this capability to assimilate observations for a number of species, starting with carbon monoxide (CO) tracer observations from the Measurement of Pollution in the Troposphere (MOPITT) on board NASA's EOS Terra spacecraft. MOPITT measures infrared radiation from the Earth's surface and atmosphere, and has been producing CO profile retrievals on 10 levels with global coverage since March 2000.

The MOPITT profiles are weighted through a vertical averaging kernel that quantifies the sensitivity of each retrieval to CO at different levels in the atmosphere. The peak sensitivity occurs near 500 hPa, with little sensitivity near the surface or upper troposphere. The assimilation system accounts for this sensitivity through the inclusion of the averaging kernel in the forward operator and its tangent linear and adjoint models. Trace gas assimilation in GEOS-5 differs from ozone assimilation in that the analyzed CO fields do not use the incremental analysis update (IAU) to adjust the model state. Instead, the CO analysis replaces the CO background field at each analysis time. The computational efficiency of this approach becomes important as large numbers of traces gases begin to be assimilated.

Initial testing of the CO assimilation has involved experiments with a simple background error covariance model, and assumes the background error standard deviation to be a percentage of the layer mean CO mixing ratio. This ensures that the largest error estimates are imposed in the surface layer, where flux errors are largest. These initial results will be used as a benchmark to compare with more sophisticated covariance modeling approaches that give some flow dependence to the errors.

The initial experiments consist of a set of 3-month assimilation runs for the period January-March 2009, in which the background error standard deviation is varied. The success of each experiment was judged by computing 6-hour forecast error statistics from the computed observed-minus-forecast (O-F) values for CO. An optimal case was identified in which the error estimates were 7.5% of the layer mean mixing ratio. Figure 1 shows the mean and standard deviation for this case, along with the O-F for a run in which the observations were treated as passive, and the observed-minus-analysis (O-A) for the optimal case. The assimilation shows mean and standard deviation reduction in the O-Fs at all levels. This indicates that the minimization within the GSI system is drawing the background fields towards the observations.

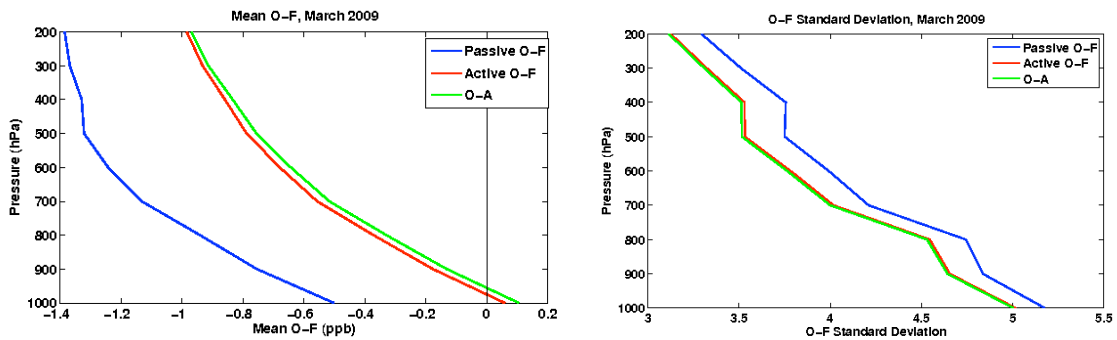

Figure 1: Mean (left) and standard deviation (right) of the O-Fs for the month of March 2009 from an assimilation run starting January 1, 2009. Each curve shows the 10 levels of the MOPITT retrieval minus forecast (or analysis). Passive observations (no CO assimilation) are shown in blue, forecasts from the assimilated CO are shown in red, and O-As are shown in green.

In order to determine whether the assimilation is producing more accurate CO fields, we need to compare the results with an independent data set. We use in situ observations from *In-Service Aircraft for a Global Observing System* (IAGOS), which is a global data set of CO observations obtained from instruments flying on commercial flights originating in Europe and flying around the globe. Comparisons with the initial assimilation run (Figure 2) show that mean errors decrease for CO outside of the boundary layer in the Southern Hemisphere, and in the Northern Hemisphere up to 40°N. Above 40°N mean errors are found to increase at all levels. This increase is likely due to the simple error covariance model being used, which tends to underestimate the background errors in the northern mid-latitudes. But the mainly positive impact of the MOPITT observations on the CO fields indicates that the analysis system is extracting useful information on the distribution of carbon monoxide in the troposphere.

Near term work will focus on moving to a flow dependent error covariance model, including CO retrievals from AIRS, IASI and other satellites, and extending the system to begin assimilating carbon dioxide.

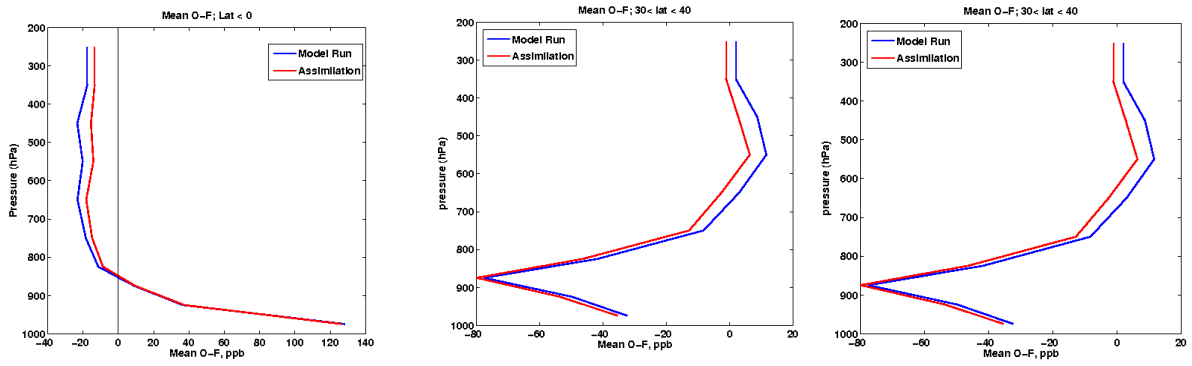

Figure 2: Mean O-Fs for independent IAGOS in situ CO measurements for (left) the SH, (middle) 0 - 30°N, and (right) 30 - 40°N. The blue curve is for the unconstrained model and the red curve is with MOPITT observations assimilated.

Assimilation of Passive and Active Microwave Soil Moisture Retrievals

Clara Draper, Rolf Reichle, Gabriëlle De Lannoy, and Qing Liu

Root-zone soil moisture is an important control over the partitioning of land surface energy and moisture. Previous studies have demonstrated that assimilating remotely sensed near-surface soil moisture can improve model profile soil moisture. These studies have focused on soil moisture data derived from either the passive microwave Advanced Microwave Scanning Radiometer for the Earth Observing System (AMSR-E) or the active microwave Advanced Scatterometer (ASCAT; or its predecessors).

Here, the assimilation of ASCAT and AMSR-E soil moisture is compared for the first time. For ASCAT, observations from the Technical University of Vienna are used, while for AMSR-E, X-band observations from the Free University of Amsterdam are used. Each of these data sets is assimilated over 3.5 years into the NASA Catchment land surface model, using an Ensemble Kalman Filter (EnKF). Soil moisture skill from each assimilation experiment is assessed against in situ soil moisture observations from the SCAN/SNOTEL network in the US (66 sites) and the Murrumbidgee Soil Moisture Monitoring Network in Australia (19 sites). Soil moisture skill is measured as the anomaly time series correlation coefficient with the in situ data (R).

Figure 1 shows the estimated R values and their 95% confidence intervals for the surface and root-zone soil moisture, from the assimilation of ASCAT, AMSR-E, and both. The results are benchmarked against an open-loop, and have been averaged by land cover type (based on MODIS land cover classifications). Across all 85 sites, assimilating ASCAT and/or AMSR-E data significantly improved the soil moisture skill (at the 5% level). In the root-zone, the mean skill was increased from 0.45 for the open-loop, to 0.55 for the assimilation of ASCAT, 0.54 for the assimilation of AMSR-E, and 0.56 for the assimilation of both.

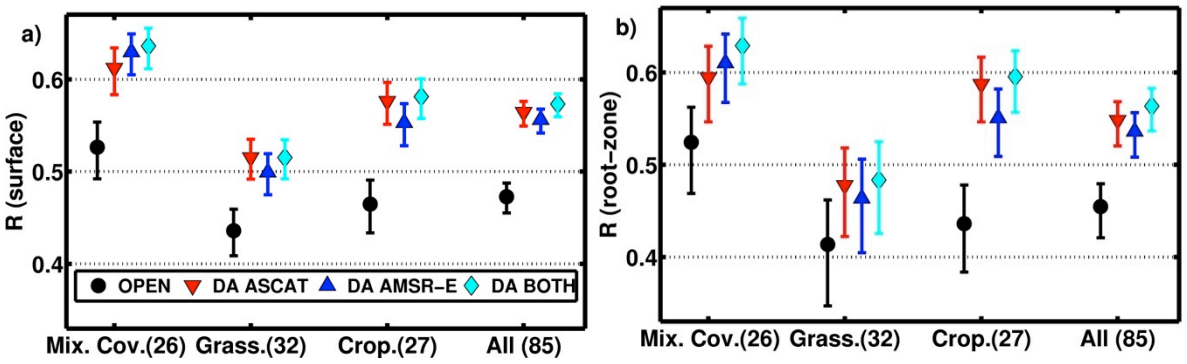

Figure 1: Mean skill for a) surface and b) root-zone soil moisture from the open-loop (ensemble mean, no assimilation), and the data assimilation (DA) of ASCAT, AMSR-E, and BOTH, averaged by land cover class, with 95% confidence intervals. The number of sites in each land cover class is given in the axis labels. Skill is based on all non-frozen days in the experiment period.

Assimilating the ASCAT or AMSR-E data also improved the mean R value over each individual land cover type, in most cases significantly. At the frequencies observed by AMSR-E and ASCAT, dense vegetation limits the accuracy of soil moisture observations, and so the improvements obtained over the mixed cover sites, which have 10-60% trees or wooded vegetation, are very encouraging. For each land cover type, the skill obtained from the assimilation of ASCAT or AMSR-E was very similar. Following the recent malfunction of the AMSR-E instrument, applications currently assimilating AMSR-E should then be able to switch to ASCAT data without loss of accuracy.

The combined assimilation (ASCAT and AMSR-E) generally matched or slightly exceeded the mean R from the single-sensor assimilation experiments. Consequently, for maximum accuracy and spatial coverage it is recommended that passive (AMSR-E or WindSat) and active (ASCAT) near-surface soil moisture be assimilated together, if possible.

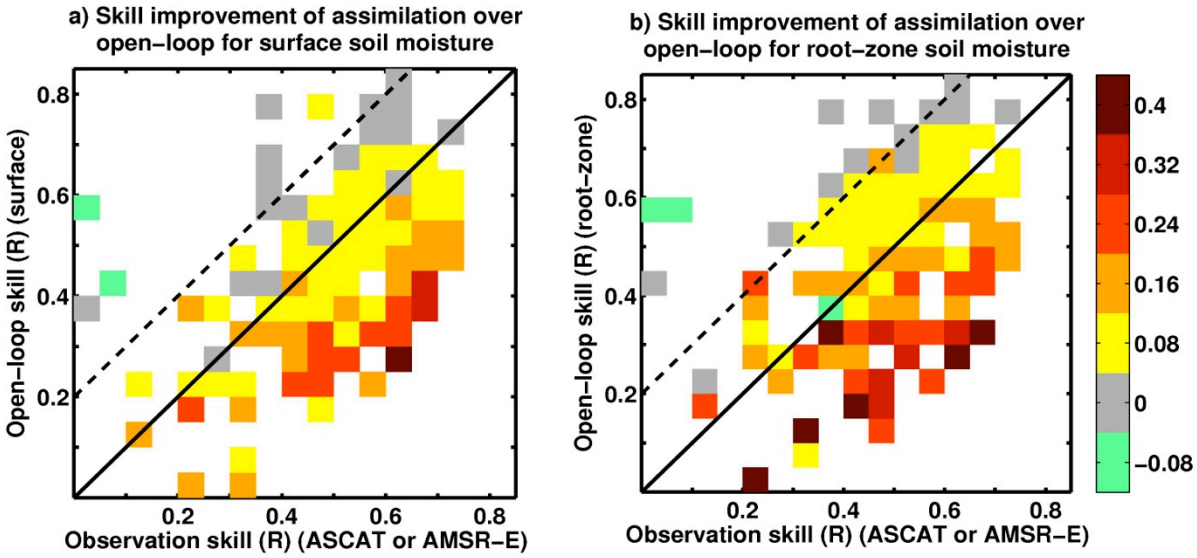

Figure 2: Skill improvement (ΔR) from assimilating either ASCAT or AMSR-E for a) surface and b) root-zone soil moisture, as a function of the open-loop and observation skill. Skill improvement is defined as the skill of the assimilation product minus the open-loop skill, with skill based only on days with data available from both satellites.

Finally, the contribution of the model and observation skill to the skill of the assimilation output was also examined. Figure 2 shows the skill increase (ΔR) relative to the open-loop model from the single-sensor assimilation of ASCAT or AMSR-E, as a function of the R of the open-loop and of the assimilated (ASCAT or AMSR-E) observations. In general, for a given combination of open-loop and observation skill, the skill gained through assimilation was slightly higher for the root-zone (Figure 2b) than for the surface soil moisture (Figure 2a). Also, where the satellite soil moisture skill was no more than 0.2 less than the open-loop skill (below the dashed lines), the assimilation improved the soil moisture skill, with larger improvements (up to 0.4) obtained as the observation skill increased relative to that of the open-loop. This result provides a practical demonstration of the minimum skill required for soil moisture observations to be beneficial in GMAO's land surface assimilation system.

Publication:

Draper, C.S., R.H. Reichle, G.J.M. De Lannoy, and Q. Liu, 2012: Assimilation of passive and active microwave soil moisture retrievals. *Geophys. Res. Lett.*, **39**, doi:10.1029/2011GL050655.

Multi-scale Assimilation of AMSR-E Snow Water Equivalent and MODIS Snow Cover Fraction Observations in Northern Colorado

Gabriëlle De Lannoy and Rolf Reichle (GMAO), Kristi Arsenault and Paul Houser (GMU), Sujay Kumar (Code 617), Niko Verhoest and Valentijn Pauwels (UGent)

Snow estimation in the Rocky Mountains is crucial to water supply in the Western United States. Satellite-based snow observations from two distinct sensors are used in an assimilation framework to analyse their benefit for fine-scale snow state estimation. Eight years (2002–2010) of Advanced Microwave Scanning Radiometer–EOS (AMSR-E) snow water equivalent (SWE) retrievals and MODIS snow cover fraction (SCF) observations are assimilated separately or jointly into the Noah land surface model over a domain in Northern Colorado. The results are validated against in situ observations at 14 high-elevation Snowpack Telemetry (SNOTEL) sites with typically deep snow and at 4 lower-elevation Cooperative Observer Program (COOP) sites.

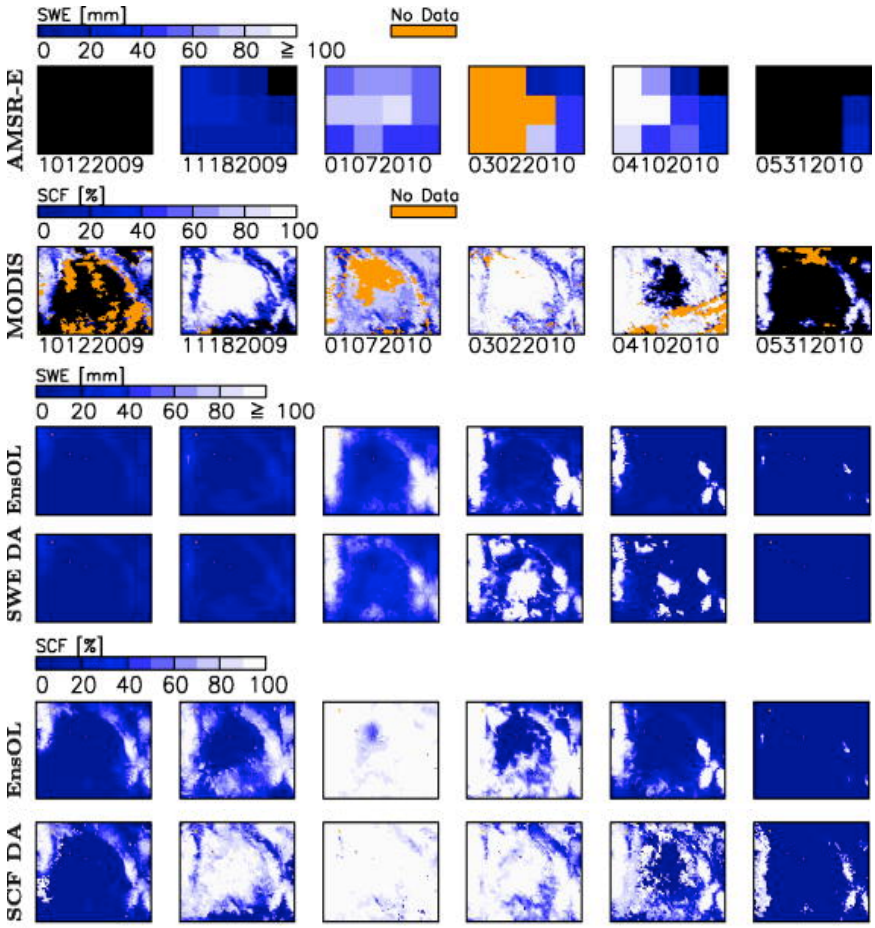

Figure 1: SWE (at 08:00 UTC) and SCF (at 17:00 UTC) fields for 5 days (MMDDYYYY) in the winter of 2009–2010. Black indicates the absence of snow. The top two rows show SWE and SCF satellite observations. The remaining rows show SWE (at 09:00 UTC) and SCF (at 18:00 UTC) for the Ensemble Open Loop (EnsOL) forecast and the analyses obtained through data assimilation (DA) of SWE or SCF without a priori scaling.

The nature of AMSR-E and MODIS snow observations is illustrated in Figure 1 for one snow season. AMSR-E retrievals are coarse-scale (25 km) SWE estimates, with data missing when the swath does not cover the study area. To estimate the snow at a fine model scale (1 km), we applied a distributed ensemble Kalman filter, which allows (i) downscaling the coarse-scale observations to the fine scale and (ii) propagating observed observations to unobserved areas, thus enabling smooth fine-scale SWE estimates. MODIS provides fine-scale estimates of SCF (not SWE), but only over cloud-free areas. To assimilate this indirect snow information, a snow depletion curve acts as the observation operator converting modeled SWE into SCF estimates. Unlike binary indicators of snow presence, the continuous SCF observations can be assimilated with an EnKF, except for snow-free or full cover conditions. We addressed these conditions by supplementing the EnKF with rule-based updates. Figure 1 shows that assimilation of coarse-scale AMSR-E SWE and fine-scale MODIS SCF observations both result in realistic spatial SWE patterns.

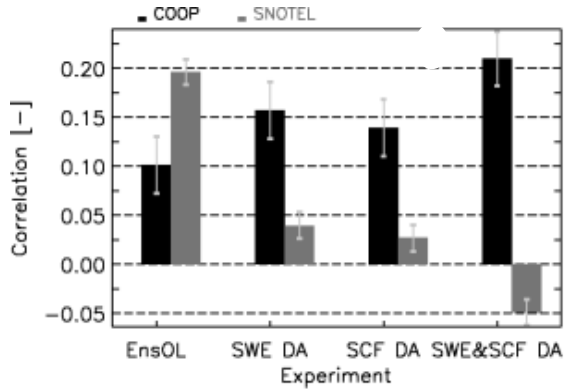

Figure 2: Time series correlation with COOP (black bars) and SNOTEL (gray bars) in situ observations for model forecasts (EnsOL) and assimilation estimates, computed over 8 winters (October–June 2002–2010) and averaged over the available sites. Also shown are 95% confidence intervals.

AMSR-E retrievals and the upscaled model SWE simulations show large climatological differences. In addition, the comparison of 1 km model simulations against point scale observations suffers from bias due to a different spatial support. To address these biases, experiments with scaled satellite data are also performed. The latter experiments show that the water balance is better preserved with anomaly assimilation than when unscaled ('raw') observations are assimilated.

The validation of the assimilation results at individual sites over the course of 10 years shows benefit for assimilation in shallow snowpacks, but not in deep snowpacks. Figure 2 shows that at COOP sites (with typically shallow snowpacks), AMSR-E SWE and MODIS SCF data assimilation are beneficial separately, and joint SWE and SCF assimilation yields significantly improved root-mean-square error and correlation values for scaled and unscaled data assimilation. In areas of deep snow where the SNOTEL sites are located, however, AMSR-E retrievals are typically biased low and assimilation without prior scaling leads to degraded SWE estimates (Figure 2). Anomaly SWE assimilation could not improve the interannual SWE variations in the assimilation results because the AMSR-E retrievals lack realistic interannual variability in deep snowpacks. SCF assimilation has only a marginal impact at the SNOTEL locations because these sites experience extended periods of near-complete snow cover. Across all sites, SCF assimilation improves the timing of the onset of the snow season but without a net improvement of SWE amounts.

Publication:

De Lannoy, G.J.M., R.H. Reichle, K.R. Arsenault, P.R. Houser, S.V. Kumar, N.E.C. Verhoest, and V.R. N. Pauwels, 2012: Multi-Scale Assimilation of AMSR-E Snow Water Equivalent and MODIS Snow Cover Fraction in Northern Colorado. *Water Resources Research*, **48**, W01522, doi:10.1029/2011WR010588.

GMAO Ocean Reanalysis

Guillaume Vernieres, Christian Keppenne, Robin Kovach, and Jossy Jacob

GMAO's ocean and sea-ice reanalysis provides initial conditions for our seasonal forecasts with GEOS-5. Naturally, the analysis also provides an estimate of ocean and sea-ice climate variability from 1980 to the present. The most recent reanalysis has been conducted with a hybrid of an ensemble optimal interpolation (EnsOI) technique and a new spatially adaptive forecast-error estimation (SAFE) methodology that functions as a cost-effective flow-adaptive alternative to our EnKF.

The EnsOI is used to assimilate vertical profiles of temperature and salinity (XBT, CTD, Argo) and along-track sea level anomalies from the AVISO merged product. The SAFE methodology is used to assimilate some of the surface observations such as sea surface temperature retrievals from Reynolds, sea-ice concentration from NSIDC and climatological sea surface salinity from WOD09.

For the EnsOI, background error covariances are estimated from a static ensemble, and flow dependency of the background error covariances is obtained through localization in temperature, salinity and density space. The static ensemble consists of the 20 leading EOFs of 186 forecast anomalies from coupled forecasts initialized from a previous analysis. SAFE determines error covariances from the local joint spatial distribution of model state variables and does not require multiple model instances to be run concurrently. The local covariance information can be complemented with temporal background error covariance estimates obtained by sampling the model state at regular intervals of a single model trajectory. The SAFE methodology includes iterative data adaptive algorithms that estimates both the error variance of each assimilated observation and the geometry of the region that each observation is allowed to influence. The error estimates are a function of how well each observation can be explained by other nearby observations. The adaptively derived geometrical information reflects how well each observation explains neighboring data.

The thermohaline circulation is a critical part of a climate system since it defines the poleward transport of heat by the ocean, as well as the circulation of water masses. The Atlantic meridional overturning circulation (AMOC) describes the pole-to-pole and vertical structure of that circulation in the Atlantic. Figure 1 shows that our estimate of the AMOC anomaly at 26°N (red line) is in good agreement with the estimate of the AMOC from the RAPID array measurements.

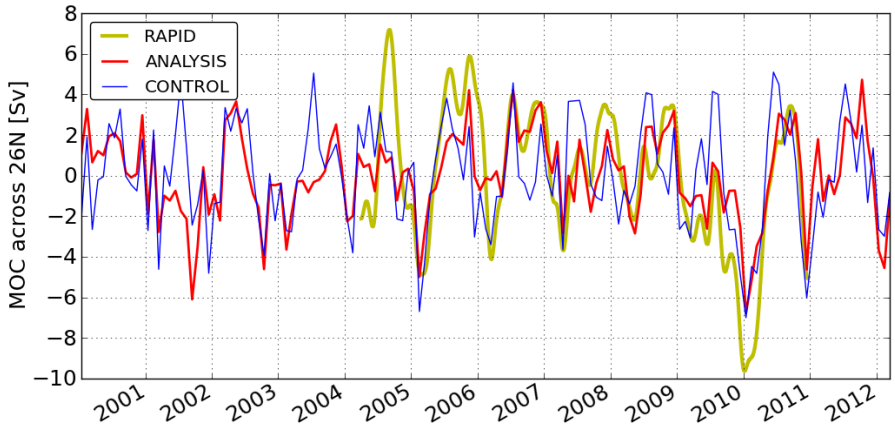

Figure 1: AMOC anomaly at 26°N. The blue line is the AMOC at 26°N calculated from an analysis that only assimilates sea surface temperature, climatological sea surface salinity and sea-ice concentration. The red line is the same estimate from the analysis described above.

Aerosol-Cloud Interactions within GEOS-5

Donifan Barahona and Andrea Molod
Andrew Gettelman, Hugh Morrison, Julio Bacmeister (NCAR), and Athanasios Nenes (GaTech)

Atmospheric aerosols can modify the radiative balance of the Earth. They alter the amount of solar energy reaching the surface as well as the thermal radiation leaving the Earth. They also alter the properties and global distribution of clouds by mediating the formation of cloud droplets and ice crystals. Clouds formed in polluted environments exhibit different properties from those formed in pristine air.

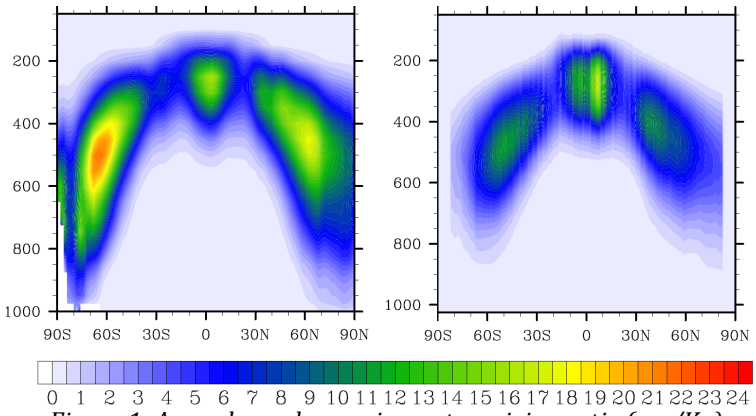

Figure 1: Annual zonal mean ice water mixing ratio (mg/Kg) from the GEOS-5 model with two-moment microphysics (left) and from CloudSat retrievals (right, courtesy of Frank Li, JPL).

Currently, GEOS-5 uses a single-moment (i.e., mass-based) cloud microphysics scheme to parameterize condensation, sublimation, evaporation, autoconversion and sedimentation of liquid and ice. This single-moment approach captures the main features related to the formation of stratocumulus decks and tropical storms, however it prevents the linkage of aerosol emissions to cloud properties and does not account for subgrid variability in cloud structure. To address this, the cloud microphysics has been updated using a two-moment scheme that explicitly calculates the *mass and number* of cloud ice and liquid, rain and snow (Barahona et al., 2012). The new implementation has significantly improved the prediction of microphysical variables like ice and liquid water content and cloud particle size, and of large scale variables like cloud fraction and cloud radiative forcing (Figure 1).

The new cloud framework also requires detailed modeling of complex aerosol activation processes. Below 0° C atmospheric clouds are made of both liquid droplets and ice crystals. Ice crystals form by the freezing of cloud droplets (homogeneous ice nucleation) and by direct ice nucleation on the surface of particles known as ice nuclei (heterogeneous ice nucleation). Whereas the former process occurs only at very low temperatures (below -40° C), the latter is active in most atmospheric conditions. The nature of ice nuclei and the concentration of ice crystals produced by heterogeneous ice nucleation are, however, uncertain, even though their impact on climate is significant. To address this, a new theoretical framework was developed to consistently describe heterogeneous ice nucleation and incorporate experimental results from different sources (Barahona, 2012).

The new formulation of the ice nucleation spectrum, i.e., the function linking the ice crystal number concentration to cloud formation conditions and aerosol properties, relies on a statistical view of the ice nucleation process. The novelty behind the new model is that ice nucleation in each aerosol particle is described using a distribution of freezing temperatures. Then, the average freezing temperature of the whole aerosol population is derived, greatly facilitating the calculation of the ice crystal number concentration in the cloud without neglecting all the complexity of the ice formation process. The new formulation reproduces several experimental results, and will improve the analysis of field campaign and laboratory data on ice nucleation.

Publications:

Barahona, D., A. Molod, A. Gettelman, H. Morrison, J. Bacmeister, and A. Nenes, 2012: A new description of cloud microphysics within the NASA GEOS-5. *GMDD* (submitted).

Barahona, D., 2012: On the ice nucleation spectrum. *Atmos. Chem. Phys.,* **12**, 3733-3752.

The Impact of Improved Ocean Surface Roughness in the GEOS-5 AGCM

Andrea Molod (GMAO), Chaim Garfinkel (Code 614), In-Sun Song, Luke Oman (Code 614)
Gary Partyka, and Max Suarez (GMAO)

The GEOS-5 AGCM is being used for a variety of applications at a wide range of horizontal resolutions. Recent improvements in the model algorithm depicting the relationship between the ocean surface roughness and the surface stress have resulted in improvements in the mean simulated climate at all resolutions, and in improvements of forecast skill and simulations of hurricanes at high resolution. Two fundamental changes in the ocean surface roughness model were implemented based on recent observations, laboratory experiments and theoretical considerations, one valid in a range of wind speeds typical of the Southern Ocean, the other valid at the high range of wind speeds observed in strong tropical cyclones.

The change in surface roughness in the mid-wind regime is illustrated in Figure 1, which shows the increase in roughness for wind speeds near 5-10 m/sec, described in Garfinkel et al. (2011) and based on recent observations in the Southern Ocean. The impact of this change on the simulated climatological surface wind speed is shown in Figure 2 with a comparison to estimates from the Special Sensor Microwave Imager (SSM/I). The error in surface wind speed from the control simulation, shown in Figure 2f, is largest in regions where the speeds are in the 5-10 m/sec range, and is reduced in the simulation using the new roughness, Figure 2c.

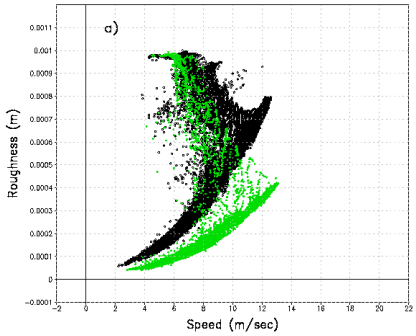

Figure 1: New (black) and old (green) three-hour mean ocean roughness in m vs. surface wind speed in m/sec.

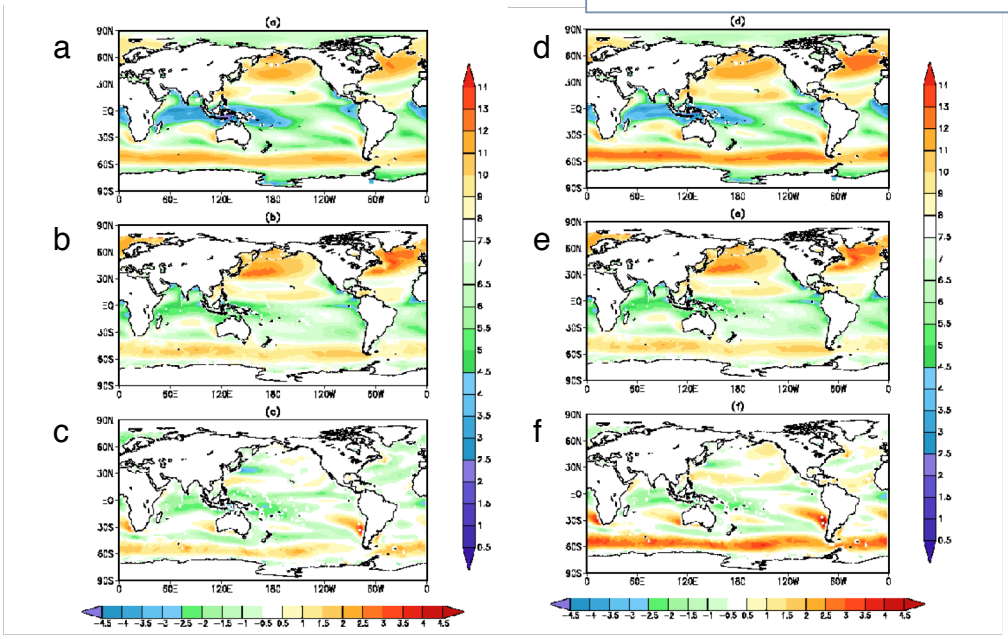

Figure 2: December-January-February climatology of surface wind speed in m/sec from simulations at 2° resolution: a) new roughness, b) SSM/I, c) the difference, new-SSM/I, d) old roughness, e) SSM/I, and f) the difference, old-SSM/I.

The ocean surface roughness in the high wind speed regime is relevant for simulations at 0.25º resolution, where the 3-hour mean wind speeds in tropical cyclone conditions typically reach 25 m/sec or more. Figure 3a shows the decrease in roughness for wind speeds higher than approximately 27 m/sec, described in Molod et al. (2012) and based on laboratory measurements and idealized model results.

The impact of the change in roughness at high wind speeds is shown through a series of short-term simulations of strong tropical cyclones. Figure 3b shows a summary of the difference in maximum wind speed and minimum sea level pressure reached in each of 8 simulations. For simulations with the highest wind speeds and lowest pressures, the wind speeds were increased by up to 6 m/sec and the minimum pressures reduced by up to 6 hPa in the simulations with the smaller roughness. Both of these measures of storm intensity are underpredicted in simulations at 0.25º resolution. In addition to improvements in metrics of storm intensity, the simulations with the smaller roughness also showed improvements in storm structure.

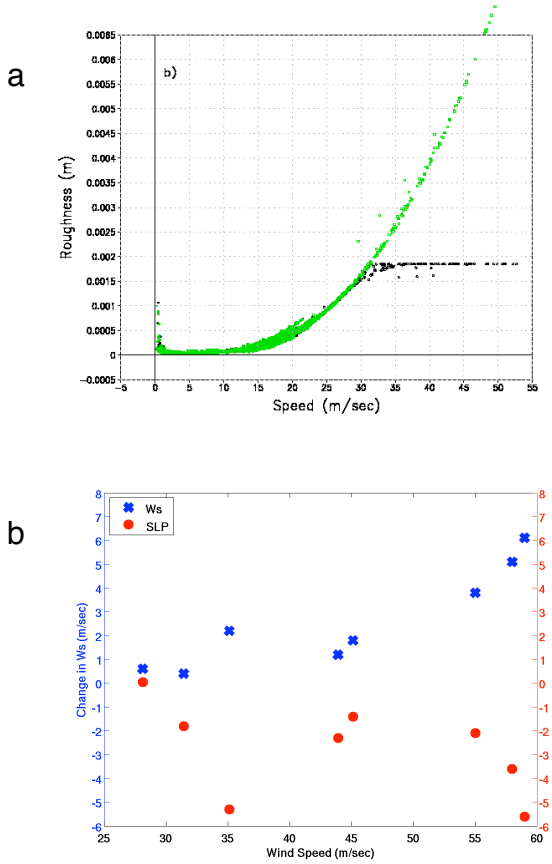

Figure 3: a) New (black) and old (green) three-hour mean ocean roughness in m vs. surface wind speed in m/sec from simulations at 0.25° resolution. b) Differences in wind speed in m/sec (blue) and sea level pressure in hPa (red) between tropical cyclone simulations using the new and old roughness algorithms.

Publications:

Garfinkel, C.I., A. Molod, L. Oman, and I.-S. Song, 2011: Improvement of the GEOS-5 AGCM upon upgrading the Air-Sea Roughness Parameterization. *Geophys. Res. Lett.,* **38,** L18702, doi:10.1029/2011GL048802.

Molod, A., M. Suarez, and G. Partyka, 2012: The Impact on GEOS-5 Hurricane Simulations of Limiting Ocean Roughness (*draft ms*).

GEOS-5 Coupled Climate Modeling

Yury Vikhliaev, Max Suarez, Andrea Molod, Bin Zhao, and Yoo-Geun Ham

The GEOS-5 Atmosphere-Ocean General Circulation Model (AOGCM) is designed to simulate climate variability on a wide range of time scales, from synoptic time scales to multi-decadal climate change. It has been tested in coupled simulations and data assimilation mode. Its main components are the GEOS-5 atmospheric model (AGCM) coupled to the catchment land surface model, MOM4, the ocean model developed by NOAA's Geophysical Fluid Dynamics Laboratory, and the sea-ice model (CICE) from Los Alamos National Laboratory. Every time step, these two components exchange fluxes of momentum, heat and fresh water through a "skin layer" interface. The skin layer module includes parameterization of the diurnal cycle and the thermodynamics of CICE.

Suites of climate predictions – on the seasonal timescale for the National Multi-model Ensemble prediction project and on the decadal timescale for the Coupled Model Intercomparison Project (CMIP5) – were conducted. A set of multi-decadal test runs under three different configurations were conducted:

(1) AGCM at 2.5˚ longitude × 2˚ latitude; OGCM at 1˚ longitude and latitude;

(2) AGCM at 2.5˚ longitude × 2˚ latitude; OGCM at 0.5˚ longitude and latitude; and

(3) AGCM at 1.5˚ longitude × 1˚ latitude; OGCM at 0.5˚ longitude and latitude.

Based on the analysis of preliminary runs, the seasonal climate predictions were conducted with configuration (3), and the decadal climate predictions with configuration (1). All simulations included a parameterization of river discharge and the aerosol model (GOCART). The model was spun up using the pre-industrial control simulation with 1950 boundary conditions. The mean state of the pre-industrial simulation was used as initial conditions for an ensemble of 20th century runs (1950-2011). The 20th century runs produce a realistic climate but with a stronger global warming response to increase of CO_2 concentration than observed (Figure 1).

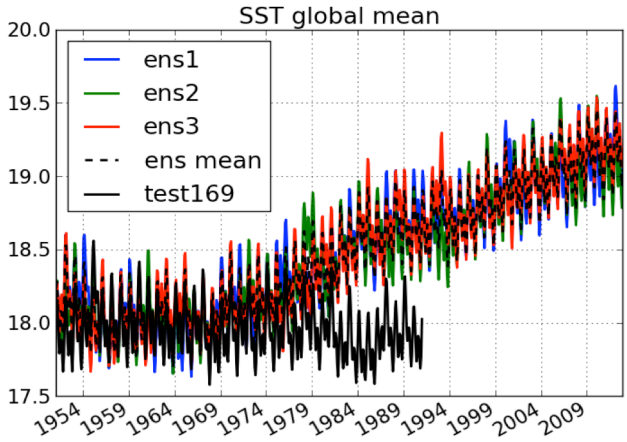

Figure 1: Global mean SST from 20th century simulations - three ensemble members (solid colored) and the ensemble mean (dashed black) - and from control simulation that uses 1950 forcings (solid black).

Analysis of the decadal forecasts revealed potential predictability of the North Atlantic climate up to several years (Ham et al., 2012). The ability of the GEOS-5 AOGCM to predict climate on decadal time scales is limited by the errors in simulating the realistic ocean circulation, such as inability to maintain the observed vertical ocean stratification in high latitudes and inability to simulate the realistic meridional overturning circulation. Currently, an effort is undertaken to ameliorate these problems.

Publication:

Ham, Y.-G., M.M. Rienecker, M.J. Suarez, Y. Vikhliaev, B. Zhao, J. Marshak, G. Vernieres, and S.D. Schubert, 2012: Decadal prediction skill in the GEOS-5 forecast system. *Climate Dynamics* (submitted).

Integration of Carbon Physics into the GMAO Land Model

Randal Koster and Greg Walker (GMAO), Peter Thornton (Oak Ridge National Laboratory)

The land surface is a key player in the global carbon cycle. Carbon fluxes into and out of land surface ecosystems are considerable, with strong temporal and spatial variations; inherent difficulties in measuring these fluxes at continental scales constitute a principal uncertainty in the global carbon budget. To promote land-carbon research, the GMAO has implemented a vegetation physics module into its land surface modeling system. In addition to tracking land carbon storage and (eventually) providing carbon fluxes to the atmospheric model in coupled simulations, the module allows vegetation phenology (e.g., the lushness of the vegetation) to respond to variations in the atmospheric forcing.

The vegetation module is adapted from the NCAR Community Land Model (CLM4). We have integrated the photosynthesis, conductance, and carbon treatments from CLM4 into a reworked version of the GMAO's Catchment land surface model (LSM) to produce a merged LSM that simulates the fluxes and states of water, energy, and carbon together. The new system maintains the unique water and energy balance framework of the Catchment LSM and is thus quite distinct from the NCAR model. One unique feature of our merged model, for example, is the ability to simulate different degrees of phenological development in different sub-regions of a given land element, capturing (for example) the greater lushness of vegetation in riparian zones. Relative to the original Catchment LSM, the new system also features separate prognostic variables in the canopy and ground surface and a broader catalogue of vegetation types for a more accurate characterization of the land boundary.

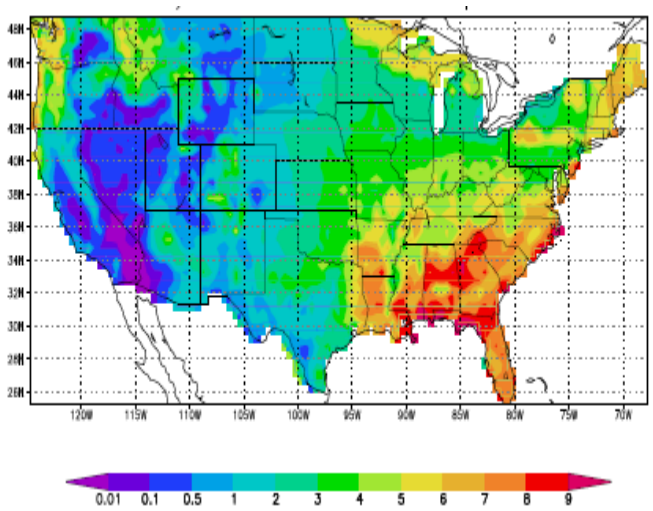

Figure 1: July distribution of leaf area index (LAI) produced by the Catchment LSM fitted with the CLM4 dynamic vegetation physics.

The combined system has been run offline using a 56-year dataset of meteorological forcing over the continental United States. Following an extensive spin-up period (looping over the 56-year period multiple times out to ~2000 years, to allow carbon prognostic variables to equilibrate), the model-simulated energy, water, and carbon fluxes were aggregated into monthly and seasonal means for analysis. Figure 1 shows the mean leaf area index (LAI) simulated by the system for July. Lusher vegetation appears where expected, e.g., in the wet regimes of the Southeastern U.S., and low LAI values properly appear in the dry west. Evaluation against observations is difficult given the imperfect nature of the observations themselves; various datasets (e.g., from AVHRR), however, suggest that the LAIs shown in the southeast are too high. Additional work is needed to address discrepancies between simulated and observed fields, a common issue with dynamic vegetation models.

The offline forcing system is uniquely suited for LAI and carbon sensitivity analyses. To exercise the model, we performed a series of experiments in which we arbitrarily removed various aspects of forcing variability from our offline simulations; in one particular experiment, for example, we replaced the precipitation forcing with its climatological seasonal cycle. The resulting reductions in the variability of LAI and carbon states were then quantified. These experiments indicate that precipitation variability has by far the greatest impact on the interannual variability of LAI and carbon storage. Variations in temperature, radiation, and other forcing variables were found to have a relatively negligible impact.

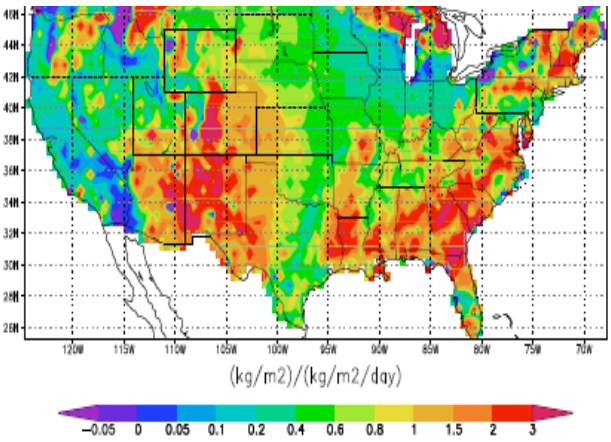

Figure 2: Numerical derivative of total carbon change with respect to a change in mean precipitation, as determined from offline simulations with the new model.

In another sensitivity simulation, the precipitation forcing was increased by a very small amount throughout the simulation period. By computing the resulting change in the carbon storage and dividing that change by the imposed precipitation change, estimates of the derivative of total carbon storage with respect to mean precipitation were derived. These derivatives are provided in Figure 2. An increase in mean precipitation (as induced, perhaps, by anthropogenic forcing) would lead to increased uptake of carbon in the Deep South and in areas of the Southwest. In areas of the Far West (parts of California and Washington), however, an increase in precipitation would lead to a loss of carbon. Similar experiments suggest a similar pattern of change (though of smaller magnitude) associated with a *decrease* in precipitation variability.

Future land model development in the GMAO will be centered on this system. An upcoming step will be to couple the system to the atmospheric model and, through multi-decadal simulations, determine the degree to which dynamic vegetation phenology feeds back on simulated climate variability.

Reference:

Koster, R.D., G.K. Walker, and P.E. Thornton, 2011: Energy and Water Balance Controls over Interannual Phenology and Carbon Flux Variations. Presented at WCRP Open Science Conference, 24-28 October 2011, Denver, Colorado, USA.

Development of Land Model Physics Using Continental-Scale Observations of Hydroclimatic Means and Variability

Randal Koster and Sarith Mahanama

Evaporation tends to increase as a soil surface gets wetter. Similarly, a wetter soil allows rainfall to be converted more efficiently into streamflow. To simulate the global hydrological cycle properly – to explore, for example, how streamflow might vary in a modified climate – climate models need to capture these soil water impacts on evaporation and runoff accurately. Unfortunately, the precise nature of these impacts is largely unknown; evaporation at the large (100 km) scale, for example, is essentially unmeasured (at least not directly), and soil moisture measurements at that scale, available only from satellites, focus only on the top few millimeters of soil. As a result, the complex approaches used by land surface modelers to relate evaporation and runoff to soil moisture at the large scale are largely untested.

In this study, these complex approaches are stripped to their barest forms and then examined within the context of a simple water balance model. In a standard simulation, the simple model is first provided with simple functions relating evaporative fraction ($\lambda E/R_{net}$, the ratio of latent heat flux to net radiation at a given time step) and runoff fraction (Q/P, the ratio of runoff to precipitation at a given time step) to soil moisture content. The model is then driven with observations-based forcing covering multiple decades across the conterminous United States. Through a controlled series of simulations using a variety of imposed functions, the simple model reveals the sensitivity of various hydrological statistics to the structure of these functions, i.e., to the assumptions a land modeler might make regarding evaporation and runoff production.

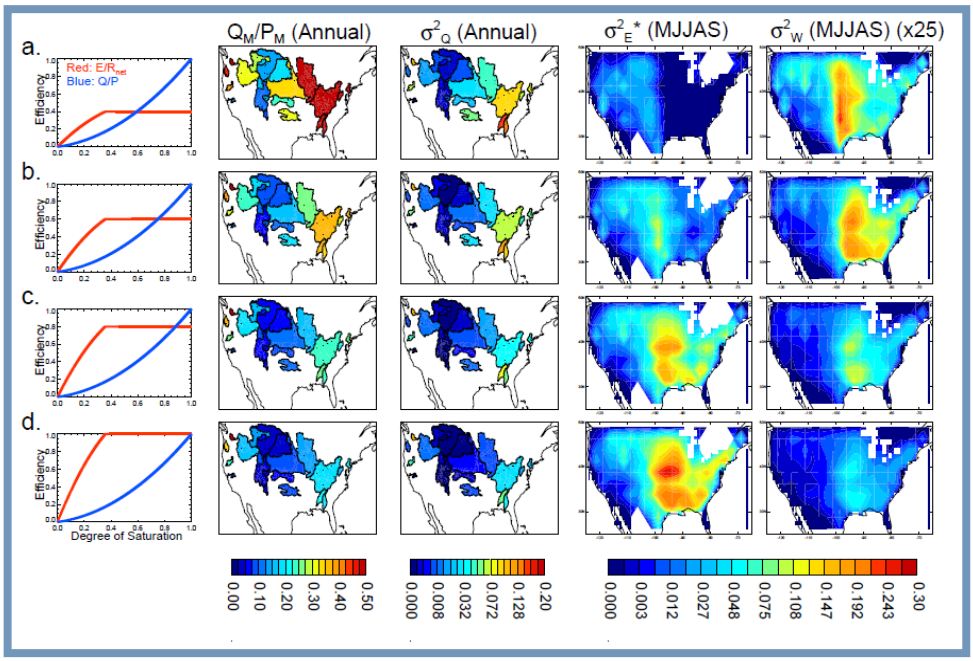

Figure 1: Impact of the "height" of the lE/R_{net} relationship on hydrological means and variability. a. Plots showing the imposed pairing of lE/R_{net} and Q/P relationships in a specific WBM experiment (first panel) and the resulting spatial distributions of average runoff ratio (Q_M/P_M, dimensionless), runoff variance (s^2_Q, mm^2/day^2), evaporation variance (s^2_E, mm^2/day^2), and soil moisture variance (s^2_W, cm^2). b. Same, but for a second experiment. c. Same, but for a third experiment. d. Same, but for a fourth experiment.*

An example is shown in Figure 1. Each row corresponds to a single simulation with the simple model, with the first panel of the row showing the evaporation and runoff functions imposed in the simulations. (More precisely, the red curve shows how evaporative fraction is made to vary with the degree of

saturation in the soil, whereas the blue curve shows how the runoff ratio is made to vary with degree of saturation.) The second panel in a given row shows the resulting values of Q_M/P_M, the ratio of annual mean runoff to annual mean precipitation, in several large U.S. basins. Q_M/P_M is seen to increase in the progression of experiments (a through d), reflecting the fact that evaporation is progressively made easier (as indicated by the increased height of the red curves in the first panels). Runoff and soil moisture variances decrease (third and fifth columns) and evaporation variance increases (fourth column) with the ease of generating evaporation. An interesting facet of the variance sensitivities is that they reflect not only the changes in the mean but also the specific shapes (particularly the slopes) of the imposed evaporation and runoff functions – sometimes in subtle ways.

Observations-based estimates (either direct or proxy) exist for Q_M/P_M and for runoff, evaporation, and soil moisture variances. A comparison of observational estimates with those of the simple model provides an indication of the evaporation and runoff functions that effectively operate in nature. In turn, a comparison of the identified "nature" functions with the effective functions used by a climate model's land surface component provides a means for improving the latter – it shows how the land surface model's effective functions would have to change to allow the generation of a more realistic simulation of hydroclimatic statistics. We employed such a development strategy with the GMAO's Catchment land surface model. The final results of the development exercise are shown in Figure 2. The revised Catchment model's simulation of Q_M/P_M and of the hydrological variances is seen to be quite good. Prior to the revision, the model's simulation of runoff ratios and runoff variances in the eastern U.S. were too low.

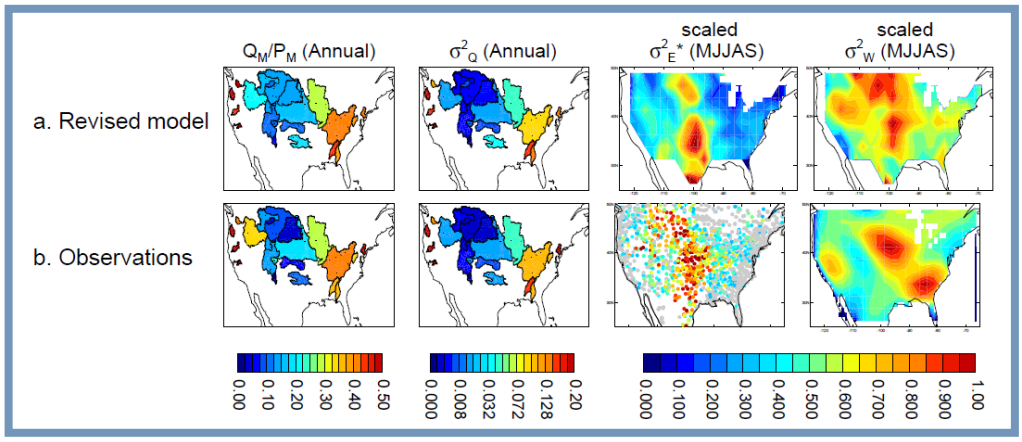

Figure 2: a. Simulated hydroclimatic statistics produced by the Catchment land surface model after its improvement through the simple water balance analysis procedure. The first panel shows Q_M/P_M (dimensionless), the second shows the variance of simulated annual runoff (s^2_Q, mm²/day²), the third shows the moisture-related variance of simulated warm season evaporation (s^2_E, no units), and the fourth shows the variance of simulated warm season soil moisture content (s^2_W, no units) b. Observations-based spatial distributions of Q_M/P_M, s^2_Q, s^2_E*, and s^2_W. The values of s^2_E* or s^2_W within a given panel are scaled arbitrarily to allow the simulated and observed spatial patterns (the feature of relevance, given the proxy nature of these data) to be more easily compared.*

By providing a means for indirectly estimating the large-scale relationships operating in nature between evaporation and soil moisture and between runoff and soil moisture – relationships that simply cannot be quantified through direct measurement – the simple water balance model framework serves as a useful testbed for evaluating and improving the land surface models used in the simulation of climate, with potential positive impacts on the climate simulations themselves. Future plans involve applying the approach to a broad range of land surface modeling systems as part of a funded multi-model effort.

Publication:

Koster, R.D., and S.P. Mahanama, 2012: Land-surface Controls on Hydroclimatic Means and Variability. *J. Hydrometeorol*. (submitted).

Implementation and Testing of the Modal Aerosol Model (MAM) Aerosol Microphysics Component in GEOS-5

Anton Darmenov and Arlindo da Silva

Atmospheric aerosols are important radiatively active agents that can also affect clouds, the water cycle, and land and ocean biogeochemistry; however their net effect on the climate remains uncertain. The diverse and dynamic nature of aerosols has been studied using in situ and remotely sensed data, and chemical transport models. The GEOS-5 model and data assimilation systems coupled with GOCART currently model organic carbon, black carbon, sulfate, sea-salt and mineral dust aerosols. However, GOART provides a simplified representation of aerosols – aerosol species are externally mixed and only basic aerosol processes are considered.

A more sophisticated aerosol model is now being implemented in GEOS-5. The representation of the aerosol size distributions in the new model follows the modal aerosol dynamics approach (Whitby and McMurry, 1997). Several log-normal modes with fixed widths are used to represent internally (within a mode) and externally (between modes) mixed aerosol species. The modal approach is computationally efficient and is less prone to the numerical diffusion problems of other methods. The model predicts the aerosol number and mass mixing ratios for sulfate, ammonium, primary and secondary organic matter, sea salt and dust aerosol components. The total number and mass concentration in each aerosol mode are used to calculate the spatially and temporally varying size distributions. The model also distinguishes between interstitial and in-cloud attachment states and provides the means of physically consistent treatment of aerosol dynamics and aerosol-cloud interactions. Aerosol microphysical processes include nucleation, coagulation, gas uptake and chemical aging following the Modal Aerosol Model (MAM) aerosol microphysics core (Liu et al., 2011). Dry and wet removal are treated explicitly using the wet size and density or the size of the cloud droplets of the interstitial and in-cloud aerosols respectively.

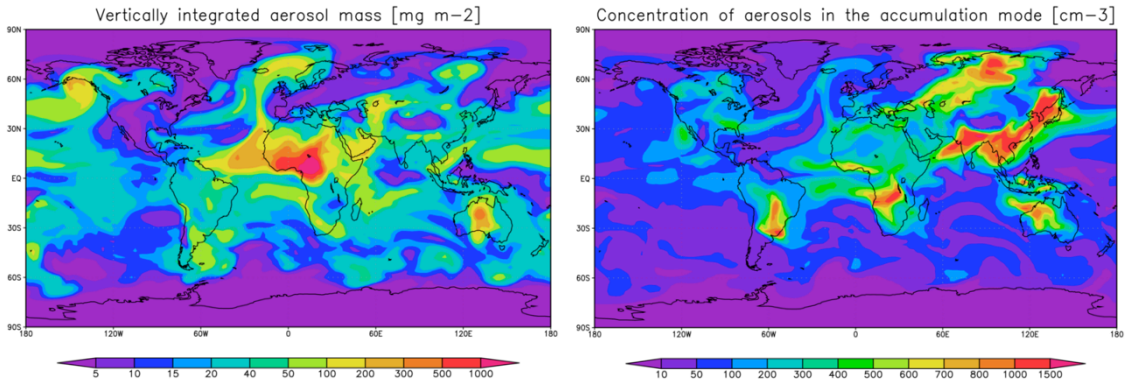

Figure 1: The GEOS-5/MAM configuration has seven log-normal modes (Aitken, accumulation, primary carbon, fine dust, fine sea salt, coarse dust and coarse sea salt) designed to represent internally and externally mixed fine and coarse particles that can be either suspended in clear or cloudy air or contained within hydrometeors. Shown are total aerosol burden (left) and number concentration of aerosols in the accumulation mode in the surface model layer (right).

The current GEOS-5/MAM implementation has been successfully run online (Figure 1) using the stable (Fortuna) and development (Ganymed) versions of the GEOS-5 system.

References:

Whitby, E.R., and P.H. McMurry, 1997: *Aerosol Sci. Technol.*, **27**, 673–688.

Liu, X., and co-authors, 2011: *Geosci. Model Dev. Discuss.*, **4**, doi:10.5194/gmdd-4-3485-2011.

Correction of Excessive Precipitation over Steep and High Mountains in Atmospheric Models

Winston Chao

Excessive precipitation over steep and high mountains (EPSM) is a known problem in atmospheric models (e.g., Ma et al., 2011). We found that the most important cause is a missing upward transport of heat out of the boundary layer due to the vertical circulations forced by the daytime upslope winds. These upslope winds, forced by the heated boundary layer, are associated with large subgridscale topographic variation. Without such subgridscale heat ventilation, the resolved upslope flow in the boundary layer generated by surface sensible heat flux is excessive and, combined with the high moisture content of the boundary layer, results in excessive moisture transport toward mountaintops.

We have parameterized the ventilation effects of the subgridscale heated-slope-induced vertical circulation (SHVC) by removing heat from the boundary layer and depositing it in layers higher up when topographic variance exceeds a critical value and when the surface sensible heat flux is upward. The heat is removed from the boundary layer at a fraction of the surface sensible heat flux. This fraction is zero when the sub-grid topographical standard deviation (TSD) is less than 300 m and is 95% when the TSD is greater than 400 m. Values in between are linearly interpolated. Heat thus removed from the boundary layer is deposited in a deep layer whose bottom is at least 1.5 km above the surface. The specifics of the parameterization design are determined partly by previously published meso-scale model simulations and partly by tuning. Tests using GEOS-5 with a 2°×2.5° grid show that the EPSM problem is largely solved. Figure 1 shows that excessive precipitation over the Andes and New Guinea in DJF is removed. Similar results are obtained over the Himalayas and other highlands in JJA (Chao, 2012).

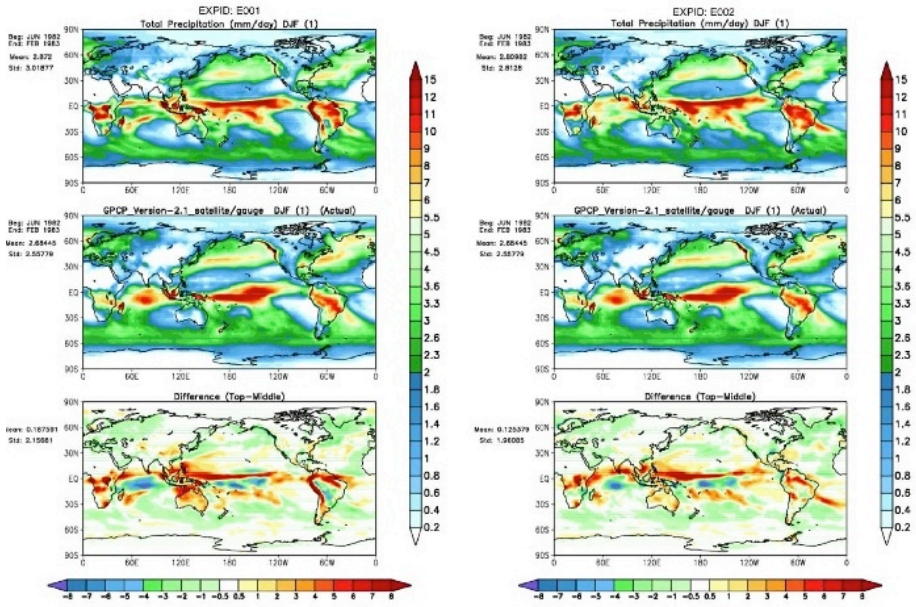

Figure 1: Precipitation field (mm/d) for one DJF season before (left) and after (right) our treatment. Top: the model results; middle: GPCP observations; bottom: the differences between the two. The vertical color bar is for the upper and middle panels.

While the mechanical effects of subgridscale topographic variations have long been recognized and incorporated in AGCMs as envelope topography and the gravity-wave and blocked-flow drag parameterizations, the corresponding thermal effects should also be incorporated.

References:

Ma, H.-Y., and co-authors, 2011: *Climate Dyn*., doi:10.1007/s00382-010-0813-3, **37**,187–203.

Chao, W.C., 2012: Correction of excessive precipitation over steep and high mountains in a GCM. *J. Atmos. Sci.,* doi:10.1175/JAS-D-11-0216.1 (in press).

Estimation of Surface Pressure Uncertainty in Meteorological Analysis Products in Support of the ASCENDS Mission

Lesley Ott, Hailan Wang, and Steven Pawson

NASA is currently planning the next generation carbon dioxide satellite mission, Active Sensing of CO_2 Emissions over Nights, Days, and Seasons (ASCENDS), to improve understanding of the natural processes driving the variability of carbon sources and sinks. This knowledge will enhance the ability to predict and model long term changes in the carbon cycle. ASCENDS will be based around lidar measurements of column CO_2 density but an open question is whether or not a companion oxygen lidar measurement is needed to accurately translate the CO_2 measurement into a high precision column concentration required for accurate source estimation. Because the oxygen measurement would significantly increase the mission's cost and complexity, alternative approaches, including using surface pressure fields produced by meteorological analyses instead of an accompanying oxygen measurement, are being considered. This study aims to quantify the error or uncertainty contained in meteorological surface pressure analysis products which will be used by the ASCENDS project team to assess the need for the oxygen lidar measurement.

Surface pressure observations are collected routinely from aircraft weather reports, radiosondes, and land and ocean surface stations, with the greatest density of observations over North America and western Europe. GEOS-5 and other meteorological analysis systems ingest thousands of these observations daily. In areas where data are available, observation minus analysis statistics computed from MERRA provide a quantitative assessment of analysis error, which is typically less than 2 hPa. However, in many other regions, particularly over oceans and less populous land regions, surface pressure data are sparse, making it difficult to assess potential errors in analysis products. In order to assess surface pressure errors in data sparse regions where objective evaluation is difficult, we have compared three different analysis products. Six-hourly fields are taken from MERRA; the Climate Forecast System Reanalysis (CFSR) from NCEP; and the operational analysis from ECMWF for January, April, July, and October 2009. Because the three analyses are provided on different horizontal grids, the CFSR and ECMWF fields have been regridded to the MERRA grid (2/3° longitude × 1/2° latitude) using an area-weighted interpolation method. Additionally, because of differences in the topography maps used by the different systems, a simple correction term based on the hypsometric equation is added to the ECMWF and CFSR products to translate them to MERRA's topography map.

Figure 1 shows an analysis of the difference in estimated surface pressure among the three analyses for January 2009. Differences largely reflect gradients in surface elevation despite the use of a common latitude/longitude grid for comparison. The correction term which accounts for differences in the underlying topography used in the analyses greatly reduces differences in surface pressure but is not able to eliminate them entirely, especially in areas where large gradients in topography may occur within a model grid cell. In some of these isolated areas, differences between the analyses can be greater than 10 hPa. Over most ocean and land regions without large topography variations, differences in surface pressure are less than 2 hPa. The greatest variability in multi-model mean surface pressure occurs in the mid- to high latitudes of both hemispheres. The greatest variability in the range of surface pressure values also tends to be located in these areas, particularly over the Southern and Arctic Oceans and in regions of the North Atlantic where few observations are available to constrain the analyses. The three analyses have also been compared with independent observations of surface pressure not included in the assimilation, where available. At several tropical and northern hemisphere mid-latitude ground stations operated by the Department of Energy's Atmospheric Radiation Measurement (ARM) program, all three analyses compare favorably with observations, with errors less than 2 hPa.

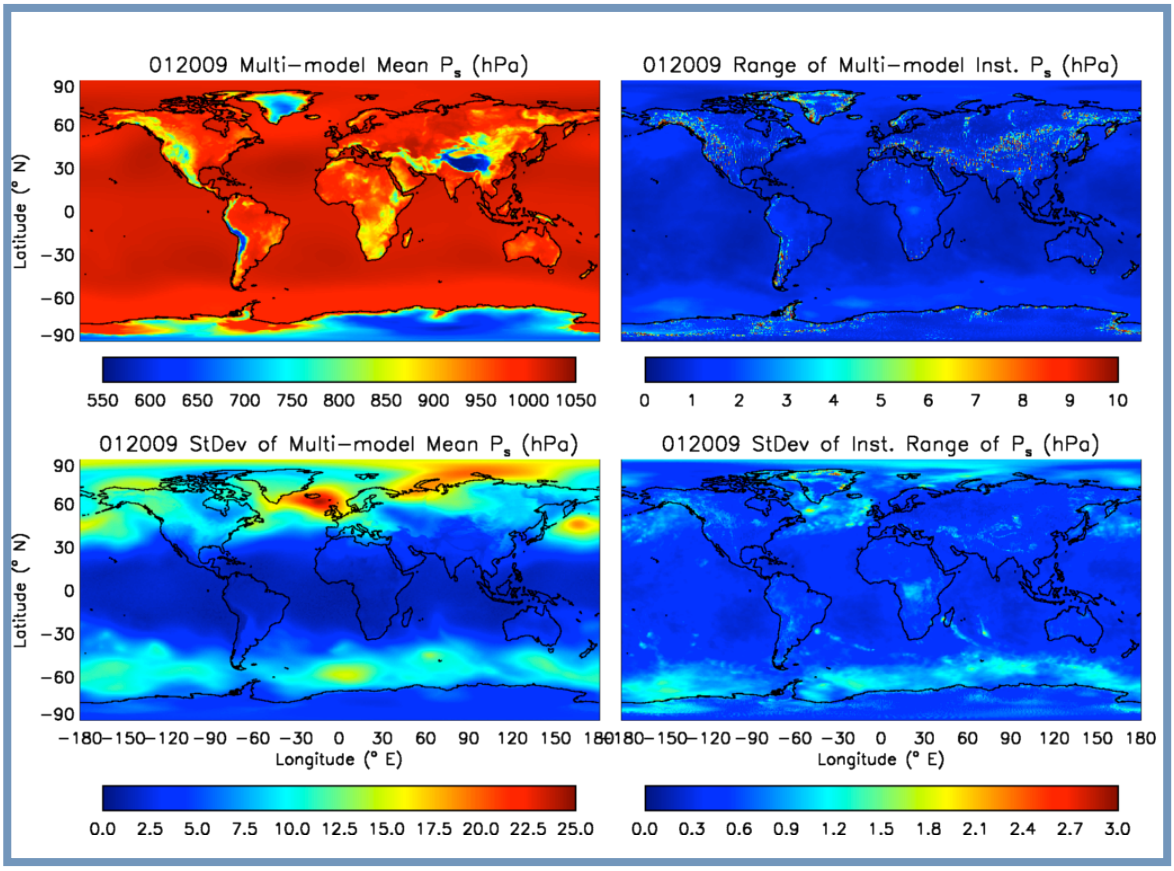

Figure 1: Multi-model mean (top left) and range (top right) of surface pressure for January 2009 calculated using instantaneous 6-hour MERRA, CFSR, and ECMWF fields. Bottom plots show the standard deviations of the mean (left) and range (right) quantities.

In addition to the examination of multi-model analysis differences, a high-resolution GEOS-5 global simulation was analyzed to understand how high resolution satellite measurements might compare to a lower resolution global model grid cell. The 5-km surface pressures were aggregated into 25 and 50-km areas representative of grid box sizes in current and planned analysis products, and the maximum surface pressure differences between the high and low resolution grids calculated. As in the multi-model analysis comparison, the largest spatial representation errors were found in regions of significant topography variations though errors over oceans could reach ~2 hPa when anticyclones with strong pressure gradients were present. Probability distribution functions show that 95% of 50-km grid cells had spatial representation errors less than 2 hPa; when 25-km grid cells were considered, errors were reduced by approximately 50%.

The results of this study suggest that uncertainty in analysis surface pressure products is fairly small (typically less than 2 hPa), both in regions where data is available for evaluation and in data sparse regions such as southern hemisphere land masses and oceans. Areas with large topographic gradients pose the greatest challenge for satellite missions which plan to use surface pressure from meteorological analyses. Spatial representation errors are likely to be significantly reduced by the use of higher resolution analysis products currently being developed in the GMAO and elsewhere.

Representation of the Middle-to-Upper Stratosphere in MERRA

Steven Pawson

Space-based radiance observations in MERRA outnumber the in-situ observations by several orders of magnitude (Rienecker et al., 2011). At high altitudes the number of observations decreases substantially, and above about 30 km there are almost no in-situ observations available for the analyses. The realism of MERRA analyses thus depends on the successful use of deep-layer radiance observations from the Stratospheric Sounding Unit (SSU) on the Tiros Operational Vertical Sounder (TOVS) and the Advanced Microwave Sounding Unit (AMSU-A) on Advanced TOVS (ATOVS) platforms. The approximate peak sensitivities of these instruments, for near-nadir observations in a standard atmosphere, are shown in Figure 1. TOVS/SSU data were available from 1979, on the Tiros-N and NOAA-6 through -14 platforms, with the ATOVS/AMSU-A observations beginning on NOAA-15 in 1998. NOAA-14 SSU channels 1 and 2 were used alongside AMSU-A data until 2004.

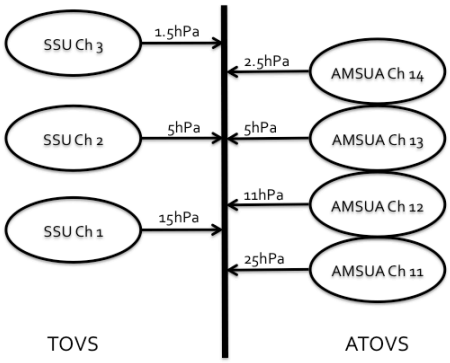

Figure 1: Schematic of the peak sensitivities for the SSU (Ch. 1-3) and the AMSU-A (Ch. 11-14). Note that the vertical structure of the averaging kernels is different for the two instruments.

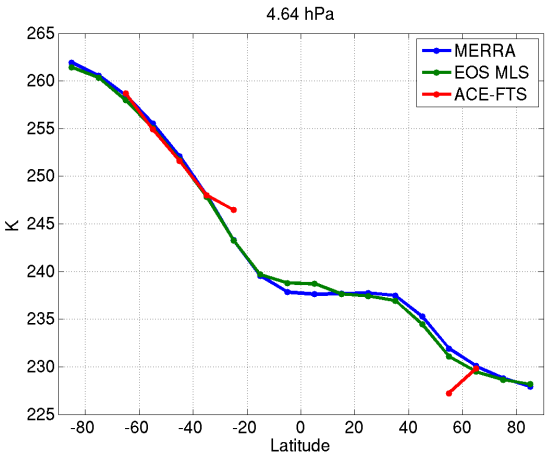

Figure 2: Comparison of January 5-hPa, zonal-mean temperature for 2005-2009. Curves are for MERRA (blue), EOS-MLS (green) and ACE-FTS (red). Plot by M. Schwartz, NASA JPL.

MERRA is being evaluated using independent data. The zonal-mean temperature near 5 hPa in January 2005-2009 (Figure 2) shows that MERRA is in close agreement with NASA's Earth Observing System Microwave Limb Sounder (EOS-MLS: Waters et al., 2006). MERRA also agrees well with the sparse data from the Atmospheric Chemistry Experiment Fourier Transform Spectrometer (ACE-FTS: Bernath et al., 2005). Comparisons with ERA-Interim (Dee et al., 2011) reveal a similar agreement at 5 hPa. This demonstrates that the assimilation of AMSU-A radiances into GEOS-5 leads to realistic and robust temperature analyses near 5 hPa in MERRA. This is helped by the use of variational bias correction for these radiances (see Rienecker et al., 2011). At lower pressures this result does not hold: near 2 hPa there are larger discrepancies between MERRA, EOS-MLS and ERA-Interim. Manney et al. (2008) showed that the stratopause dynamics are not well represented at times of disturbances. There is thus less confidence in MERRA temperatures at 1 hPa and lower pressures than there is at 5hPa and higher pressures.

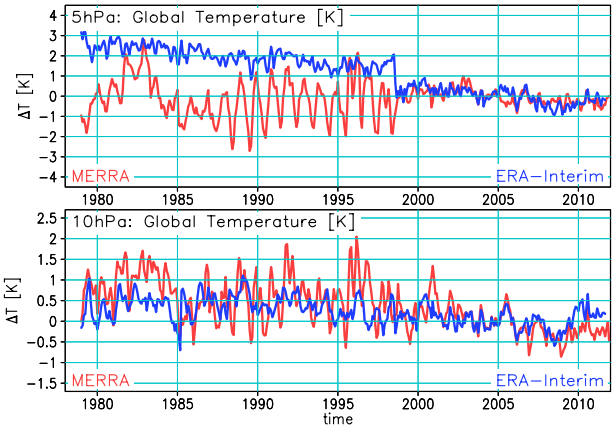

Figure 3: Time series of global-mean temperature anomaly at 5 hPa (top) and 10 hPa (bottom) for MERRA (red) and ERA-Interim (blue). The mean annual cycle for 2005-2009 is subtracted.

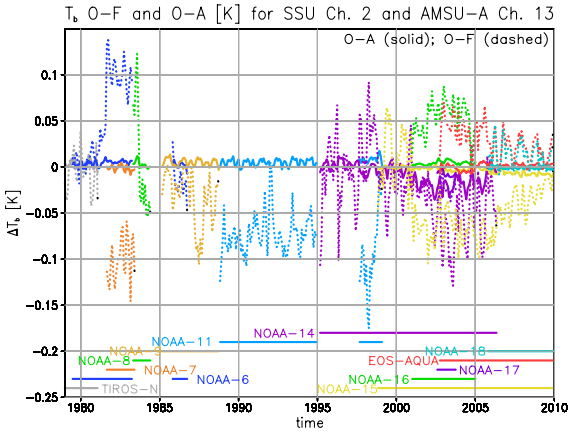

Figure 4: Time series of O-F (dashed) and O-A (solid) of the brightness temperatures for SSU Channel 2 and AMSU-A Channel 13, colored according to the platform making the observations.

After 1998, the global-mean temperature (at 5 hPa and 10 hPa) is very similar in MERRA and ERA-Interim (Figure 3). ERA-Interim shows a strong temperature decrease of about 2 K in 1998, whereas MERRA retains a similar mean temperature, but the mean annual cycle changes abruptly. Time series of O-F and O-A for MERRA (Figure 4) reveal good stability in the ATOVS era. These results show that the AMSU-A data assimilation is stable in MERRA and consistent with that in ERA-Interim. The same is not true of TOVS/SSU. MERRA temperatures fluctuate in the 1980s, when five short-lived SSU instruments in different orbits are used. With only NOAA-11, the analysis is quite stable through much of the 1990s. NOAA-14 provides similar stability until the ATOVS instruments are available, when the magnitude of O-A increases, suggesting that the treatment of SSU radiances in MERRA is inconsistent with the treatment of AMSU-A radiances. The TOVS-to-ATOVS transition happens differently in MERRA from in ERA-Interim, implying that additional development is needed to successfully integrate the SSU radiances into reanalyses.

References:

Bernath, P.F., and co-authors, 2005: Atmospheric Chemistry Experiment (ACE): Mission overview. *Geophys. Res. Lett.*, **32**, L15S01, doi:10.1029/ 2005GL022386.

Dee, D.P., and co-authors, 2011: The ERA-Interim reanalysis: configuration and performance of the data assimilation system. *Q. J. Roy. Meteorol. Soc.*, **137**, 553–597. doi: 10.1002/qj.828.

Manney, G.L., and co-authors, 2008: The Evolution of the Stratopause During the 2006 Major Warming: Satellite data and Assimilated Meteorological Analyses. *J. Geophys. Res.*, **113**, D11115, doi:10.1029/2007JD009097.

Rienecker, M.M., and co-authors, 2011: MERRA - NASA's Modern-Era Retrospective Analysis for Research and Applications. *J. Climate*, **24**, 3624–3648. doi: 10.1175/JCLI-D-11-00015.1

Waters, J.W., and co-authors, 2006: The Earth Observing System Microwave Limb Sounder (EOS MLS) on the Aura Satellite. *IEEE Trans. Geosci. Rem. Sens.*, **44**, 1075-1092.

National Climate Assessment (NCA): Evaluating Reanalyses for Contributions to US Regional Climate Assessment

Michael Bosilovich

The National Climate Assessment (NCA) aims to bridge the divide between scientific data development / research activities with the applied decision makers through the synthesis of climate information and to increase the understanding about what is known and unknown about climate change while building climate science capacity in regions of the United States and sectors of applications. The observational analysis data products developed at the GMAO provide a synthesis of satellite and in-situ observations across weather and climate time scales. While there are any number of uses of such data in research and applied science, uncertainties and limitations still exist. The GMAO interacts with the NCA providing both data and expertise in the utilization of observational analyses and retrospective analyses, and receives feedback on the development of metrics and variables important to decision-making.

The GMAO's NCA effort began in 2011, developing an evaluation of reanalyses for use in regional climate studies for the United States. The initial evaluation focused on summer seasonal variability of precipitation and temperature because summer is a challenging season for all atmospheric model predictions, but especially for precipitation. MERRA summer precipitation generally correlates well with gauge-only observations in most regions, but especially in the northwestern United States (Figure 1). Further statistical comparisons show that the northwestern high correlations are also related to springtime El Niño - Southern Oscillation (ENSO) signals, and can be reproduced across many reanalyses. The correlation of MERRA to ENSO persists into the Midwestern United States, but the Midwest observations diverge from ENSO. Hence, MERRA has weak correlation to observations in the Midwest. In general, reanalyses are too highly correlated to ENSO across much of the United State. Likely, the models need to improve their representation of land-atmosphere interactions and also that of the mesoscale convection that produces precipitation. Surface temperature is found to be a robust quantity across all reanalyses, owing to the assimilation of radiosonde and other data sources. Reanalyses with land analysis of station observations, however, do reproduce the interannual variations more closely.

In requesting input, NCA also asked for confidence levels to be considered for data products. Quantifying the uncertainty of reanalyses has been a long outstanding research issue. For precipitation, we consider independent validation, relying on correlation, variance, bias and even trend. The summertime results are clearly regionally dependent, but may provide useful information to decision makers. NCA suggested several categories of confidence, and Figure 2 represents our first attempt at applying those to GMAO's analyzed data. Regionally, NW shows medium high confidence, owing to the close ties with antecedent ENSO conditions in the Tropical Pacific Ocean and attendant large-scale circulation. The NGP region is also reasonably related to ENSO, but hampered by an overestimate (bias) in the mean precipitation. The SE and MW regions could be classified as medium-low confidence, owing to excessively high correlation to ENSO and significant bias. Since reanalyses tend to be internally correlated, we can expect these results to hold for related atmospheric properties, such as cloudiness, radiation and surface turbulent fluxes.

In the coming year, the most recent version of the GMAO operational analysis system will retrospectively analyze the period from 2004 to the present, incorporating more observations than presently in MERRA and at higher spatial resolution, to the benefit of regional assessments. The processing of the data is scheduled to begin by late summer 2012.

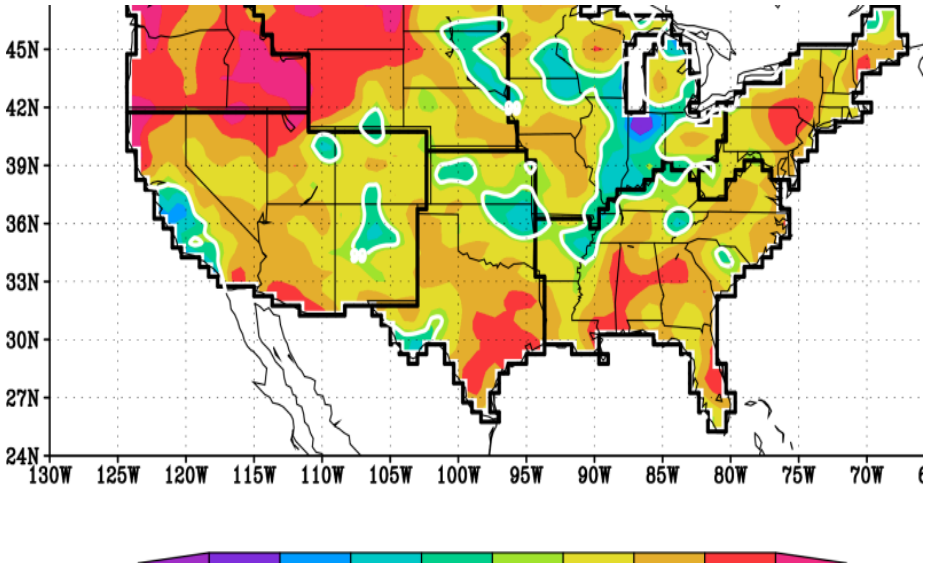

Figure 1: Correlation of MERRA summer seasonal precipitation for 33 years to gauge observations (Climate Prediction Center), where the white contour indicates the 99% significance level. The black outlines denote NCA-defined regions.

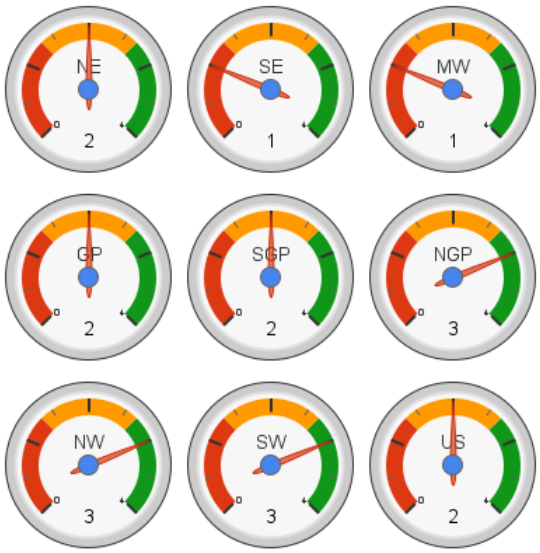

Figure 2: Schematic of the regional confidence levels of interannual variability of MERRA summertime precipitation, based on correlation, variance, bias and trend compared with observations (1 low, 2 medium low, 3 medium high, 4 high).

Reference:

Bosilovich, M.G., 2012: Regional Climate and Variability in NASA MERRA and Recent Reanalyses: US Summertime Precipitation and Temperature. A Report Submitted to the National Climate Assessment. http://gmao.gsfc.nasa.gov/projects/NCA/.

Comparison of Atmospheric Moisture Transports From Reanalyses for the North Polar Cap

Richard Cullather and Michael Bosilovich

A quantitative depiction of the atmospheric hydrologic cycle over the Arctic basin has significant relevance to a variety of weather and climate-related investigations. Although differences in surface moisture flux estimates among reanalyses have narrowed, large discrepancies persist among contemporary products. These discrepancies are associated with a poor representation of cold climate physical processes in global data assimilation models. In contrast to prognostic surface fluxes from reanalyses, atmospheric moisture transport and convergence are generally considered to be more stable variables, and are a more direct product of data assimilation. Additionally, moisture transport provides additional information that relates the surface flux to atmospheric circulation. In this study, a comparison of reanalysis moisture transport and convergence fields over the north polar cap (70°N – 90°N) is made using MERRA, ERA-Interim, and the CFSR. The comparison is conducted over the period 1989-2009. A focus is placed on the mean spatial and temporal variability of the vertically-integrated flux and convergence fields. Comparisons are made with previous studies using rawinsonde and satellite data.

The vertically-integrated atmospheric moisture transport may be computed as

$$\overline{\widetilde{Q}} = \overline{\frac{1}{g}\int_0^{P_{sfc}} (q\widetilde{V})\, dp}\ .$$

For an annual average, the line integral of the meridional moisture transport across the 70°N parallel is equal to the surface moisture flux, expressed as

$$\overline{E - P} = \oint \overline{\widetilde{Q}} \cdot \hat{n}\, dl\ .$$

The monthly-averaged total transport is a pre-computed quantity in MERRA. Mean and eddy components have been computed. The NCAR climate analysis section has computed the total transports for ERA-Interim and CFSR.

While the zonal distribution across 70°N shows MERRA and ERA-Interim to be in good agreement for particular locations, large differences in magnitude and sign are noted between CFSR and the other reanalyses (Figure 1). The zonal average for MERRA and ERA-Interim differ by 7%. Discrepancies in CFSR are largest in the Barents Sea, where the sign of annual mean transports is reversed.

Differences in moisture transport are assessed in the context of recent atmospheric circulation anomalies in the central Arctic associated with the perennial sea ice decline (Figure 2). Anomalous high-pressure patterns in summer have resulted in decreased atmospheric moisture convergence. Small but robust increases in October are associated with the presence of more open water at the onset of colder temperatures. The trends in autumn are in general agreement with model predictions.

Reference:

Cullather, R., and M. Bosilovich, 2012: A comparison of atmospheric moisture transports from reanalyses for the north polar cap. 4th World Climate Research Programme International Conference on Reanalyses, 7-11 May, Silver Spring, Maryland.

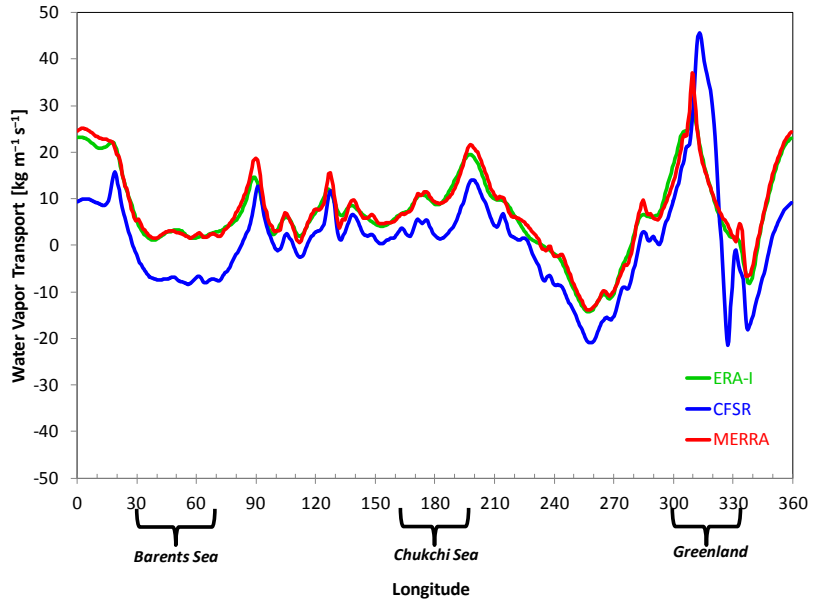

Figure 1: Annual mean distribution of meridional atmospheric moisture transport across 70°N, in kg m⁻¹ s⁻¹.

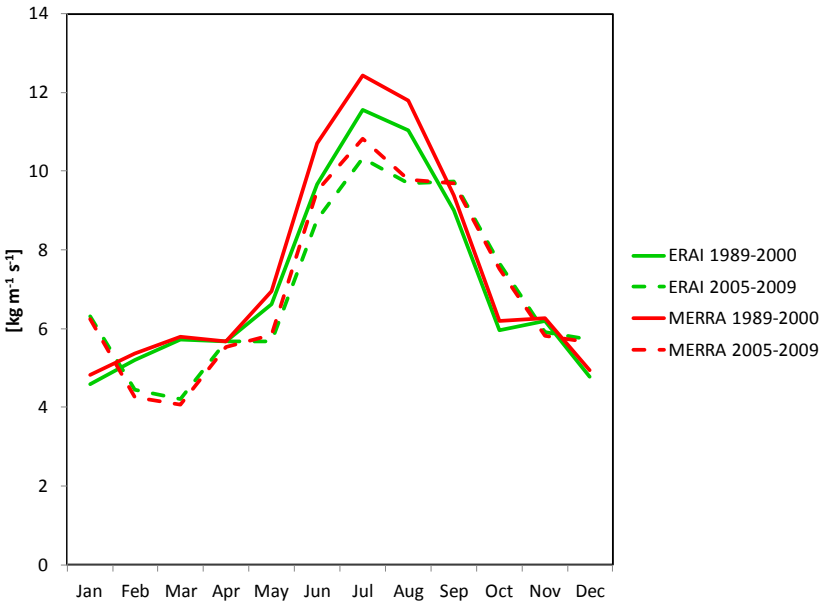

Figure 2: The moisture transport annual cycle in ERA-Interim and MERRA for two time periods shown.

The MERRA-Land Data Product: Assessment and Enhancement of MERRA Land Surface Hydrology Estimates

Rolf Reichle, Randal Koster, Gabriëlle De Lannoy, Barton Forman, Qing Liu, Sarith Mahanama, and Ally Toure

MERRA is a state-of-the-art reanalysis data product that provides, in addition to atmospheric fields, global estimates of soil moisture, latent heat flux, snow, and runoff for 1979-present. A supplemental and improved set of land surface hydrological fields ("MERRA-Land") was generated by re-running a revised version of the land component of the MERRA system (Reichle et al., 2012). Specifically, the MERRA-Land estimates benefit from corrections to the precipitation forcing with the global gauge-based NOAA Climate Prediction Center "Unified" (CPCU) precipitation product and from revised parameter values in the rainfall interception model in the Catchment Land Surface Model, changes that effectively correct for known limitations in the MERRA surface meteorological forcings.

With a few exceptions, the MERRA-Land data appear more accurate than the original MERRA estimates and are thus recommended for those interested in using MERRA output for land surface hydrological studies. As an example, Figure 1 examines the drought conditions experienced across the western United States and along the East Coast. The MERRA and MERRA-Land drought indicator shown in the figure is derived by ranking, separately for each grid cell, the normalized, monthly mean root zone soil moisture anomalies for June, July, and August of 1980 through 2011 and converting the rank into percentile units. For comparison, the drought severity assessed independently by U.S. Drought Monitor is also shown. The figure clearly demonstrates that MERRA-Land data are more consistent with the Drought Monitor than MERRA data.

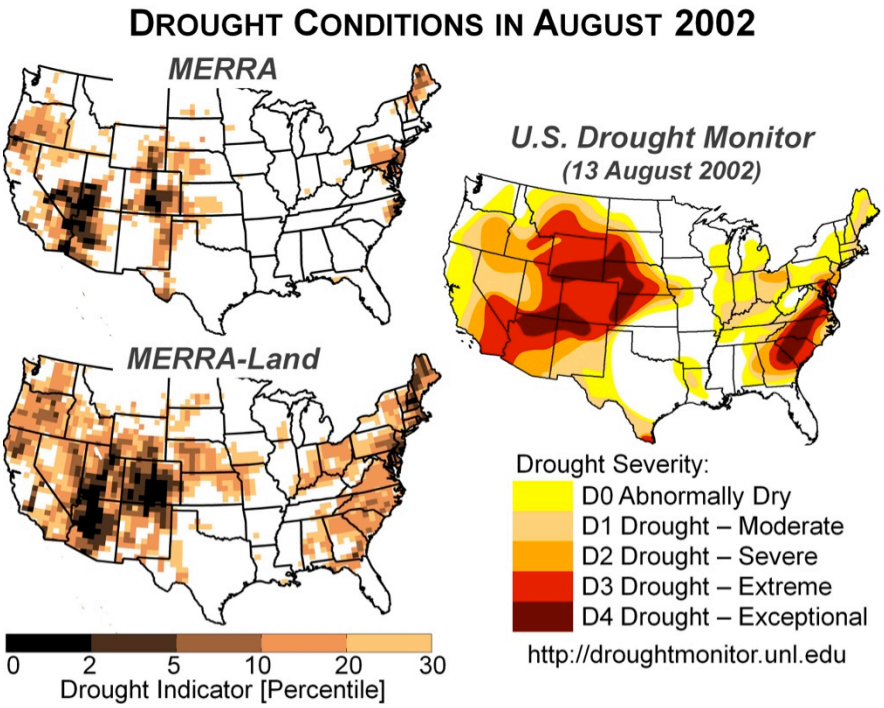

Figure 1: Drought indicator derived from (top left) MERRA and (bottom left) MERRA-Land root zone soil moisture estimates for August 2002. Darker colors indicate more severe drought conditions. MERRA-Land estimates are more consistent than MERRA estimates with an independent drought assessment from the US Drought Monitor for 13 August 2002 (right).

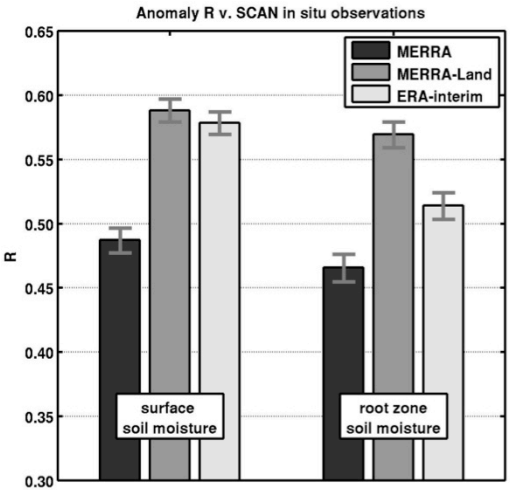

Figure 2: Skill (pentad anomaly R; dimensionless) of MERRA, MERRA-Land, and ERA-Interim estimates (2002-2009) versus SCAN in-situ surface and root zone soil moisture measurements. Error bars indicate approximate 95% confidence intervals.

A quantitative analysis of the skill (defined as the correlation coefficient of the anomaly time series) in land surface hydrological fields from MERRA and MERRA-Land was conducted against observations and compared to the skill of ERA-Interim. Figure 2 shows that MERRA-Land and ERA-Interim root zone soil moisture skills (against in-situ observations at 85 U.S. stations) are comparable and significantly greater than that of MERRA. Figure 3 shows that runoff skill (against naturalized stream flow observations from 18 U.S. basins) of MERRA and MERRA-Land is typically higher than that of ERA-Interim. Throughout the northern hemisphere, MERRA and MERRA-Land agree reasonably well with in-situ snow depth measurements (from 583 stations) and with snow water equivalent from an independent analysis (not shown).

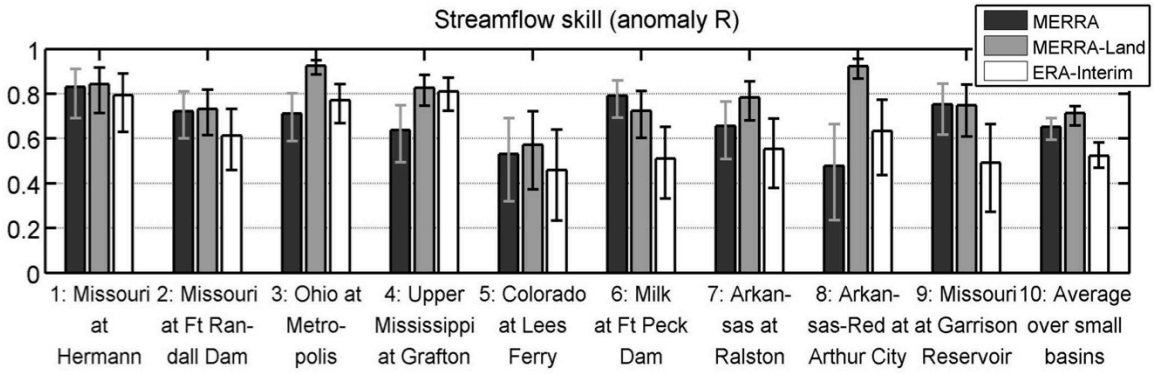

Figure 3: Seasonal anomaly time series correlation coefficients for runoff estimates from MERRA, MERRA-Land, and ERA-Interim. See Table 1 of Reichle et al. (2011) for more information on the basins and time periods examined.

Publications:

Reichle, R.H., R.D. Koster, G.J.M. De Lannoy, B.A. Forman, Q. Liu, S.P.P. Mahanama, and A. Toure, 2011: Assessment and enhancement of MERRA land surface hydrology estimates. *J. Climate,* **24**, 6322-6338, doi:10.1175/JCLI-D-10-05033.1.

Reichle, R.H., 2012: The MERRA-Land Data Product. Available at http://gmao.gsfc.nasa.gov/research/merra/file_specifications.php.

Global Surface Ocean Carbon Estimates in a Model Forced by MERRA

Watson Gregg, Nancy Casey, and Cecile Rousseaux

The oceans play a critical role in the global carbon cycle. More than 90% of the active non-geological carbon pool resides in the oceans. Estimates of global primary production suggest that the oceans contribute about half. One quarter of the carbon emitted by anthropogenic sources is thought to be sequestered in the oceans (Gregg et al., 2012 and references therein).

MERRA products were used to force the NASA ocean biogeochemical model to estimate surface carbon inventories and fluxes in the global oceans. The results were compared to in-situ carbon data and estimates. The model exhibited skill for ocean dissolved inorganic carbon (DIC), partial pressure of ocean CO_2 (pCO_2) and air-sea fluxes (FCO_2). The MERRA-forced model produced global mean differences of 0.02% (~ 0.3 µM) for DIC, -0.3% (about -1.2 µatm; with the model lower) for pCO_2, and -2.3% (-0.003 mol C m^{-2} y^{-1}) for FCO_2 compared to in-situ estimates. Basin-scale distributions were significantly correlated with observations for all three variables (r=0.97, 0.76, and 0.73, P<0.05, respectively for DIC, pCO_2, and FCO_2). The sign of the fluxes over all major oceanographic basins was in agreement with in-situ estimates. However, there were substantial basin-scale and local departures.

The model was forced with three other reanalysis products, NCEP2, NCEP1 and ECMWF. Model representations of global air-sea carbon fluxes were insensitive to the choice of forcing reanalysis. All global FCO_2 results were within 20% of in-situ estimates (MERRA and NCEP1 were within 7%) and all exhibited statistically significant positive correlations across ocean basins. There were, however, substantial departures among basin estimates from the different forcings. The high latitudes and tropics had the largest ranges in estimated fluxes among the reanalyses. No individual reanalysis produced uniformly better or worse results in the major oceanographic basins.

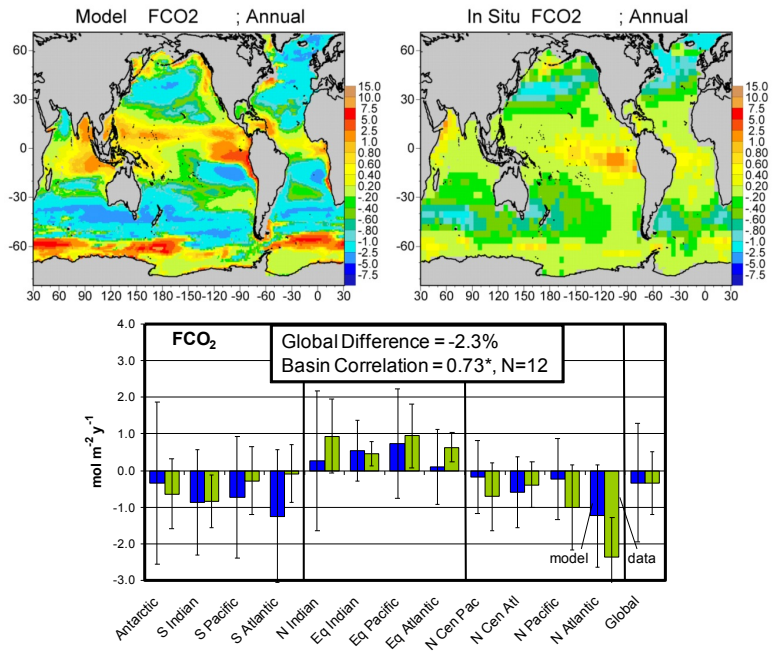

Figure 1: Annual CO_2 flux (FCO_2, mol C m^{-2} y^{-1}) distributions and statistics from the model (blue) and data (green). The model-data basin correlation is statistically significant at P < 0.05. Southern, tropical, and northern basins are delineated on the bar graph. A positive flux indicates a source to the atmosphere. Error bars indicate the standard deviation.

Publication:

Gregg, W.W., N.W. Casey, and C.S. Rousseaux, 2012: Global surface ocean carbon estimates in a model forced by MERRA. *J. Climate*, Special Collection on MERRA (submitted).

Evaluation of GEOS-5/GOCART Simulations of SO_2 and Aerosol Extinction Profile during the Frostburg and DISCOVER-AQ Field Campaigns

Virginie Buchard-Marchant and Arlindo da Silva

The Frostburg and DISCOVER-AQ regional air quality campaigns that took place over the Maryland region on November 2010 and summer 2011 provided an opportunity to evaluate the GEOS-5/GOCART model simulations of SO_2 and aerosol extinction profile against in-situ and satellite measurements and thereby guide model improvements.

One of the objectives of the University of Maryland's Frostburg field campaign in November 2010 was to monitor sulfur dioxide (SO_2), a major atmospheric pollutant with a strong anthropogenic component, mostly produced by the combustion of fossil fuel and other industrial activities. As a precursor of sulfate aerosols that affect climate, air quality, and human health, this gas needs to be monitored on a global scale.

By comparing the modeled SO_2 against observed data, such as aircraft and ground-based measurements from the Environmental Protection Agency (EPA) network, we have first evaluated the GEOS-5 vertical distribution of SO_2 (Figure 1). One can see that GEOS-5 captures most of the major features of the aircraft observations. GEOS-5 overestimated the observed SO_2 surface concentrations; the main reason for these discrepancies was found to be the emission injection height considered in the model (Figure 2).

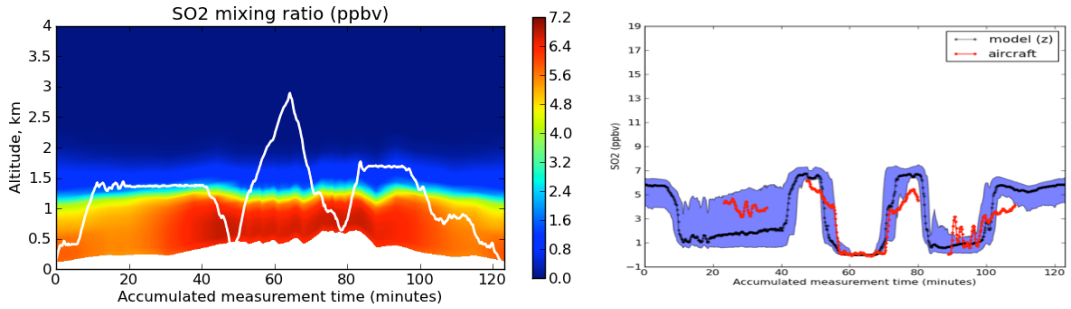

Figure 1: GEOS-5/GOCART SO_2 simulations (revised run) along the flight track on 11/08/2010. On the left, which shows the modeled SO_2 vertical profiles, the white line is the aircraft altitude; on the right, the red line is the observed SO_2 concentration, the black line is the modeled SO_2 concentration, and the blue shading shows the range of simulated SO_2 for surrounding grid-boxes.

We used a new dataset (EDGAR v4.1), available at 0.5° horizontal resolution, that allowed us to emit the "non-energy" emissions (from transportation, manufacturing industries, residential) into the lowest GEOS-5 layer and the "energy" emissions from power plants at higher levels between 100 and 500 meters (referred to as "Revised Run").

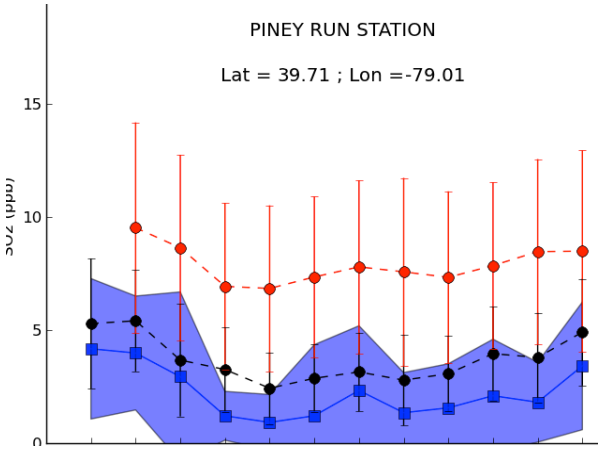

Figure 2: Monthly averaged concentrations of SO_2 at the surface in 2010 at the Piney Run station in Maryland. Blue squares are observations, red circles are model simulations with the control run, black circles are revised model simulations. Vertical bars are the standard deviations of monthly values for the model, shaded blue area for observations.

Next, we have evaluated the GEOS-5 vertical structure of aerosol extinction using data collected during the DISCOVER-AQ campaign. The overarching goal of DISCOVER-AQ is to better understand the processes that relate column-averaged measurements of atmospheric constituents by satellites to near-surface air-quality parameters.

During this study, the initial diagnostic of the NRT GEOS-5 indicated an overly deep planetary boundary layer (PBL) height that could be traced back to a precipitation deficit in the preceding season that led to a hot and dry land surface. Correcting the soil moisture and prescribing observed precipitation improved the Bowen ratio and led to better near-surface temperatures, PBL height and aerosol vertical distributions.

By comparing the GEOS-5/GOCART extinction profiles against the airborne High Spectral Resolution Lidar (HSRL) aerosol measurements, we could see that GEOS-5 was able to capture the day-to-day variability in aerosol extinction. A comparison for a flight on 7/11/2012 is shown in Figure 3. During this day we noticed that GEOS-5 was able to capture the aerosol layer above the PBL, but the GEOS-5 extinction tended to peak at the top of the PBL, while HSRL indicated a more uniform mixing within the PBL.

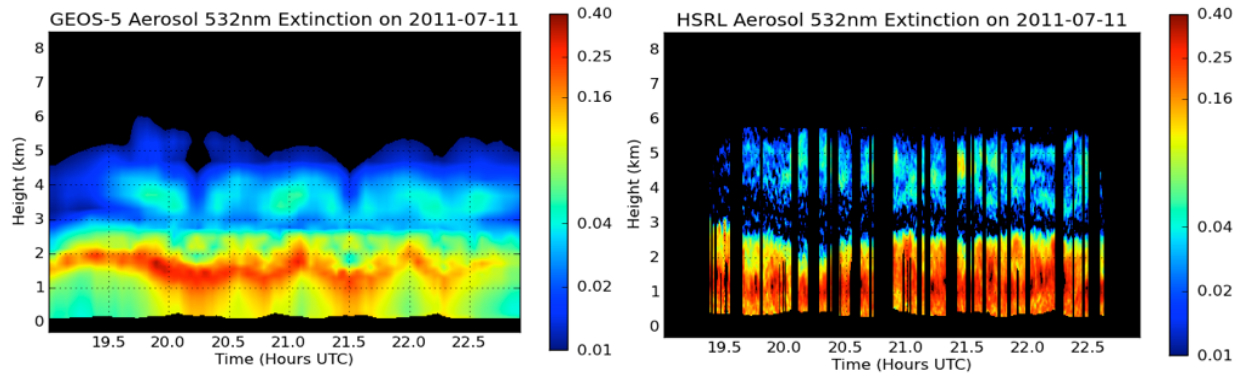

Figure 3: On the left, GEOS-5/GOCART Aerosol Extinction profiles at 532 nm interpolated to the HSRL in time and space from the GEOS-5 3-hourly extinction profile product. On the right, HSRL Aerosol Extinction profiles at 532 nm.

The GEOS-5 derived Aerosol Optical Depth (AOD) and PM 2.5 surface concentrations have also been evaluated against AERONET "DRAGON" and MDE stations showing that GEOS-5 was able to reproduce the day-to-day variability of both products. During this analysis, we have also noticed that GEOS-5 tended to underestimate the observed AOD and the PM 2.5. This can be explained in part by the remaining overestimation of PBL heights. Although MODIS AOD is being assimilated, the twice daily data availability is not sufficient to constrain the model throughout the rest the day.

Publication:

Buchard-Marchant, V., A. da Silva, P. Colarco, and co-authors, 2012: Evaluation of Sulfur Dioxide (SO_2) Simulations with the GEOS-5/ GOCART Model (over North America) during the Frostburg Field Campaign (*draft ms*).

Climate Variability and Phytoplankton Composition in the Pacific Ocean

Cecile Rousseaux and Watson Gregg

The El Niño – Southern Oscillation (ENSO) is the dominant source of interannual climate variability in the tropical Pacific Ocean. During El Niño events, the phytoplankton concentration, represented by chlorophyll, decreases in the Equatorial Pacific (e.g. Strutton and Chavez, 2000) and the associated Peruvian anchovy fishery collapses (Chavez et al., 2003). The generalized mechanisms for these events are well described: wind anomalies lead to reduced upwelling in the eastern tropical Pacific, impacting total phytoplankton concentration and the fisheries that depend upon them. However, the effect climate variability has on phytoplankton community structure, and the spatial and temporal extent of the effects, are less well known. Based on historical data sets, there are some indications that the phytoplankton community structure might shift (e.g. Karl et al., 2001). The effects on a global scale are only now beginning to be explored (e.g. Uitz et al., 2010).

The effect of climate variability on phytoplankton community structure was assessed for the tropical and sub-tropical Pacific Ocean between 1998 and 2007 using the NASA ocean biogeochemical model (NOBM) and its assimilation system. The tropical and sub-tropical phytoplankton communities exhibited a wide range of responses to climate variability, from radical shifts in the Equatorial Pacific, to changes of only a couple of phytoplankton groups in the North Central Pacific, to no significant changes in the South Pacific. In the Equatorial Pacific, climate variability represented by ENSO dominated the variability of phytoplankton. Here, nitrate, chlorophyll and all but one of the four phytoplankton types (diatoms, cyanobacteria and coccolithophores) were strongly correlated ($p<0.01$) with the Multivariate El Niño Southern Oscillation Index (MEI) (Figure 1). During La Niña events, diatoms increased and expanded westward along the cold tongue (correlation with MEI, $r= -0.81$), while cyanobacteria concentrations decreased significantly ($r= 0.61$) (Figure 2). El Niño produced the reverse pattern, with cyanobacteria populations increasing while diatoms plummeted. This represented a radical shift in the phytoplankton community in response to climate variability. In the North Central Pacific, the MEI was only significantly correlated ($r= -0.31$) with chlorophytes. Ocean biology in the South Pacific was not significantly correlated with MEI.

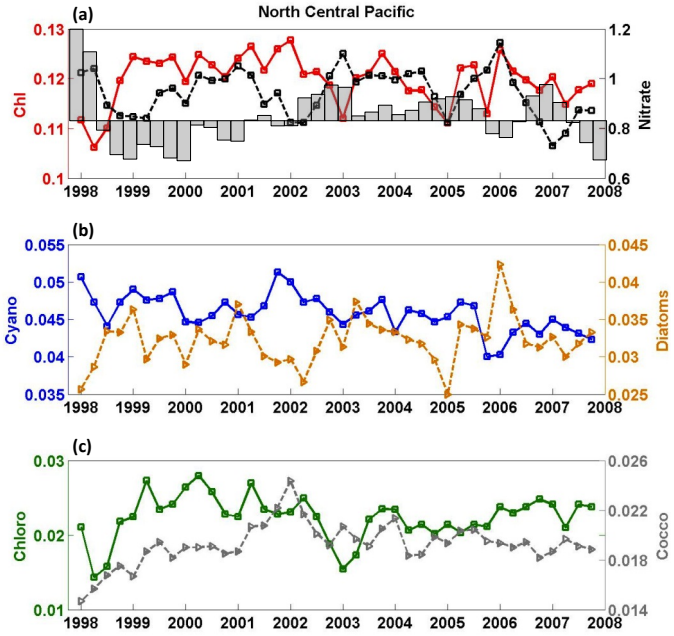

Figure 1: Temporal variation of nitrate and phytoplankton concentration in the Equatorial Pacific. Seasonal average (JFM, detrended, seasonal climatology removed and average added) of (a) chlorophyll-a (mg chl-a m^{-3}) and nitrate concentration (µM). Shaded bars represent the MEI. (b) Abundance of cyanobacteria and diatoms from NOBM (mg chl a m^{-3}). (c) Abundance of chlorophytes and coccolithophores from NOBM (mg chl a m^{-3}).

The phytoplankton composition from the assimilation model was compared to the one from a new empirical algorithm using satellite data (Hirata et al., 2011). Despite differences in the absolute concentration, the relative abundance from the model and the satellite-derived approach showed a similar shift in phytoplankton community in the Equatorial Pacific. The diverse response of phytoplankton in the different basins of the Pacific suggests the different roles climate variability can play in ocean biology.

These results provide the first evidence of how climate variability affects the phytoplankton community structure on a basin scale in the tropical and sub-tropical Pacific Ocean. The results here on the ocean biology response to interannual climate variability may have implications for climate change (long-term trends), considering recent results that the intensity and frequency of ENSO events may have increased in past warm periods (Scroxton et al., 2011). This suggests that the overall increase in cyanobacteria concentration and the decrease in the area where diatoms predominate during El Niño events may contribute to the decrease in fish stock and the collapse of fisheries such as the anchovies fisheries that was observed during the 1997-98 El Niño event. Our results suggest that this change in the predominant carbon pathway during El Niño events does not occur over the entire Pacific Ocean but rather mostly in the Equatorial Pacific, locally in the North Central Pacific, and has negligible effect on the phytoplankton composition in the South Pacific. We have expended much effort in validation of the large-scale distributions of the phytoplankton groups, and have additionally assimilated the total chlorophyll data to improve the realism. The results are ultimately dependent upon the physical and physiological characterization of the phytoplankton embedded in the model. While direct observations of phytoplankton composition during ENSO are rare, it is encouraging that those that do exist generally support our results.

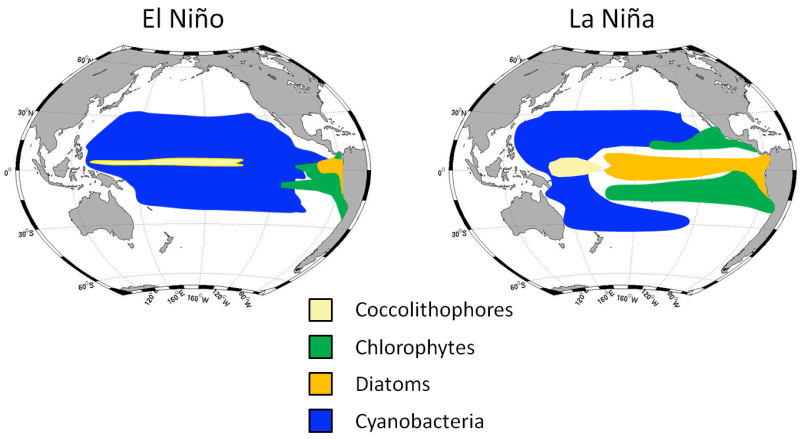

Figure 2: Conceptual description of the effect climate variability has on the distribution of phytoplankton community structure in the Pacific Ocean. An average for JFM 1998 was used as representative of El Niño conditions and an average for JFM 2000 was used as for La Niña. The spatial patterns loosely approximate predominance, except for coccolithophores where presence is depicted because they are rarely predominant.

References:

Chavez, F.P., J. Ryan, S.E. Lluch-Cota, and C. Ñiquen, 2003: *Science*, **299**, 217-221.

Hirata, T., and co-authors, 2011: *Biogeosciences*, **8**, 311-327.

Karl, D.M., R.R. Bidigare, and R.M. Letelier, 2001: *Deep Sea Res. Part II*, **48**, 1449-1470.

Rousseaux, C.S., and W.W. Gregg, 2012: Climate variability and phytoplankton composition in the Pacific Ocean. *J. Geophys. Res*. (submitted).

Scroxton, N., and co-authors, 2011: *Paleoceanography*, **26**, PA2215, doi:2210.1029/2010PA002097

Strutton, P.G., and F.P. Chavez, 2000: *J. Geophys. Res*., **105**, 20,089-26,101.

Uitz, J., H. Claustre, B. Gentili, and D. Stramski, 2010: *Global Biogeochemical Cycles*, **24**, GB3016.

Climate Variability and Weather Extremes

Siegfried Schubert and Young-Kwon Lim

The climate community is being challenged to provide increasingly more comprehensive societally-relevant information about the impacts of climate change that go well beyond broad statements about how much the global mean temperature will change. This in turn requires more comprehensive assessments of the quality of climate models to reproduce past regional climate impacts as well as the full spectrum of observed climate variability, including those aspects (such as weather extremes) that are likely to have the greatest impact on society.

We examine here the simulated and observed short-term climate variability and weather extremes that have occurred over the last three decades with a focus on the winter hemispheres. Three AMIP-style simulations were conducted with the GEOS-5 AGCM at moderately high horizontal resolution (50 km) forced with observed SST, ozone, and GHGs, with for the period 1980-2009. Other experiments include a 20-year run with repeating climatological SSTs, a run with a spatially uniform 2°C added to the climatological SST, and another with climatological SST and doubled CO_2. The model results are compared with MERRA and other observations.

The model reproduces the leading modes of monthly Northern Hemisphere (NH) and Southern Hemisphere (SH) winter (January-March, JFM, and July-September, JAS) variability including the Pacific North American (PNA) pattern, North Atlantic Oscillation (NAO), Northern Annular Mode (NAM), Southern Annular Mode (SAM), and the Pacific South American (PSA) patterns (e.g., Figure 1). With the exception of the PNA pattern (which shows a tendency toward negative values), there is little evidence of any trends in these internal modes over the last three decades. Separate trend patterns are obtained in both seasons, but they are characterized by nearly globally uniform height increases that, during JFM, are intertwined with the ENSO response. The model reproduces the winter storm tracks in both hemispheres (e.g., Figure 2), as well as extreme value statistics over land, including 10-year return values of daily maximum precipitation, warmest day, and warmest night, with however a notable cold bias in the NH high latitudes during JFM, and a tendency for too large precipitation extremes in low latitudes. In addition, the model reproduces the predominant seasonal mean regional impacts that the above modes of variability have on surface temperature, precipitation and storm tracks.

The primary changes in the SST over the last three decades consist of a warming in the Atlantic, Indian, and western Pacific oceans, together with cooling in the eastern tropical Pacific. The associated decadal changes in the atmosphere estimated from MERRA (and reproduced by the model) consist of a general tropospheric and continental surface warming during both seasons, and a La Niña-type (negative PNA) wave response during JFM. Other decadal-scale changes include a poleward shift of the storm tracks (modified by the La Niña response over the North Pacific/North American region) during JFM, and a weakened and expanded Hadley Cell during both seasons – with the latter based on the model results alone due to limitations of the reanalysis data in estimating trends in the divergent circulation. The 2°C SST warming run exhibits several aspects of the observed changes including a weakened and expanded Hadley Cell, and a poleward shift in the subtropical jets and storm tracks. The direct radiative impact of doubling CO_2 on the atmosphere and land is generally weak, but includes interior NH continental warming of up to 1°C and cooling in the stratosphere. The spatial structure of the leading internal modes of variability appear to be robust with respect to both the SST and CO_2 increases, with some evidence of enhanced variability of the NAM in the 2° SST warming run.

The observed and simulated changes in boreal winter extremes between the two periods reflect the continental warming and, over North America, the La Niña-like response, including the northward shift of the storm tracks and the generally warmer conditions over the southern U.S. Most of the southern U.S. shows a decrease in the number of days with heavy precipitation, while much of Europe and eastern Russia show an increase. Much of southern and central Asia, and the Mediterranean region are characterized by an increase in the number of warm days. The major discrepancy between the simulations

and observations is that the latter show a reduction in the number of warm days (and an increase in the number of cold days) in northern Russia while the simulations produce the opposite, although observations are missing in the most recent decade making the observational results of questionable reliability in that region.

The simulated austral winter temperature extremes show an increase in the number of warm days and a decrease in the number of cold days over much of the SH land masses with the largest changes occurring over northern South America, southern Africa and northern Australia. The simulated changes in the number of days with heavy precipitation show a more complicated pattern with, for example, a reduction over the Amazon basin, and an increase over equatorial Africa. The reliability of the simulated changes in the SH extremes is however difficult to assess, since observational estimates in most regions are not available or of questionable quality.

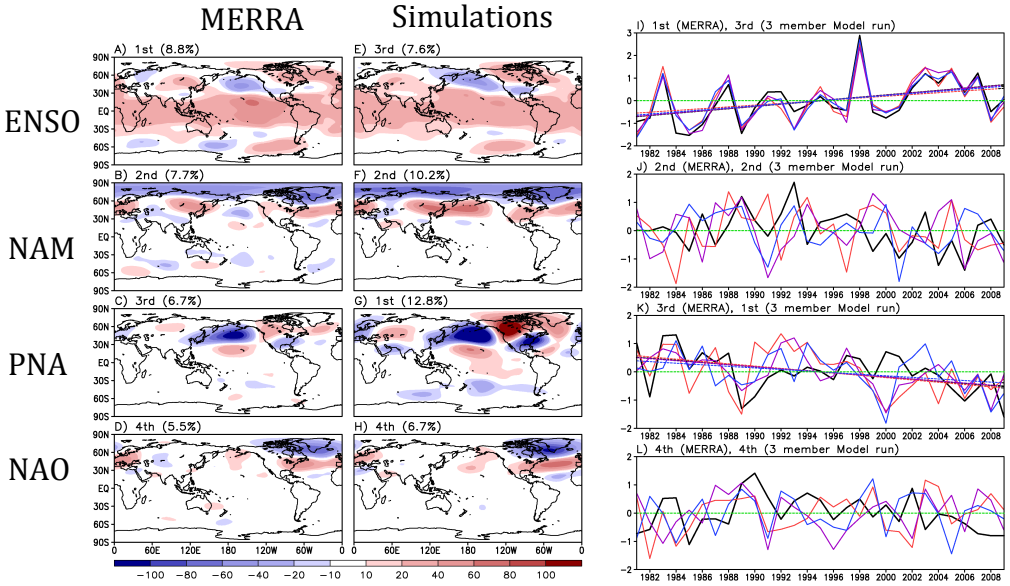

Figure 1: Left set of panels: The four leading rotated empirical orthogonal functions (REOFs) of the monthly 250 hPa height field for JFM, 1981-2009. Left panels (A-D) are from MERRA and the right panels (E-H) are from GEOS-5 (note the reordering of the GEOS-5 REOFs to match MERRA). Right set of panels (I-L): The time series of the four leading PCs. The black line is from MERRA and the colored lines are the three model ensemble members. The monthly values are averaged to produce seasonal (JFM) means before plotting. For the first and third mode the trend lines for each ensemble member and MERRA are significant at the 10% level. The PCs are normalized to have unit variance, so amplitude information is contained in the spatial maps of the REOFs.

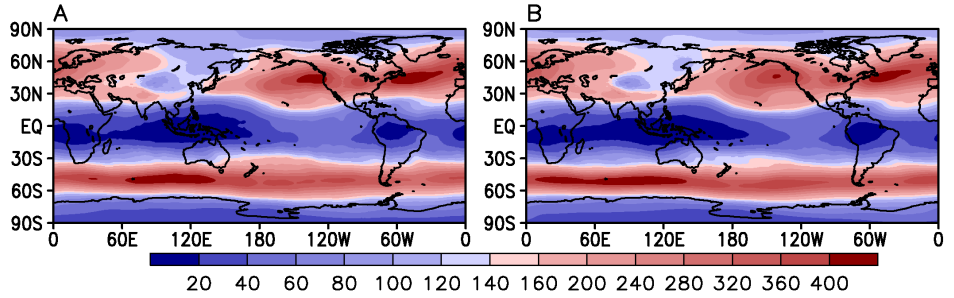

Figure 2: Variance of daily v-wind for JFM (1981-2009) at 250 hPa (top) from MERRA (A) and the model simulations (B). The variance is based on daily data. Units are $(m/s)^2$.

Publication:

Schubert, S.D., and Y.-K. Lim, 2012: Climate Variability and Weather Extremes: Model-Simulated and Historical Data. In ***Hydrologic Extremes in a Changing Climate - Detection, Analysis & Uncertainty.*** S. Sorooshian, D. Easterling, A. AghaKouchak, S. Schubert, and K. Hsu, Editors.

GEOS-5 Production Operations

Gi-Kong Kim, Robert Lucchesi, and Jonathan Kelly

Our GEOS-5 data production achieved a significant milestone this year when we successfully upgraded the NRT operational system to generate GEOS-5 assimilation products and forecasts at ¼° spatial resolution. Likewise, the GMAO continued to generate and deliver MERRA products with approximately 3 weeks delay of real-time. The use of MERRA data by researchers and scientists across the globe continued to trend upward. In fact, the total accumulated MERRA data volume downloaded by users surpassed 1.2 PB in June 2012.

More details about our products are provided at http://gmao.gsfc.nasa.gov/products/.

Near Real Time (NRT) Products Upgraded

The GMAO continued providing NRT GEOS-5.2.0 products using 128 processors on the IBM Linux cluster at the NASA Center for Climate Simulation (NCCS). However, in August 2011 we began generating GEOS-5.7.2 products at ¼° horizontal resolution using 720 processors.

The GEOS-5.7.2 system not only includes many advances in the Global Circulation Model (GCM), physics, and the GSI analysis but also has the capability to assimilate new data types such as AMSRE, MTIASI, MHS, and HIRS4. Other notable additions are ocean-related surface quantities and aerosol diagnostic products. Our new output products provide much more realistic representation of the atmospheric fields at finer scale. With this change, the temporal frequencies of our output have doubled or in some cases tripled. Also, compared to the GEOS-5.2.x, the number of product collections increased from 10 to 25 and total daily data volume sent to the GES DISC (http://disc.sci.gsfc.nasa.gov/) for distribution to users increased from 10 GB to 62 GB.

The operational interface between GEOS-5 production system and the Land Atmosphere Near real-time Capability for EOS (LANCE) increased. The real time AIRS data the GEOS-5 system previously acquired from NOAA/NCEP is now obtained from LANCE. LANCE, in return, will be receiving GEOS-5 real time data for MODIS/MODAPS data processing.

The primary operational users list includes the EOS instrument teams (i.e., MLS, TES, and MODIS), other NASA and international projects (i.e., CALIPSO, SRB, FlashFLUX, POWER, GLDAS, Flood Warning, and JAXA/SMILES), and research teams at universities and government organizations. We are pleased to note that there were two additions this year: the Community Earth System Model (CESM) team at NCAR and the MODIS L-3 AOD production team.

A New Strategy for GEOS-5 Forward Processing

The state-of-the-art GEOS system evolves at the pace of scientific and technological advancements in Earth System Modeling, data assimilation, and high performance computing. The GMAO needs to keep pace with the changes and be capable of running the "best" GEOS system possible in real time. Products from the 'best' system are critical to system evaluation, interactions with other data assimilation centers, and real time support for the field campaigns. The ¼° resolution that the current real time system is running is the highest spatial resolution feasible at this time to support instrument teams for their real time needs. However, one drawback of the data production at this resolution is that its throughput is only a little over three data days per processing day. This rate is often inadequate to meet the *reprocessing* requirements for the instrument teams.

We are now undertaking a new strategy for GEOS-5 forward processing that would accommodate both the GMAO's need to run state-of-the-art models and EOS Instrument Teams for tailored reprocessing. Our proposed strategy is to run two NRT forward processing systems, one (FP) generating ¼° data including forecasts as well as assimilation products from the 'best' system and the other (FP-IT) providing ½° analysis from a semi-frozen system. FP will be primarily used for system evaluation, GMAO interactions with other data assimilation centers and field campaigns. FP-IT will provide real

time data as well as reprocessing data when needed. It will serve the EOS Instrument Teams who require stable products over a long time period.

30+Year Reanalysis (MERRA) Surpassed 1 Petabyte of User Downloads

MERRA data have been available for public access since December 2008 via an online data distribution system called MDISC (http://disc.sci.gsfc.nasa.gov/mdisc/) at the GES DISC. MERRA has attracted a global user community and access by users has steadily increased over the years (Figure 1). We reached a milestone in March 2012, when the cumulative total data downloaded surpassed 1 PB.

The list of MERRA product collections also continues to expand with the addition of an ocean collection of MERRA fields targeted for forcing ocean models. This ocean collection, covering the entire MERRA period, has been shipped to MDISC; near real time data delivery continues. Another dataset added is the MERRA-Land collection. As with the ocean collection, MERRA-Land products have been delivered to MDISC and NRT production is continued.

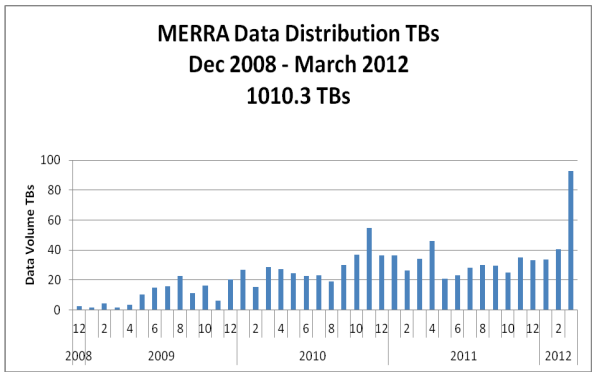

Figure 1: Monthly MERRA data distribution in data volumes accessed by users

G5.4.1-CERES products

The GEOS-5 data production for CERES has progressed without any problems. GEOS-5.4.1 data production for the CERES team started in December 2010 and continues to the present time. The production started in two separate streams. The production stream for the time period of 1997 through 2000 was completed in June 2011. The stream beginning from February 2000 is currently generating 2008 data. Data production for CERES will continue until the February 2000 stream catches up to real time, which is expected to occur in the fall of 2012.

Mission Support

The GMAO provided real time support to several field campaigns in 2011. These included: Deriving Information on Surface Conditions from Column and Vertically Resolved Observations Relevant to Air Quality (DISCOVER-AQ), BOReal forest fires on Tropospheric oxidants over the Atlantic using Aircraft and Satellite (BORTAS) in July, HIAPER Pole-to-Pole Observations (HIPPO) of Carbon Cycle and Greenhouse Gases Study from June - August, and Hurricane and Severe Storm Sentinel (HS3) in August. Support included providing 5-day forecasts primarily for flight planning and for onsite analyses of the observations. Frequently our GEOS-5 forecast products are carefully tailored to meet the needs of specific campaigns.

GMAO plans to provide real time support to HS3 again in September 2012.

Publications

Allen, D.A., A.R. Douglass, G.L. Manney, S.E. Strahan, J. Krosschell, J.V. Trueblood, **J.E. Nielsen**, **S. Pawson**, and **Z. Zhu,** 2011: Modeling the frozen-in anticyclone in the 2005 summer stratosphere. *Atmos. Chem. Phys.*, **11**, 4557-4576. DOI: 10.5194/acp-11-4557-2011.

Barahona, D.O., 2011: On the ice nucleation spectrum. *Atmos. Chem. Phys.*, **11**, 29601-29646. DOI: 10.5194/acpd-11-29601-2011.

Bosilovich, M.G., F. Robertson, and **J. Chen**, 2011: Global energy and water budgets in MERRA. *J. Climate*, **24**, 5721-5739. DOI: 10.1175/2011JCLI4175.1.

Brunke, Michael A., Z. Wang, X. Zeng, **M. Bosilovich**, and C-L. Shie, 2011: An assessment of the uncertainties in ocean surface turbulent fluxes in 11 reanalysis, satellite-derived, and combined global datasets. *J. Climate*, **24**, 5469-5493. DOI: 10.1175/2011JCLI4223.1

Butchart, N., **S. Pawson** and co-authors, 2011: Multi-model climate and variability of the stratosphere. *J. Geophys. Res.*, **116**, D05102. DOI: 10.1029/2010JD014995.

Chao, W., 2012: Correction of excessive precipitation over steep and high mountains in a GCM. *J. Atmos. Sci.*, **69**, 1547-1561. DOI: 10.1175/JAS-D-11-0216.1.

Chang, Y., S.D. Schubert, and **M. Suarez**, 2011: Attribution of the extreme U.S. East Coast snowstorm activity of 2010. *J. Climate*, **25**, 3771–3791. DOI: 10.1175/JCLI-D-11-00353.1.

Cullather, **R.I**., and **M. Bosilovich**, 2012: The energy budget of the polar atmosphere in MERRA. *J. Climate*, **25**, 5-24. DOI: 10.1175/2011JCLI4138.1.

Cullather, R.I., and **M. Bosilovich**, 2011: The moisture budget of the polar atmosphere in MERRA. *J. Climate*, **24**, 2861-2879. DOI: 10.1175/2010JCLI4090.1.

Decker, M., M.A. Brunke, Z. Wang, K. Sakaguchi, X. Zeng, and **M. Bosilovich**, 2012: Evaluation of the reanalysis products from GSFC, NCEP, and ECMWF using flux tower observations. *J. Climate*, **25**,1916-1944. DOI: 10.1175/JCLI-D-11-00004.1.

De Lannoy, G.J.M., R.H. Reichle, and V.R.N. Pauwels, 2012: Global Calibration of the GEOS-5 L-band Microwave Radiative Transfer Model over Land Using SMOS Observations. *J. Hydrometeor. (Submitted)*

De Lannoy, **G.J.M., R.H. Reichle**, K.R. Arsenault, P.R. Houser, S.V. Kumar, N.E.C. Verhoest, and V.R.N. Pauwels, 2012: Multi-scale assimilation of AMSR-E snow water equivalent and MODIS snow cover fraction in Northern Colorado. *Water Resour. Res.*, **48**, W01522. DOI: 10.1029/2011WR010588.

Draper, **C.S**., **R.H. Reichle**, **G.J.M. De Lannoy**, and **Q. Liu**, 2012: Assimilation of passive and active microwave soil moisture retrievals. *Geophys. Res. Lett.*, **39**, L04401. DOI: 10.1029/2011GL050655.

El Akkraoui, A., Y. Tremolet, and **R. Todling,** 2011: Preconditioning of variational data assimilation and the use of a bi-conjugate gradient method. *Q. J. Royal Meteorol. Soc., (In Press).*

Errico, R.M., R. Yang**, N. Prive, K-S. Tai, R. Todling, M. Sienkiewicz,** and **J. Guo,** 2012: Development and validation of observing system simulation experiments at the Global Modeling and Assimilation Office. *Q. J. Meteorol. Soc. (In Press)*

Forman, B.A., and **R.H. Reichle**, and C. Derksen, 2012: Estimating passive microwave brightness temperature over snow-covered land in North America using a land surface model and an artificial neural network. *IEEE Trans. Geo. Rem. Sens*. *(Submitted)*

Forman, B.A., **R.H. Reichle**, and M. Rodell, 2012: Assimilation of terrestrial water storage from GRACE in a snow-dominated basin. *Water Resour. Res.*, **48**, W01507. DOI:

10.1029/2011WR011239.

Forman, B.A., and S.A. Margulis, 2012: Impact of covariance localization on ensemble estimation of surface downwelling longwave and shortwave radiation. *J. Hydrometeor.,* DOI: 10.1175/JHM-D-11-073.1. *(In Press)*

Guo, Z., P. Dirmeyer, T. DelSole, and **R. Koster**, 2012: Rebound in atmospheric predictability and the role of the land surface. *J. Climate,* DOI: 10.1175/JCLI-D-11-00651.1. *(In Press)*

Ham, Y.-G., I.S. Kang, D. Kim, and J.S. Kug, 2011: El-Niño southern oscillation simulated and predicted in SNU coupled GCMs. *J. Climate*, DOI: 10.1007/s00382-011-1171-5. *(In Press)*

Ham, Y-G., I-S. Kang, and J-S Kug, 2012: Coupled bred vectors in the tropical Pacific and the application to ENSO prediction. *Prog. Oceanography,* DOI**:** 10.1016/j.pocean.2012.04.005. *(In Press)*

Ham, Y.-G., H.-J. Song, and **R. Todling**, 2012: The Non-stationary Incremental Analysis Updates (NIAU) algorithm. *Mon. Wea. Rev. (Submitted).*

Ham, Y.-G., and J.-S. Kug, 2011: How well do current climate models simulate two types of El Niño? *Clim. Dyn.*, DOI: 10.1007/s00382-011-1157-3. *(In Press)*

Ham, Y.-G., and **M. Rienecker**, 2012: Flow-dependent empirical singular vector with an ensemble Kalman filter data assimilation for El Nino prediction. *Clim. Dyn.*, DOI: 10.1007/s00382-012-1302-7. *(In Press)*

Hardiman, S., and co-authors, 2011: Improved predictability of the NAO using stratospheric final warmings. *J. Geophys. Res.*, **116**, D18113. DOI: 10.1029/2011JD015914.

Holmes, T.R.H., T. Jackson**, R. Reichle**, and J. Basara, 2012: An assessment of surface soil temperature products from numerical weather prediction models using ground-based measurements. *Water Resour. Res.*, **48**, WO2531. DOI: 10.1029/2011WR010538.

Houborg, R., M. Rodell, B. Li, **R.H. Reichle**, and B.F. Zaitchik, 2012: Drought indicators based on model assimilated GRACE terrestrial water storage observations. *Water Resour. Res*., DOI: 10.1029/2011WR011291. *(In Press)*

Jimenez, C., **R.H. Reichle**, and co-authors, 2011: Global inter-comparison of 12 land surface heat flux estimates. *J. Geophys. Res.*, **116**, D02102. DOI: 10.1029/2010JD014545.

Koster, R., and **S.P. Mahanama**, 2012: Land-surface controls on hydroclimatic means and variability. *J. Hydrometeor. (Submitted)*

Kumar, S.V., **R.H. Reichle**, K.W. Harrison, C.D. Peters-Lidard, S. Yatheendradas, and J.A. Santanello, 2012: Model parameter estimation for a priori bias correction in land data assimilation: A soil moisture case study. *Water Resour. Res. (In Press)*

Kug, J.-S., and **Y.-G. Ham**, E.J. Lee, and I.-S. Kang, 2011: Empirical Singular Vector (ESV) method for ensemble ENSO prediction with a coupled GCM. *J. Geophys. Res.*, **116**, C08029. DOI: 10.1029/2010JC006851.

Kug, J.-S., and **Y.-G. Ham**, 2011: Are there two types of El Nina? *Geophys. Res. Lett.,* **38**, L16704. DOI: 10.1029/2011GL048237.

Langlois, T.J., B.T. Radford, K.P. Van Niel, J.J. Meeuwig, A.F. Pearce, **C. S. G. Rousseaux**, G. A. Kendrick, and E.S. Harvey, 2012: Consistent abundance distributions of marine fishes in an old, climatically buffered, infertile seascape. *Global Ecol. Biogeogr.,* DOI: 10.1111/j.1466-8238.2011.00734.x. *(In Press)*

Lee, M.-I., **S.D. Schubert**, and D. Kim, 2011: Representation of tropical storms in the Northwestern Pacific by the modern-era retrospective analysis for research and applications. *Asia-Pacific J. Atmos.*

Sci., **47**, 245-253. DOI: 10.1007/s13143-011-0013-z.

Liang, Q., **A. da Silva, J.E. Nielsen**, **S. Pawson**, and co-authors, 2011: Reactive nitrogen, ozone and ozone Production in the Arctic troposphere and the impact of stratosphere-troposphere exchange. *Atmos. Chem. Phys.*, **11**, 13181-13199. DOI: 10.5194/acp-11-13181-2011.

Lim, Y.-K., and **S. Schubert**, 2011: The impact of ENSO and the Arctic oscillation on winter temperature extremes in the Southeast United States. *Geophys. Res. Lett.,* **38,** L15706. DOI: 10.1029/2011GL048283.

Liu, Q., **R. Reichle**, R. Bindlish, M. Cosh, W. Crow, R. de Jeu, **G. De Lannoy**, G. Huffman, and T. Jackson, 2011: The contributions of precipitation and soil moisture observations to the skill of soil moisture estimates in a land data assimilation system. *J. Hydrometeor.*, **12**, 750-765. DOI: 10.1175/JHM-D-10-05000.1.

Lu, J., and **B. Zhao**, 2012: The role of oceanic feedback in the climate response to doubling CO2. *J. Climate. (Submitted)*

Mahanama, S.P.P., B. Livneh, **R.D. Koster**, D. Lettenmaier, and **R.H. Reichle**, 2012: Soil moisture, snow, and seasonal streamflow forecasts in the United States. *J. Hydrometeor.*, **13**, 189-203. DOI: 10.1175/JHM-D-11-046.1.

Maggioni, V., **R.H. Reichle**, and E.N. Anagnostou, 2011: The effect of satellite-rainfall error modeling on soil moisture prediction uncertainty. *J. Hydrometeor.*, **12**, 413-428. DOI: 10.1175/2011JHM1355.1.

Maggioni, V., **R.H. Reichle**, and E.N. Anagnostou, 2012: The impact of rainfall error characterization on the estimation of soil moisture fields in a land data assimilation system. *J. Hydrometeor*. DOI: 10.1175/JHM-D-11-0115.1. *(In Press)*

Maggioni, V., E.N. Anagnostou, and **R.H. Reichle**, 2012: The impact of land model structural, parameter, and forcing errors on the characterization of soil moisture uncertainty. *Hydrol. Earth Syst. Sci*., **9**, 2283-2319. DOI: 10.5194/hessd-9-2283-2012. *(Submitted)*

McCarty, W., R.M. Errico, and **R. Gelaro**, 2011: Cloud coverage in the joint OSSE nature run. *Mon. Wea. Rev.*, **140**, 1863-1871. DOI: 10.1175/MWR-D-11-00131.1.

Molod, A., 2012: Constraints on the total water PDF in GCMs from AIRS and a high resolution model. *J. Climate. (In Press)*

Mueller, B., **R.H. Reichle**, and co-authors, 2011: Evaluation of global observations-based evapotranspiration datasets and IPCC AR4 simulations. *Geophys. Res. Lett.*, **38**, L06402. DOI: 10.1029/2010GL046230.

Nearing, G.S., K.R. Thorp, W.T. Crow, M.S. Moran, **R.H. Reichle**, and H.V. Gupta, 2012: Improving DSSAT wheat yield estimates by assimilating observations of soil moisture and leaf area index. *Water Resour. Res., **DOI***: 10.1029/2011WR011420.

Norris, P.M., and A.M. da Silva, 2012: Monte Carlo Bayesian inference on a statistical model of sub-gridcolumn moisture variability using high-resolution cloud observations. Part I: Method. *Q. J. Roy. Meteorol. Soc., (Submitted).*

Orth, R., **R. Koster**, and S. Seneviratne, 2012: Inferring soil moisture memory from runoff observations. *J. Hydrometeor. (Submitted)*

Ott, L., S. Pawson, and J. Bacmeister, 2011: An analysis of the impact of convective parameter sensitivity on simulated global atmospheric CO distributions. *J. Geophys. Res.,* **116**, D21310. DOI: 10.1029/2011JD016077.

Prive, N., **R.M. Errico,** and **K.-S. Tai**, 2012: Validation of forecast skill of the Global Modeling and

Assimilation Office observing system simulation experiment. *Q. J. Roy. Meteorol. Soc. (Submitted)*

Putman, W.M., and **M. Suarez**, 2011: Cloud-system resolving simulations with the NASA Goddard Earth Observing System global atmospheric model (GEOS-5). *Geophys. Res. Lett.*, **38**, L16809. DOI: 10.1029/2011GL048438.

Reichle, R.H., **R.D. Koster**, **G.J.M. De Lannoy**, B.A. Forman, **Q. Liu, S. Mahanama**, and A. Toure, 2011: Assessment and enhancement of MERRA land surface hydrology estimates. *J. Climate*, **24**, 6322-6338. DOI: 10.1175/JCLI-D-10-05033.1.

Rienecker, M.M., and co-authors, 2011: MERRA - NASA's modern-era retrospective analysis for research and applications. *J. Climate*, **24**, 3624-3648. DOI: 10.1175/JCLI-D-11-00015.1.

Roberts, J. B., F.R. Robertson, C.A. Clayson, and **M.G. Bosilovich**, 2012: Characterization of turbulent latent and sensible heat flux exchange between the atmosphere and ocean in MERRA. *J. Climate*, **25**, 821-838. DOI: 10.1175/JCLI-D-11-00029.1.

Robertson, F.R., **M. Bosilovich, J. Chen**, and T. Miller, 2011: The effect of satellite observing system changes on MERRA water and energy fluxes. *J. Climate*, **24**, 5197-5217. DOI: 10.1175/2011JCLI4227.1.

Rousseaux, C.S., and **W.W. Gregg,** 2012: Climate variability and phytoplankton in the Pacific Ocean. *Science. (Submitted)*

Rousseaux, C.S., and **W.W. Gregg,** 2012: Climate variability and phytoplankton composition in the Pacific Ocean. *J. Geophys. Res. (Submitted)*

Sahoo, A.K., **G.J.M. De Lannoy, R.H. Reichle**, and P.R. Houser, 2011: Assimilation and downscaling of satellite observed soil moisture over the Little River experimental watershed in Georgia, USA. *Adv. Water Resour. (Submitted)*

Schubert, S., H. Wang, and **M. Suarez**, 2011: Warm season subseasonal variability and climate extremes in the Northern Hemisphere: The role of stationary rossby waves. *J. Climate*, **24**, 4773-4792. DOI: 10.1175/JCLI-D-10-05035.1.

Seneviratne, S.I., and **R.D. Koster**, 2012: A revised framework for analyzing soil moisture memory in climate data: Derivation and interpretation. *J. Hydrometeor.*, **13**, 1525-755X. DOI: 10.1175/JHM-D-11-044.1

Strode, S., **L. Ott, S. Pawson**, and T.W. Bowyer, 2012: Emission and transport of Cesium-137 from Boreal Biomass Burning the summer of 2010. *J. Geophys. Res.,* **117***,* D09302. DOI: 10.1029/2011JD017382.

Todling, R., 2012: Insights on observation impact measures. *Mon. Wea. Rev. (Submitted)*

Van Donkelaar, A., R.V. Martin, R.C. Levy, **A. da Silva**, M. Krzyzanowski, N.E. Chubarova, E. Semutnikova, and A.J. Cohen, 2011: Satellite-based estimates of ground-level fine particulate matter during extreme events: A case study of the Moscow fires in 2010. *Atmos. Env.,* **45**, 6225-6232. DOI: 10.1016/j.atmosenv.2011.07.068.

Vernieres, G., C.K.R.T. Jones, and K. Ide, 2011: Capturing eddy shedding in the Gulf of Mexico from Lagrangian observations. *Physica D,* **240**, 166-179. DOI: 10.1016/j.physd.2010.06.008.

Vinukollu, R.K., J. Sheffield, E.F. Wood, **M. Bosilovich,** and **D. Mocko**, 2012: Multimodel analysis of energy and water fluxes: Intercomparisons between operational analyses, a land surface model, and remote sensing. *J. Hydrometeor.*, **13**, 3-26. DOI: 10.1175/2011JHM1372.1.

Wang, J., **S. Pawson**, B. Tian, M.-C. Liang, R.-L. Shia, Y.-L Yung, and X. Jiang, 2011: El Niño-Southern oscillation in the tropical and Mid-Latitude column ozone. *J. Atmos. Sci.,* **68**, 1911-1921. DOI:10.1175/JAS-D-11-045.1.

Wei, J. P.A. Dirmeyer, **M. Bosilovich**, and R. Wu, 2012: Water vapor sources for Yangtze River Valley rainfall: Climatology, variability, and implications for rainfall forecasting. *J. Geophys. Res*., **117**, DO5126. DOI: 10.1029/2011JD016902.

Wernberg, T., D.A Smale, F. Tuya, M.S. Thomsen, T.J. Langlois, T. de Bettignies, S. Bennett, and **C.S. Rousseaux**, 2012: An extreme climatic event alters marine ecosystem structure in a global biodiversity hotspot. *Nature Climate Change. (Submitted)*

Wu, M.-L. C., O. Reale, **S. Schubert, M. Suarez**, and C. Thorncroft, 2011: African easterly jet: barotropic instability, waves and cyclogenesis. *J. Climate*, **25**, 1489-1510. DOI: 10.1175/2011JCLI4241.1.

Wu, M.-L., O. Reale**,** and **S. Schubert**, 2012: A characterization of African Easterly Waves on 2.5-6 day and 6-9 day time scales. *J. Climate*. *(Submitted)*

Xue, Y., M. Balmaseda, T. Boyer, N. Ferry, S. Good, I. Ishikawa, A. Kumar**, M. Rienecker**, A. Rosati, and Y. Yin, 2012: A comparative analysis of upper ocean heat content variability from an ensemble of operational ocean reanalyses. *J. Climate.* DOI: 10.1175/JCLI-D-11-00542.1. *(In Press)*

Xue, Y., M. Balmaseda, T. Boyer, N. Ferry, S. Good, I. Ishikawa, **M. Rienecker,** T. Rosati, Y. Yin, and A. Kumar, 2012: A comparative analysis of upper ocean heat content variability from ensemble operations ocean analyses. *U.S. CLIVAR Variations*, **9 (1),** 7-10.

Yasunari, T.J., **R.D. Koster**, K.-M. Lau, Aoki, T., Y.C. Sud, T. Yamazaki, H. Motoyoshi, and Y. Kodama, 2011: Influence of dust and black carbon on the snow albedo in the NASA GEOS-5 land surface model. *J. Geophys. Res.*, **116**, D02210. DOI: 10.1029/2010JD014861.

Yi, Y., J. Kimball, L. Jones, **R. Reichle**, and K. McDonald, 2011: Evaluation of MERRA land surface estimates in preparation for the soil moisture active passive mission. *J. Climate*, **24**, 3797-3816. DOI: 10.1175/2011JCLI4034.1.

TECHNICAL MEMORANDA

Molod, A., L. Takacs, M. Suarez, J. Bacmeister, I.-S. Song, and **A. Eichmann**, 2012: The GEOS-5 Atmospheric general circulation model: Mean climate and development from MERRA to Fortuna. *Technical Report Series on Global Modeling and Data Assimilation*, Vol. **28**, NASA/TM-2012-104606/28.

Rienecker, M., D. Dee, J. Woollen, G. Compo, K. Onogi, **R. Gelaro, M. Bosilovich, A. da Silva, S. Pawson, S. Schubert, M. Suarez**, D. Barker, H. Kamahori, R. Kistler, and S. Saha, 2012: Atmospheric reanalyses – Recent progress and prospects for the future. A report from a technical workshop, April 2010. *Technical Report Series on Global Modeling and Data Assimilation*, Vol. **29**, NASA/TM-2012-104606/29.

BOOK/BOOK CHAPTER

Schubert, S.D., and Y.-K. Lim, 2012: "Climate variability and weather extremes: model-simulated and historical data" in *Hydrologic Extremes in a changing climate – detection, analysis & uncertainty*. S. Sorooshian, D. Easterling, A. AghaKouchak, S. Schubert, and K. Hsu, Editors, *Springer*. *(Submitted)*

Bosilovich, M., J. Kennedy, D. Dee, A. O'Neill, 2012: On the reprocessing and reanalysis of observations for climate. *IEEE Monographs. (Submitted)*